Study of Recombination X-rays from Supernova Remnants with Suzaku

Midori Ozawa

Department of Physics, Graduate School of Science, Kyoto University
Kitashirakawa Oiwake-cho, Sakyo-ku, Kyoto, 606-8502, Japan
midori@cr.scphys.kyoto-u.ac.jp

This thesis was submitted to the Department of Physics,
Graduate School of Science, Kyoto University on January 2010
in partial fulfillment of the requirements
for the degree of Doctor of Philosophy in physics.

Abstract

A gigantic explosion of a star forms a supernova remnant (SNR). Huge kinetic energy of supernova explosion is transduced into the thermal energy of electrons and atoms by the shock wave heating, and high-temperature ($\sim 10^7$ K) plasma is formed. Because the plasma in an SNR is so thin (~ 1 cm^{-3}), it takes 10^{4-5} years to reach the ionization equilibrium state between electrons and atoms. Therefore, X-ray investigation of ionization states of the plasma in SNRs provides a good indication of the evolutionary stage of the remnants.

It is the traditional common knowledge that all the plasma in SNRs is in the ionizing state and end up in ionization equilibrium. In order to check this validity, we performed deep Suzaku observations of SNRs, W49B, IC 443, and G359.1-0.5, whose X-ray spectra are known to exhibit highly-ionized states of atoms.

The W49B spectrum exhibits an unusual structure of a saw-edged bump above 8 keV. We firmly conclude that this bump is caused by the strong radiative recombination continuum of iron, detected for the first time in SNRs. We also detected the strong radiative recombination structures of silicon and sulfur from IC 443 and G359.1-0.5. For all these SNRs, the electron temperatures determined from the bremsstrahlung and recombination continuum shapes are consistent with each other. Furthermore, volume emission measures determined independently from the fluxes of the bremsstrahlung and recombination components are also consistent. The results indicate the common origin of these components.

We further investigate the spatial distribution of the recombining plasma in W49B and IC 443. Both SNRs exhibit significant anisotropy. Combined with the spatial distribution, lifetime of highly-ionized atoms, metallicity of the recombining plasma, and surrounding environments, we discuss the formation process of this anomalous coexisting state of highly-ionized atoms and low-temperature electrons. We propose the plausible origin is supernova explosion in a dense circumstellar matter.

Contents

Chapter 1

Introduction

A supernova is a dynamic explosion of a star. The huge kinetic energy is released in the explosion. This kinetic energy of the ejecta is converted into the thermal energy of atoms and electrons via the shock wave heating and the hot plasma is formed. Hence, the supernova remnant (SNR) is composed of high-temperature ($\sim 10^7$ K) and low-density (~ 1 cm^{-3}) plasma.

The physical states of high temperature plasma in an SNR reflect the energy transduction condition. The traditional picture of the time evolution for the SNR plasma ionization states is described as follows. Soon after the supernova explosion, a blast shock wave goes through the progenitor star and ejecta atoms are shock-heated and fully ionized. Because of the high electron and atom density in this stage, however, highly ionized atoms rapidly recombine with electrons within one day. Almost all the ejecta atoms are in the first- or second-ionized states. This phase is well-observed in in the visible light. The ionization state in this phase last until the passage of a reverse shock which is formed when a swept-up interstellar matter dominate the ejecta mass.

When the reverse shock wave passes through the plasma, a particle's kinetic bulk motion is gradually randomized and transduced into the thermal motion. Among the constituents of plasma, massive ions with large electrical charges are firstly randomized and heated (ion temperature; $kT_{\rm i}$). Subsequently, electrons are heated (electron temperature; $kT_{\rm e}$) by the thermal transport from the ions. Finally, heated electrons gradually ionize the ions (ionization temperature; kT_z). Figure 1.1 shows the scheme of the plasma temperature time evolution. Because the plasma density in SNRs is so low (~ 1 cm^{-3}), it takes long time ($\sim 10^4$–10^5 years) to reach the equilibrium. In this manner, young SNRs ($<10^3$ years) obey the following relation:

$$kT_{\rm i} > kT_{\rm e} > kT_z. \tag{1.1}$$

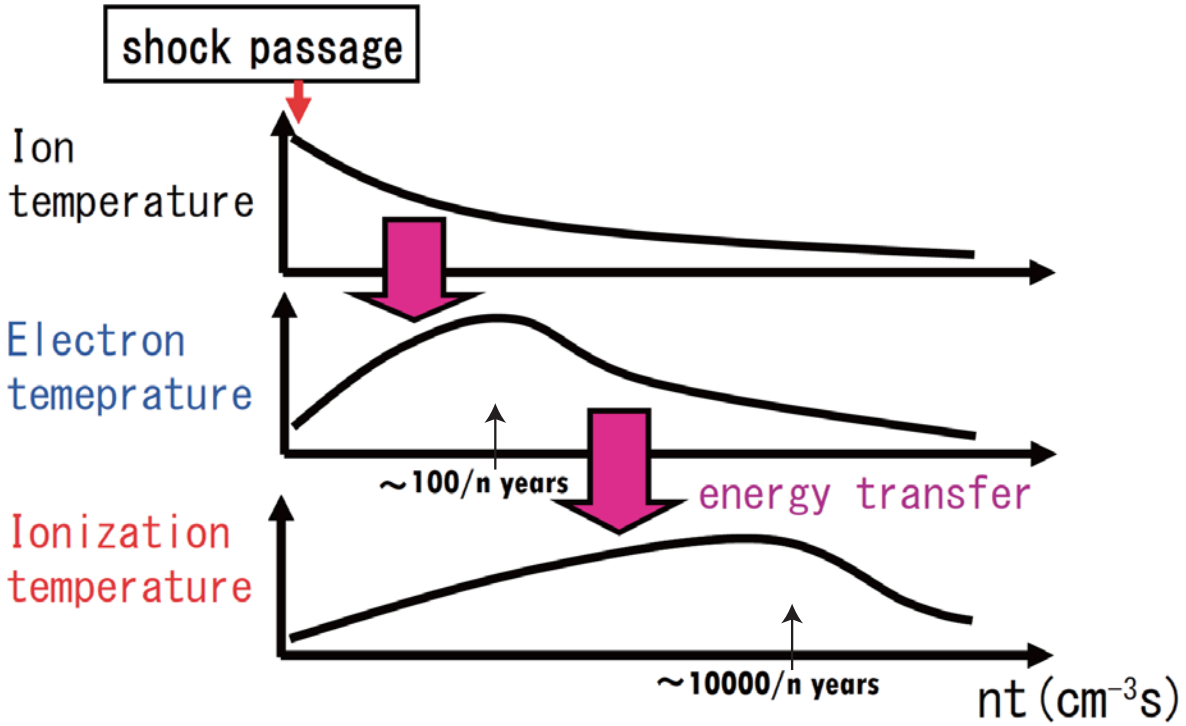

Fig. 1.1.—: Time evolution of temperature for the normal SNR plasma. n and t are plasma density and time after the reverse shock passage, respectively. Kinetic bulk energy of the shock wave is first tranduced into atoms (ions), then transferred into electrons. Heated electrons then ionize the atoms.

As for the ion temperature, there is no observational results so far. In principle, it can be determined by the Doppler broadening of line emission from ions. However, it requires detectors with very high energy resolution. Because it is difficult to determine the ion temperature in our actual condition, we concentrate on the study of electron and ionization temperatures [1].

The picture $kT_{\rm e} > kT_z$ is supported by many observational results of ASCA, which is the previous Japanese X-ray satellite. As we can see in figure 1.2, almost all the SNRs are in the underionized state ($kT_{\rm e} > kT_z$). Even old SNRs ($> 10^4$ years), such as Cygnus Loop, are still in the underionized state.

[1]The energy resolution of the CCD (current standard X-ray detector) is ∼130 eV (at 6 keV, FWHM). X-ray micro-calorimeter on board Astro-H (next Japanese X-ray satellite) has a very high energy resolution of 7 eV (FWHM) between 0.3–12keV. Because the expected Doppler broadening is the order of ∼10 eV, we can detect this effect using the micro-calorimeter. The determination of the ion temperature is an issue for the next-generation X-ray satellites and hence we will not discuss in this thesis.

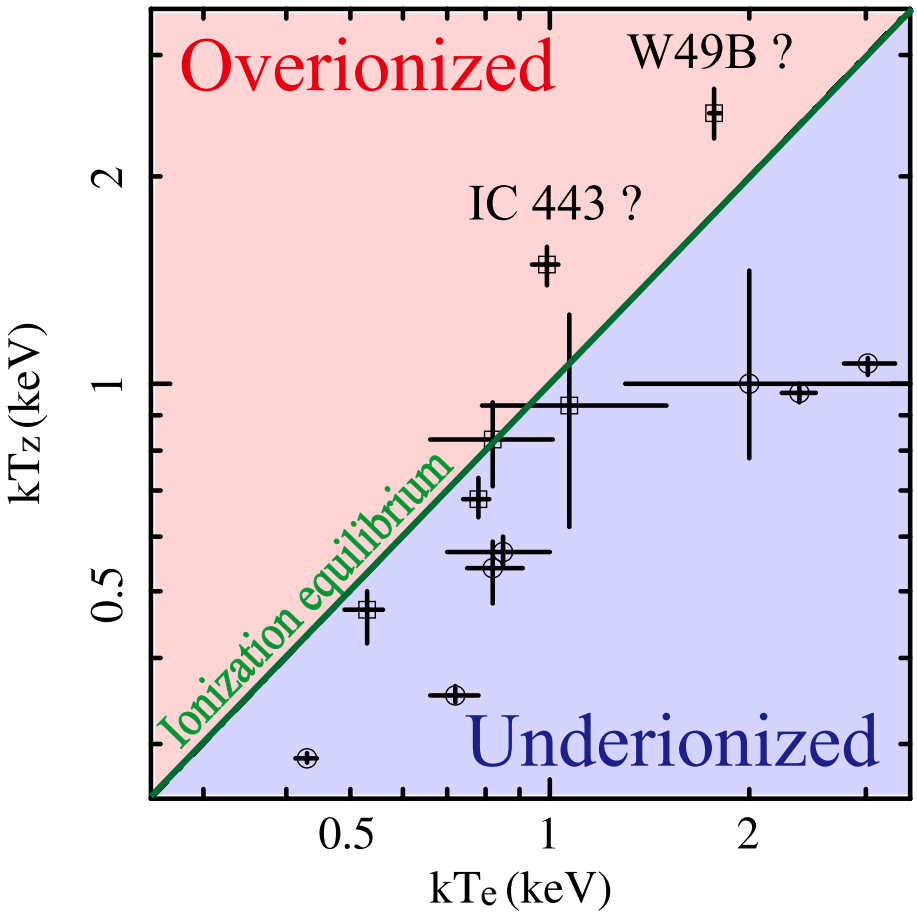

Fig. 1.2.—: Plasma states of the major supernova remnants obtained with the ASCA satellite (Kawasaki et al. 2005). A horizontal axis means electron temperature ($kT_{\rm e}$), which reflects the kinetic energy of electrons. A vertical axis is ionization temperature (kT_z), which indicates an ionization degree of heavy elements. The diagonal line represents $kT_{\rm e}$= kT_z and thus ionization equilibrium condition, and kT_z< $kT_{\rm e}$ (lower right) and kT_z> $kT_{\rm e}$ (upper right) regimes correspond to overionized and underionized conditions, respectively. Note that all remnants, except for W49B and IC 443, are in the underionized state.

Only two exceptions are W49B and IC 443. Using the ASCA data, Kawasaki et al. (2002, 2005) claimed that the plasma is in the overionized state ($kT_{\rm e} < kT_z$) for these two SNRs (figure 1.2). They derived $kT_{\rm e}$ from the spectral continuum shape, assuming it is completely originates from the bremsstrahlung emission. However, this method is not appropriate when there is a significant contribution of the non-thermal and/or other continuous spectral components. In order to check this validity, we examine these SNRs. We also examine G359.1-0.5, whose spectrum exhibits a signal of highly-ionized sulfur atoms (Bamba et al. 2000).

In principle, ionization dominates recombination in the underionized state. On the contrary, recombination should dominate ionization in the overionized plasma. Although Kawasaki et al. (2002, 2005) insist the existence of overionized plasma in two SNRs, they cannot find the recombination structure. If there are some structures originate from the recombination of atoms, the overionized plasma would become conclusive.

The emission from high temperature plasma dominates in X-ray band, hence X-ray data are suitable to investigate ionization states. Since the plasma states of SNRs can be known by measuring the intensities of the emission lines of heavy elements, the detector sensitivity for the line spectrum is essential to the accurate measurements. Suzaku, an actively working Japanese X-ray satellite, has good energy resolution, high efficiency, and low background level for diffuse sources. In particular, it is superior to the other X-ray missions, in the energy band corresponds to the K-shell emission structures of iron, which is one of the major products of supernova explosions.

In this thesis, we will focus on the study of X-ray emission from SNRs with highly ionized atoms utilizing the excellent performances of Suzaku. In chapter 2, we describe the reviews of supernovae and SNRs. The basic characteristics of the instruments onboard Suzaku are summarized in chapter 3. In chapter 4, we describe the classification of the thin thermal plasma and its detailed emission mechanisms. The following chapters provide the first results on the analyses of individual Galactic SNRs with Suzaku: W49B in chapter 5, IC 443 in chapter 6, and G359.1-0.5 in chapter 7. Combining all the works, we develop the discussions in chapter 8, and we finally summarize our findings in chapter 9.

Chapter 2

Supernovae and Supernova Remnants

Supernovae (SNe) are one of the most energetic events in the universe. Its typical kinetic energy is $\sim 10^{51}$ ergs[1]. This is as large as the total radiation energy that the sun radiates in its whole life time. The remnants created by the supernovae is called supernova remnants (SNRs). SNRs can yield information about the progenitors, explosion mechanism, and evolution of the remnants. This chapter is devoted to explain the basic characteristics of SNe and SNRs.

2.1 Supernovae

Around 300–500 SNe are discovered in a year, recently. In our Galaxy, however, SNe have not been discovered for ∼400 years [2]. SNe play quite important roles in several aspects. They scatter the heavy elements into the interstellar medium synthesized in the stars and the explosion via explosive nucleosynthesis. Furthermore, the shock wave generated by the SN explosions produce density fluctuation of an interstellar matter (ISM), which promote new star formation.

Figure 2.1 shows the fundamental classification scheme of SNe. It is traditionally based on the optical spectra. If a spectrum lacks absorption lines of hydrogen Balmer series, the SN is classified as Type I, otherwise as Type II. Type I SNe are sub-classified due to the presence of Si and He. The SNe with strong Si line are defined as Type Ia. The SNe without Si line and with He line are classified as Type Ib. Those without Si and He lines are Type Ic.

As we see from the definition, this classification does not reflect explosion mechanisms of SNe. The progenitors of Type Ia SNe are believed to be white dwarfs with nearly Chandrasekhar mass ($\sim 1.4 M_\odot$), while those of Type II to be massive stars ($M \gtrsim 10 M_\odot$). Details of the characteristics and origins of classified SNe are described in the following.

[1] This can be roughly estimated by a typical ejecta mass ($M \sim 1\ M_\odot$) and a typical expansion velocity ($v \sim$ 10,000 km s^{-1}) as $1/2Mv^2 \sim 1/2 \times (2 \times 10^{33}$ g) $\times (10^9$ cm/s$)^2 \sim 10^{51}$ ergs.

[2] There are some Galactic supernova remnants whose ages are estimated to be younger than 400 years. However, these SNe were not observed by human.

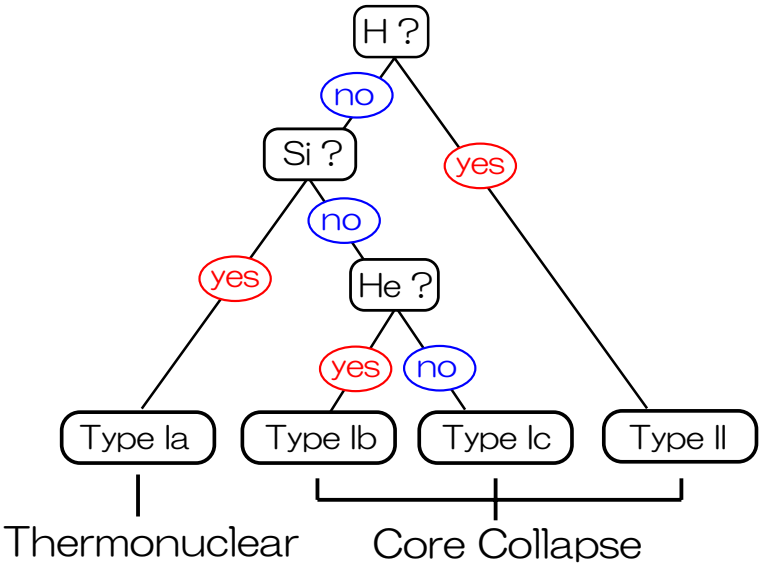

Fig. 2.1.—: Classification scheme for supernovae.

Type Ia

Type Ia SNe are observed in all types of galaxies. They are even observed in the elliptical galaxies where the star formation has finished and no massive stars exist. The lack of hydrogen revealed by optical spectra indicates that the progenitors have no hydrogen envelope. These facts indicate it is plausible that Type Ia explosions originate from thermonuclear explosions of mass-accreting white dwarfs in binary systems.

When the mass of the white dwarf reaches about the Chandrasekhar limit ($\sim 1.4 M_{\odot}$), the gravity exceeds the electron degeneracy pressure. Then, the carbon core burning occurs. Nuclear fusion advances explosively, and the star is totally disrupted. This explosion leaves no compact star nor black hole. Nucleosynthesis models of Type Ia SNe predict that the elements such as Si and Fe are selectively synthesized, while those as O, Ne, and Mg are hardly synthesized (Nomoto et al. 1984, Iwamoto et al. 1999).

Type II

Because Type II SNe are concentrated in the spiral galaxy's arm, it is plausible that their progenitors are massive stars. A high mass star ($\geq 10 M_{\odot}$) finally has a Fe core. When the internal temperature exceeds $\sim 3 \times 10^9$K, photo-disintegration of Fe nuclei takes place.

$$
\begin{aligned}
^{56}\mathrm{Fe} &\rightarrow 13\ ^{4}\mathrm{He} + 4\mathrm{n} - 124.4\ \mathrm{MeV} \\
^{4}\mathrm{He} &\rightarrow 2\mathrm{p} + 2\mathrm{n} - 28.3\ \mathrm{MeV}\ ,
\end{aligned}
$$

Because this is an endoergic reaction, the star cannot support its gravity and collapses. The gravitational energy released by the infalling matter creates a shock wave and the shock propagates outward. The total energy generated by the gravitational collapse is $\sim 10^{53}$ ergs. Because most

of the explosion energy is carried out by neutrinos, the kinetic energy of the shock wave becomes $\sim 10^{51}$ ergs. This explosion leaves a neutron star or a black hole. Nucleosynthesis models of Type II SNe predict that O, Ne, and Mg, as well as Si and Fe are synthesized during this explosion (Thielemann et al. 1996).

Type Ib

Although the optical spectra of Type Ib SNe lack hydrogen absorption lines, the property of light curves is very similar to Type II. Furthermore, Type Ib SNe are observed only in spiral galaxies and star forming regions. These facts indicate that the progenitors of Type Ib SNe are the same as Type II (massive stars which have lost their hydrogen envelope). The plausible candidate is a Wolf-Rayet star, because they lose an outer hydrogen envelope by the strong stellar wind.

Type Ic

It is believed that the progenitors of Type Ic are also massive stars. The plausible candidate is a Wolf-Rayet star which has lost an outer hydrogen and helium envelope. A few fraction of the Type Ic SNe is said to be accompanied with γ-ray bursts (GRBs). For example, the optical spectrum of GRB980425 is very similar to Type Ic. The broad absorption feature indicate the velocity of elements range from 10-20% of the light speed. From these facts, it is concluded that the progenitor of this GRB is a high mass star with $\sim 40 M_{\odot}$, and associated with a hypernova phenomenon. Similar phenomena are also detected from GRB030329 and GRB031203.

2.2 Supernova Remnants

274 SNRs are identified in our Galaxy (Green 2009), and about a half are observed in X-rays. In this chapter, we explain the shock heating process, and evolution and classification of SNRs.

2.2.1 Shock Wave Heating

Because the shell of an SNR expands supersonically, a shock wave is formed. As the shock wave passes, the gas is compressed and heated. Here we consider a coordinate system in figure 2.2 (right). Conservation of mass, momentum, and energy across the shock front can be expressed as

$$\rho_u v_u = \rho_d v_d \tag{2.1}$$

$$\rho_u v_u^2 + p_u = \rho_d v_d^2 + p_d \tag{2.2}$$

$$\frac{1}{2}v_u^2 + w_u = \frac{1}{2}v_d^2 + w_d \ , \tag{2.3}$$

where ρ, v, p, and w are the density, velocity, pressure, and enthalpy of upstream (subscript u) and downstream (subscript d). Assuming the fluid is ideal gas, the enthalpy is given as

$$w = C_p T = \frac{\gamma p}{(\gamma - 1)\rho} \ , \tag{2.4}$$

where γ is the specific heat ratio ($= C_p/C_V$).

From equations 2.1, 2.2, 2.3, and 2.4, and assuming the strong shock ($p_d/p_u \gg 1$), we obtain

$$\frac{\rho_u}{\rho_d} = \frac{v_d}{v_u} = \frac{\gamma - 1}{\gamma + 1} \tag{2.5}$$

$$\frac{T_u}{T_d} = \frac{p_d}{p_u}\frac{\gamma - 1}{\gamma + 1} \tag{2.6}$$

$$v_u^2 = \frac{(\gamma + 1)p_d}{2\rho_u} \tag{2.7}$$

$$v_d^2 = \frac{(\gamma - 1)^2 p_d}{2(\gamma + 1)\rho_u} \ . \tag{2.8}$$

Because $v_u = v_s$ (see figure 2.2), we can derive the mean post-shock temperature using equations 2.5 and 2.8 as:

$$kT_d = \mu m_{\rm H}\frac{p_d}{\rho_d} = \frac{2(\gamma - 1)}{(\gamma + 1)^2}\mu m_{\rm H} v_s^2 \ , \tag{2.9}$$

where k, μ, and $m_{\rm H}$ are the Boltzmann constant, the mean atomic weight, and the hydrogen mass, respectively. Assuming the non-relativistic single atomic gas ($\gamma = 5/3$), we obtain the relations of $\rho_d/\rho_u = 4$ and $v_d/v_u = 1/4$. The post-shock temperature is described as

$$kT_d = \frac{3}{16}\mu m_{\rm H} v_s^2 \ . \tag{2.10}$$

As we can see from this equation, the shock wave heating can be understood as the energy conversion of the bulk kinetic energy into the randomized thermal energy.

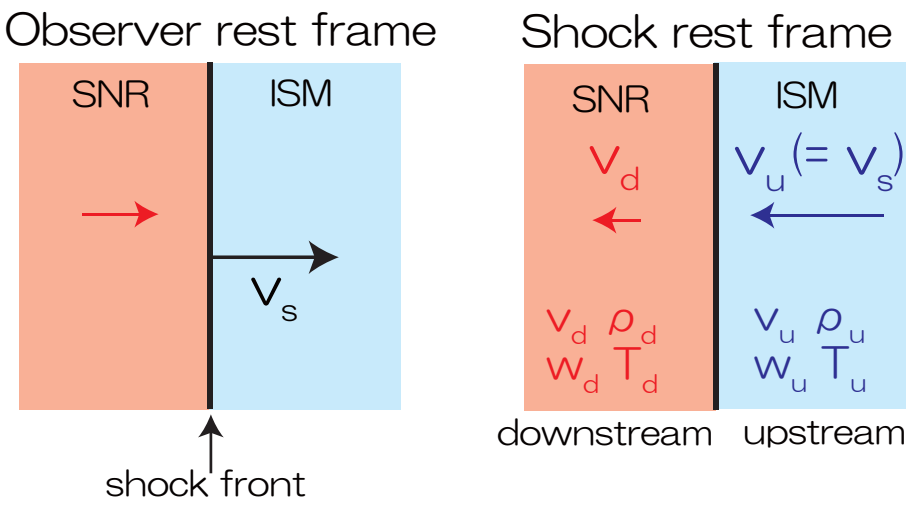

Fig. 2.2.—: A schematic view of the shock wave in observer rest frame (left) and shock rest frame (right). v, ρ, p, w, and T are the velocity, density, pressure, enthalpy, and temperature, respectively.

2.2.2 Evolution

Basically, an SNR is composed of an expanding ejected material (ejecta) and a swept-up ISM. The evolution phase of an SNR is mainly determined by the relation between the mass of the ejecta ($M_{\rm Ej}$) and swept-up ISM ($M_{\rm ISM}$). We here assume that the density of the ambient medium is uniform [3].

1) $M_{\rm ISM} \ll M_{\rm Ej}$: Free Expansion Phase

The ejecta expands without deceleration. The expansion velocity ($\sim 10^4$ km s^{-1} as we see below) is much larger than the sound speed in the ambient gas (~ 10 km s^{-1}), and hence shock wave (blast wave) precede the ejecta. Since most of the explosion energy (E) is released kinetically [4], the expansion velocity (v_s) and the radius (R_s) of the shock front can be expressed by

$$v_s = \sqrt{\frac{2E}{M_{\rm Ej}}} = 1.0 \times 10^9 \left(\frac{E}{10^{51}\ {\rm erg}}\right)^{1/2} \left(\frac{M_{\rm Ej}}{M_\odot}\right)^{-1/2} \quad [{\rm cm\ s^{-1}}] \ , \tag{2.11}$$

$$R_s = v_s t \ , \tag{2.12}$$

where t is the time since the explosion. The mass of the ISM swept-up by the blast wave is described as

$$M_{\rm ISM} = \frac{4}{3}\pi R_s^3 \mu m_{\rm H} n_0 \ , \tag{2.13}$$

where n_0 is hydrogen number density of the ISM. Since the free expansion phase continues until $M_{\rm ISM}$ becomes comparable to $M_{\rm Ej}$, its timescale can be approximately estimated from equation 2.11, 2.12, and 2.13 to be

[3] The detailed descriptions are shown in Truelove & McKee (1999) for young stages (from free expansion phase through Sedov phase) and Cioffi et al. (1988) for evolved stages (radiation phase).

[4] The energy converted into thermal energy is only 2–3% in this phase.

$$t \sim 1.9 \times 10^2 \left(\frac{E}{10^{51}\ \mathrm{erg}}\right)^{-1/2} \left(\frac{M_{\mathrm{Ej}}}{M_\odot}\right)^{5/6} \left(\frac{\mu}{1.4}\right)^{-1/3} \left(\frac{n_0}{1\ \mathrm{cm}^{-3}}\right)^{-1/3} \quad [\mathrm{yr}]\ . \tag{2.14}$$

Therefore, this phase typically continues for a few hundred years.

2) $M_{\mathrm{ISM}} \sim M_{\mathrm{Ej}}$: Transition Phase

In this phase, the interaction with the ISM cannot be ignored, although it is not yet dominant. The swept-up ISM decelerates the ejecta and causes another shock wave (reverse shock). The ejecta is compressed and heated by the reverse shock. The boundary between the ISM and the ejecta is called the "contact discontinuity". Note that reverse shock initially propagate outward. When M_{ISM} becomes greater than M_{Ej}, the reverse shock propagates back to the center. Most of young SNRs, such as Tycho, are probably in this stage.

3) $M_{\mathrm{ISM}} \geq M_{\mathrm{Ej}}$: Adiabatic (Sedov) Phase

The blast wave is decelerated by the swept-up ISM, but the energy loss via radiation is still negligible. Therefore, the SNR expands adiabatically. In this stage, the shock evolution can be approximated by a point explosion in a uniform medium [5]. The gas flow can be characterized by two parameters, E and n_0. The radius (R_s) and velocity (v_s) of the blast wave, and the mean temperature just behind the shock front (T_s) are written as

$$R_s = 4 \times 10^{19} \left(\frac{t}{10^4\ \mathrm{yr}}\right)^{2/5} \left(\frac{E}{10^{51}\ \mathrm{erg}}\right)^{1/5} \left(\frac{n_0}{1\ \mathrm{cm}^{-3}}\right)^{-1/5} \quad [\mathrm{cm}] \tag{2.15}$$

$$v_s = \frac{dR_s}{dt} = 5 \times 10^7 \left(\frac{t}{10^4\ \mathrm{yr}}\right)^{-3/5} \left(\frac{E}{10^{51}\ \mathrm{erg}}\right)^{1/5} \left(\frac{n_0}{1\ \mathrm{cm}^{-3}}\right)^{-1/5} \quad [\mathrm{cm\ s}^{-1}] \tag{2.16}$$

$$T_s = 3 \times 10^6 \left(\frac{t}{10^4\ \mathrm{yr}}\right)^{-6/5} \left(\frac{E}{10^{51}\ \mathrm{erg}}\right)^{2/5} \left(\frac{n_0}{1\ \mathrm{cm}^{-3}}\right)^{-2/5} \quad [\mathrm{K}]\ . \tag{2.17}$$

In this phase, the density of the swept-up ISM is much higher than that of ejecta, and hence X-ray emission is dominated by the ISM. The Sedov phase lasts for a few ten thousand years. Until the end of this phase, $\sim 70\%$ of the initial explosion energy (bulk kinetic energy) is transduced into thermal energy of the swept-up ISM (Chevalier 1974).

Radiative Cooling Phase

In the Sedov phase, the temperature behind the shock decreases with time (equation 2.17). The cooling rate gradually increases, and the evolution becomes no longer adiabatic. When the temperature cools down to $\sim 3{\times}10^5$ K, electrons efficiently recombine with abundant carbon and oxygen, and radiate ultraviolet emission lines. The shell is driven by the pressure of the internal gas obeying $PV^\gamma = \mathrm{const.}$, where P and V are the mean pressure and the volume of the internal

[5] This is explained by a self-similar solution by Sedov (1959). Therefore, this phase is often called as "Sedov phase".

gas, respectively. If we assume the non-relativistic single atomic gas ($\gamma = 5/3$), the shock expands with the time as

$$R_s \propto t^{2/7} \ . \tag{2.18}$$

When the temperature further cools down, the pressure can be ignored and the cool shell expands with the conserved radial momentum ($M_s v_s = $ const., where M_s is the mass of the shell). The shock expands as

$$R_s \propto t^{1/4} \ . \tag{2.19}$$

When the shock speed becomes comparable to the proper motion of the ISM (10–20 km s^{-1}), the SNR lose its boundary. This phase is called as "Disappearance phase". The age of SNRs in this phase is larger than $\sim 10^6$ years.

2.2.3 Classification

Based on the radio morphology, SNRs are classified mainly into three classes; shell-type, plerion-type, and composite. These classification is summarized in table 2.1. Among 274 Galactic SNRs, ∼65% , ∼4% , and ∼10% are classified as shell-type, plerion-type, and composite, respectively. Remains are not firmly classified. Addition to these, Rho & Petre (1998) claimed a new category of SNRs, called "mixed-morphology" SNRs. They have shell-like morphology in radio band, and center-filled one in X-rays. Here we mention each type.

Shell-type

This type has limb brightened morphology in both X-ray and radio bands. Figure 2.3a shows one example. X-ray emission is thermal or non-thermal. Examples for the former are Cassiopeia A, Tycho, and Kepler. Almost all the observed SNRs in this category are considered to be between free expansion and adiabatic phases. Examples for the latter are SN1006 and RX J1713.7-3946. The origin of the non-thermal X-rays is synchrotron radiation from relativistic electrons accelerated to the energy order of TeV by a blast wave. On the other hand, the origin of the non-thermal radio photons is due to electrons accelerated up to the energy order of GeV.

Plerion-type

This type shows non-thermal emission with center-filled morphology. Figure 2.3b shows one example. The origin of X-rays is synchrotron radiation from a neutron star or its nebula. Examples are, Crab Nebula, 3C 58, and G21.5-0.9.

Composite

We can see both shell-like and center-filled morphology from this category. In figure 2.3c, we show one example. The central object is associated with a pulsar, while the emission from limb is

Table 2.1—: Classification of SNRs.

		Shell-like ?	Center-filled ?
Shell-type SNR		yes	no
Plerion-type SNR		no	yes
Composite SNR		yes	yes
Mixed-morphology SNR	(Radio)	yes	no
	(X-ray)	no	yes

associated with the blast wave. Thus, this is a mixture of the shell-type and plerion-type. Examples are, CTB 109, Vela SNR, and G11.2-0.3.

Mixed-morphology

This is another group of SNRs which exhibit different morphology in X-ray and radio bands. One example is shown in figure 2.3. The bulk of X-ray emissions is thermal, mainly originates from the swept-up ISM. Examples are, W28, W44, and 3C 391. The population represents ∼10% of all Galactic SNRs and as much as ∼25 % of all X-ray detected Galactic SNRs. Rho & Petre (1998) proposed two formation mechanisms to explain this category. One is a cloud evaporation model. In this scenario, many small interior clouds evaporate and emit X-rays. The other is a fossil conduction model (Cox et al 1999, Shelton et al. 1999a). This predicts the hot interior plasma gradually became uniform by thermal conduction and creates centrally brightened X-ray morphology. X-ray emission from the shell, on the other hand, became undetectable because the temperature became too low ($\sim 10^6$ K) and absorbed by the ISM.

In this thesis, we analyze W49B, IC 443, and G359.1-0.5. All exhibit center-filled morphology in X-rays, and a shell-like feature in the radio band. So we can say, all these SNRs are classified into the mixed-morphology type.

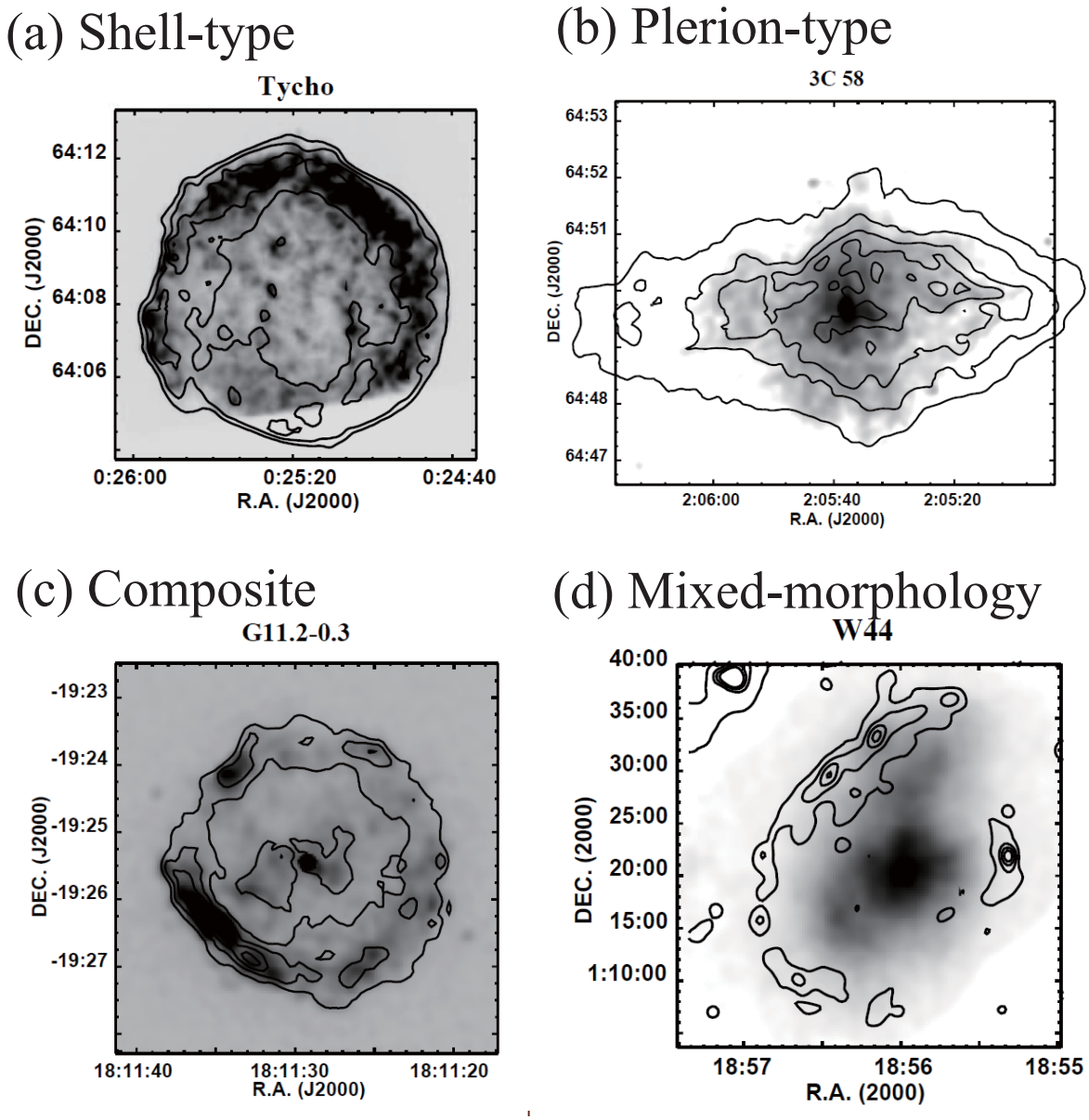

Fig. 2.3.—: Examples of classified SNRs. Gray scale and contours indicate X-ray and radio maps, respectively. (Credit: Chandra Supernova Remnant Catalog. http://hea-www.cfa.harvard.edu/ChandraSNR/) (a) Shell-type SNR; Tycho. Gray scale: 0.3-10 keV by Chandra. Contour: 1.375 GHz by VLA. (b) Plerion-type SNR; 3C 58. Gray scale: 0.3-10 keV by Chandra. Contour: 21 cm by VLA. (c) Composite SNR; G11.2-0.3. Gray scale: 0.3-10 keV by Chandra. Contour: 21 cm by VLA. (d) Mixed-morphology SNR; W44. Gray scale: 0.7-10 keV by ASCA. Contour:1.4 GHz by VLA. These figures are taken from Kawasaki (ph.D.).

Chapter 3

Instruments

Suzaku is the Japan's fifth X-ray astronomy satellite. Throughout this thesis, we use the data obtained with Suzaku. The X-ray CCD (XIS) onboard Suzaku has good energy resolution, high efficiency, and low and stable background for diffuse sources. All these characteristics are essential for the accurate analyses of SNRs. In this chapter, we review the Suzaku satellite, onboard instruments, and onboard calibration issues.

3.1 Suzaku

Suzaku (Mitsuda et al. 2007) was launched on July 10, 2005, and put into a near circular orbit at a ~ 570 km altitude with an inclination angle of $\sim 31^\circ$ and orbital period of ~ 96 minutes. Figure 3.1 shows a schematic view of Suzaku. The spacecraft length is 6.5 m along the telescope axis and the total weight is ~ 1700 kg.

Suzaku carries three scientific detector systems: the X-ray Imaging Spectrometer (XIS: Koyama et al. 2007a), the Hard X-ray Detector (HXD: Takahashi et al. 2007; Kokubun et al. 2007), and the X-ray Spectrometer (XRS: Kelley et al. 2007). The XRS and four XIS cameras are located at the focal plane of the corresponding X-ray Telescope modules (XRT: Serlemitsos et al. 2007). The capability of these instruments is summarized in table 3.1.

The XRS is the first orbiting X-ray microcalorimeter, and supposed to be one of the main instruments of Suzaku. However, it became nonoperational due to the evaporation of the liquid helium. The HXD is a non-imaging, collimated detector, which covers band pass of 10–600 keV. In this thesis, we do not use the XRS and HXD.

Table 3.1—: Overview of Suzaku capabilities (Mitsuda et al. 2007).

XRT	Focal length	4.75 m
	Field of view	$20'$ (@ 1 keV) / $14'$ (@ 7 keV)
	Effective area	440 cm^2 (@ 1.5 keV) / 250 cm^2 (@ 8 keV)
	Angular resolution	$2'$ (Half power diameter)
XIS	Field of view	$17.'8 \times 17.'8$
	Bandpass	0.2–12 keV
	Pixel grid / size	1024 × 1024 / 24 μm × 24 μm
	Energy resolution	∼130 eV (@ 6 keV: FWHM)
	Effective area	330 (FI) & 370 (BI) cm^2 (@ 1.5 keV)
	(including XRT)	160 (FI) & 110 (BI) cm^2 (@ 8 keV)
HXD	Field of view	$4.°5 \times 4.°5$ (≥ 100 keV) / $34' \times 34'$ (≤ 100 keV)
	Band pass	PIN:10–70 keV / GSO: 40–600 keV

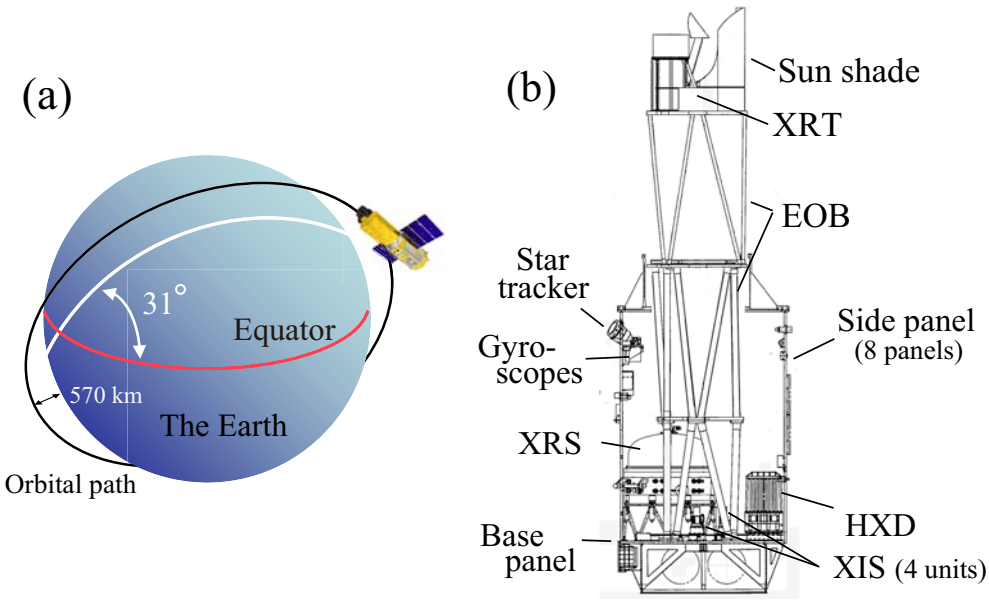

Fig. 3.1.—: (a) Schematic view of Suzaku and its orbital path. (b) Side view of Suzaku with the internal structure after the EOB extension (Mitsuda et al. 2007).

3.2 XRT

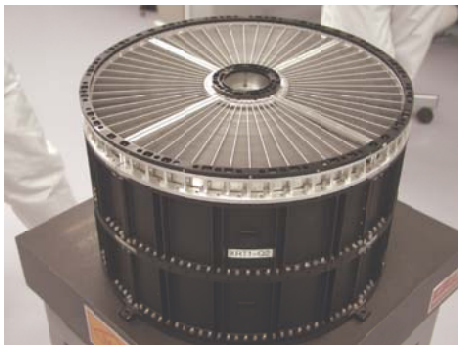

Fig. 3.2.—: Picture of the XRT (Serlemitsos et al. 2007).

There are five XRT modules (figure 3.2). One is equipped for the XRS, and the others are for the XIS. All XRTs are co-aligned to image the same region of the sky. The XRT is configured to form a Wolter I grazing-incidence reflective optics (figure 3.3). Incident X-rays are reflected twice by the parabolic and hyperbolic surfaces, and are condensed to the focal plane, when their incident angle is less than $\sim 1^\circ$. In order to increase the effective area, each XRT module has 175 nested thin foil layers. Because it is difficult to construct a precise Wolter geometry with thin foils, both the primary and secondary reflectors are approximated by simple cones.

Figure 3.4a shows the energy dependence of the total on-axis effective area of the four XRTs, including the detector efficiency. It is compared with those of other X-ray missions. The XRT provide a large efficiency in the energy range of 0.2–12 keV. The effective area of the four XRT modules is larger than Chandra in most energy band, and comparable to XMM-Newton above $\sim$5 keV. As shown in figure 3.4b, the effective area is a function of the off-axis angle. This effect is called "vignetting". The effect is calculated by the ray-tracing simulator, and confirmed by the observational data of Crab Nebula. The response of the XRT is described by Ancillary Response Files (ARFs). In all spectral analyses in following chapters, we use ARFs generated by `xissimarfgen` software (Ishisaki et al. 2007).

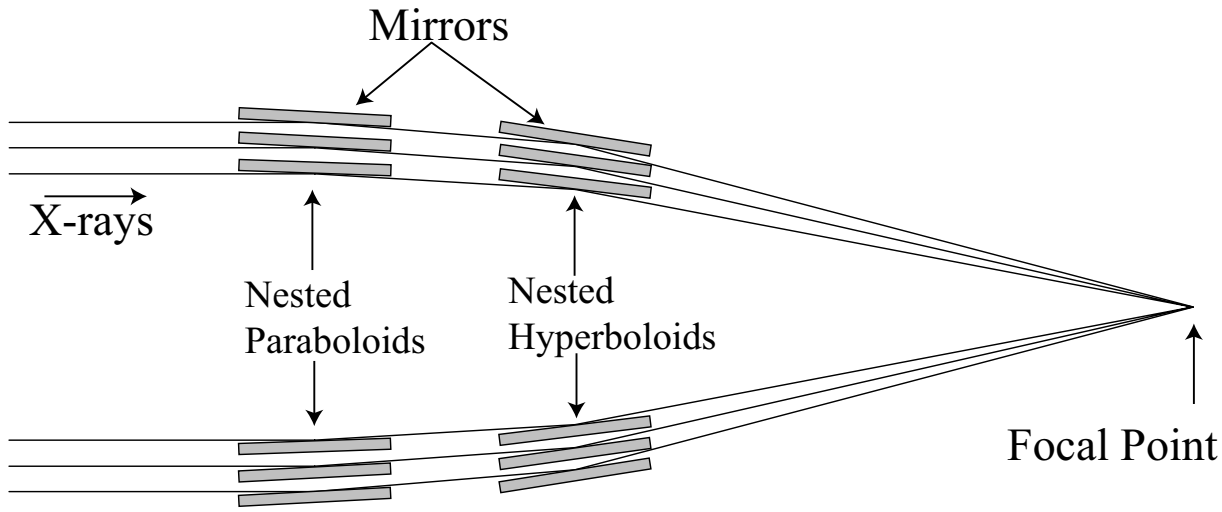

Fig. 3.3.—: Sectional view of Wolter I reflecting optics. Incident X-rays are reflected twice at very shallow angles and concentrated at the focal point.

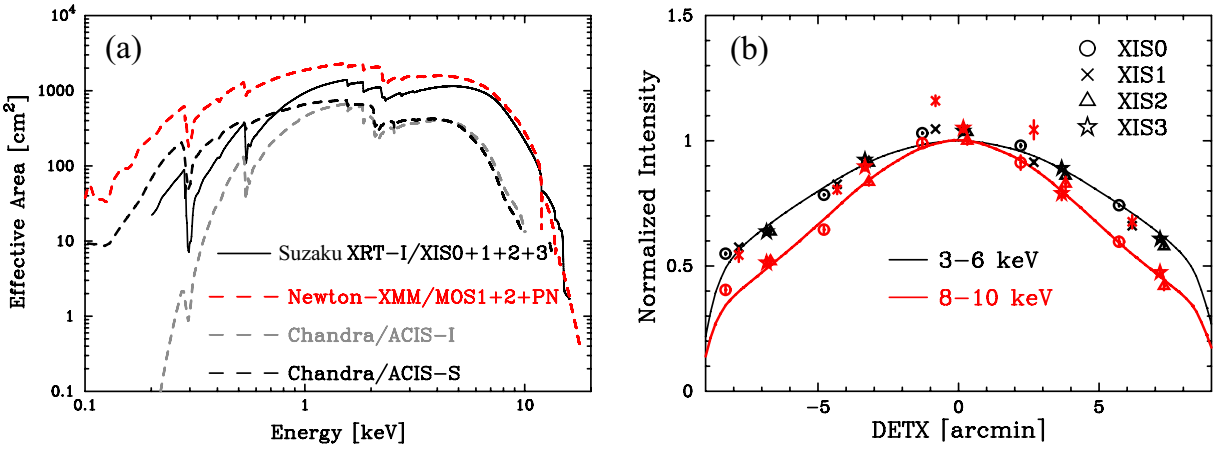

Fig. 3.4.—: (a) Total effective area of the XRT (combined with the XIS). Those of other X-ray missions (XMM-Newton and Chandra) are also shown for comparison. (b) Off-axis angle dependence of the effective area normalized at the optical axes. Data points are the Crab nebula data, and solid lines are the simulated model (Serlemitsos et al. 2007).

3.3 XIS

3.3.1 Overview

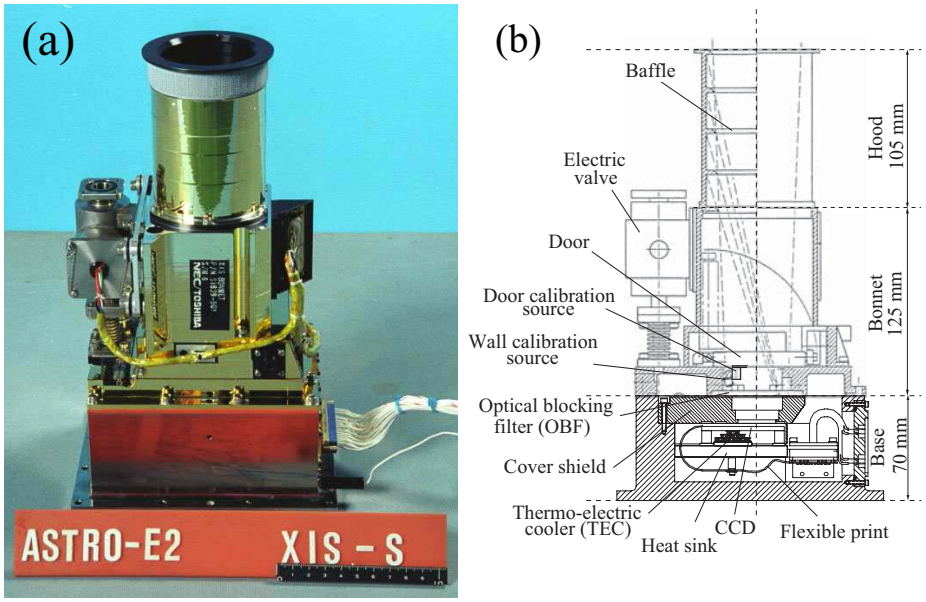

Fig. 3.5.—: (a) Picture and (b) side view of the XIS (Koyama et al. 2007a).

The XISs (figure 3.5) have four sensors (XIS 0, 1, 2, and 3), and each sensor has one charge coupled device (CCD) chip. Each CCD consists of four segments (A, B, C, and D) with a dedicated read-out node. Three sensors (XIS 0, 2, and 3) contain front-illuminated (FI) CCDs, and the other (XIS 1) has a back-illuminated (BI) CCD. Combined with the XRT, the field of view is $17'.8 \times 17'.8$. There are ^{55}Fe calibration sources located on a side wall of the bonnet (figure 3.5b). ^{55}Fe decays to leave ^{55}Mn via electron capture mainly from the K-shell. Subsequently, a fluorescent X-ray is emitted (Kα: 5.895 keV) accompanied by an electron transition. Calibration sources illuminate the two far-end corners from the read-out node of the imaging area (figure 3.6).

The depletion layer of the BI CCD ($\sim 42\mu$m) is thinner than that of the FI CCD ($\sim 65\mu$m). The quantum efficiency at high energy of the BI is, therefore, lower than FI (figure 3.7). The clocks of the XIS are generated by the sequence in the analog electronics according to the micro-code. The "normal" clocking mode has imaging capability with time resolution of 8 second. In all observations described in this thesis, the XIS were operated in the normal mode.

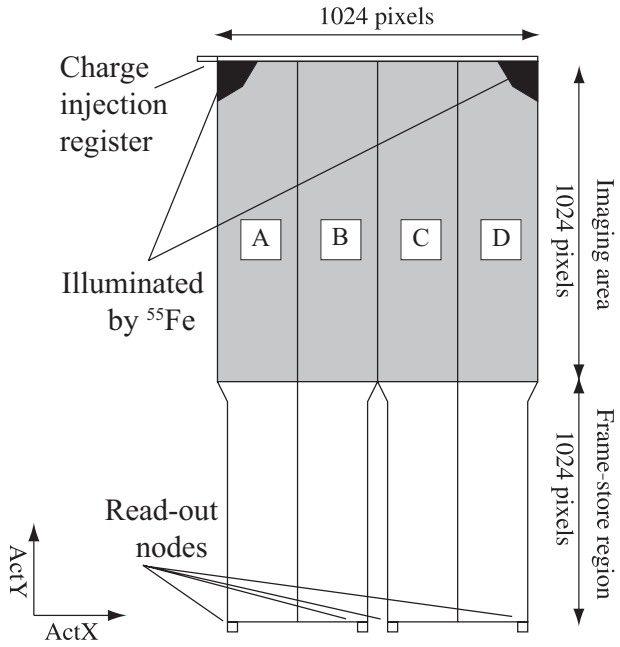

Fig. 3.6.—: Schematic view of the XIS CCD (Koyama et al. 2007a).

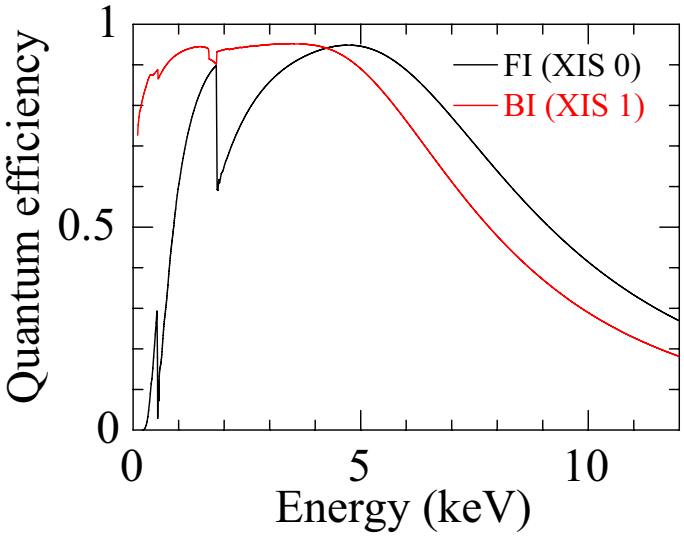

Fig. 3.7.—: Quantum efficiency of the XIS as a function of incident photon energy (Koyama et al. 2007a).

Even if incident X-rays are monochrome, the spectral shape is complicated (figure 3.8). This spectral response is called "response function", which is examined by ground experiments. The response function is included in the response matrix files (RMFs), which can be made using `xisrmfgen` software (Ishisaki et al. 2007).

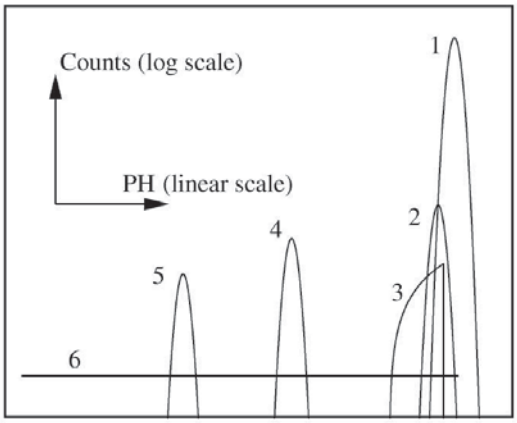

Fig. 3.8.—: XIS response to monochromatic X-rays. There are (1) main peak, (2) sub peak, (3) triangle component, (4) Si escape peak, (5) Si fluorescent peak, and (6) constant component. (Matsumoto et al. 2006)

Figure 3.9 shows non X-ray background (NXB) spectra obtained while Suzaku was pointed toward the night earth. Since the orbit altitude of Suzaku is much lower than that of XMM-Newton or Chandra, Suzaku is less influenced by solar flares and keeps the very stable NXB level. Hence, the XIS is sensitive to diffuse sources.

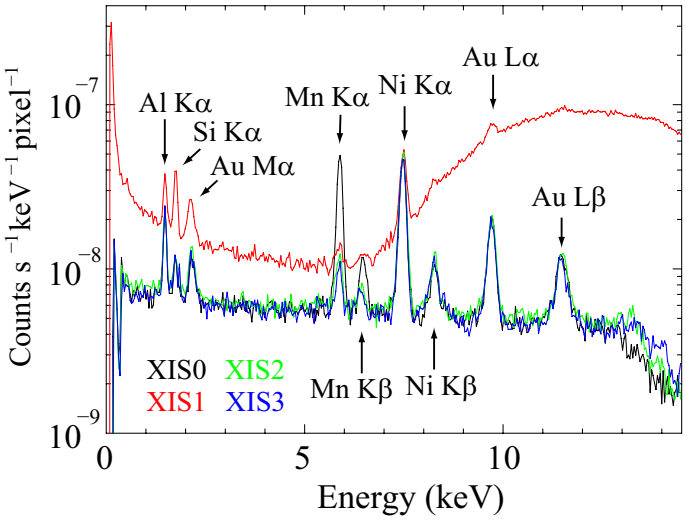

Fig. 3.9.—: XIS non X-ray background spectra (Tawa et al. 2008). Note that the count rate of the BI (XIS 1) is higher than that of the FI (XIS 0, 2, and 3) especially above ∼7 keV.

3.3.2 On-orbit Performance

Since the launch, the energy gain and resolution of the XIS is gradually degrading due to the radiation damage (figure 3.10). The damage increases a charge-transfer inefficiency (CTI).

In order to mitigate this effect, we (= XIS team members) have carried out two methods utilizing the charge injection technique. Using this technique, we can inject an arbitrary amount of charge in arbitrary positions (Prigozhin et al. 2004, Bautz et al. 2004, LaMarr et al. 2004, Prigozhin et al. 2008). One method we have carried out is "a checker-flag charge injection (CFCI)" [1], and the other is "a spaced-row charge injection (SCI)". All the results using these two methods have been implemented to the Suzaku calibration database and applied to all the observational data. In this section, we summarize the CFCI and SCI, and mention the observing condition in this thesis.

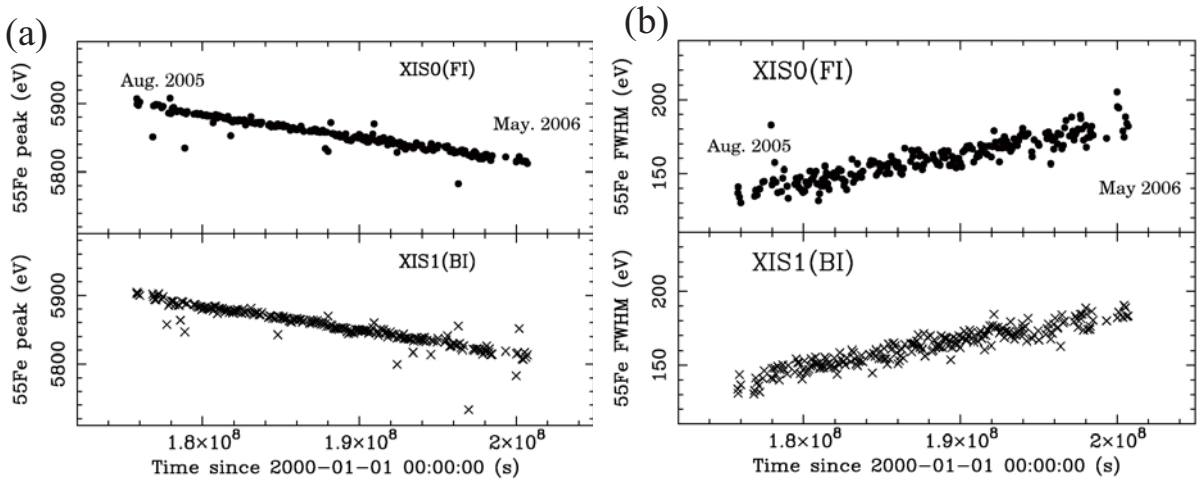

Fig. 3.10.—: Time history of the (a) energy gain and (b) energy resolution of the Mn Kα line from the ^{55}Fe calibration sources (Koyama et al. 2007a).

[1] We can obtain a checker flag pattern by these injected packets in the X-ray image (figure 3.11b) because of the onboard event-detection algorithm. Therefore, we call this technique a "checker flag" charge injection.

Checker-flag Charge Injection (CFCI)

We summarize CFCI on-orbit experiments. The details are summarized in Ozawa et al. (2008, 2009b). We briefly explain the CFCI method (figure 3.11). First, we inject a “test” charge packet into the top CCD row. Then, after the gap of a few rows, five continuous packets are injected with the same amount of charge of the test packet. The former four are called “sacrifice”, while the last one is called “reference”. ”Test” loses its charge by the charge traps. On the other hand, ”reference” does not lose the charge because the traps are already filled by ”sacrifice”. Thus, we can measure the charge loss by comparing the pulse-height of ”reference” and ”test”.

We have conducted CFCI experiments six times in orbit. Effective exposure time ranges from a few to ∼20 ks, and the equivalent X-ray energy of the injected charge packets ranges from 0.3 to 8 keV.

Using this CFCI capability, we can precisely measure the CTI of each CCD column. By applying the column-to-column CTI correction, the energy scale have been greatly reduced, and the over-all energy resolution have been also improved.

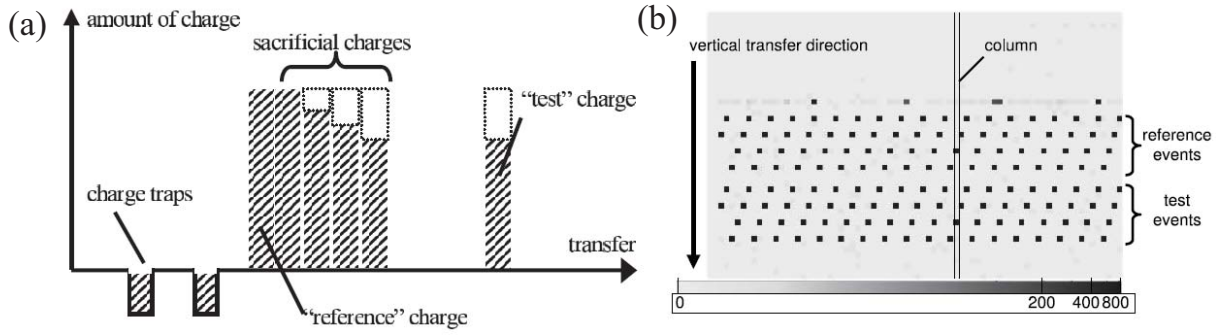

Fig. 3.11.—: (a) Schematic view of the charge injection. (b) Frame image of the XIS during the charge-injection experiment. The gray scale shows the pixel level. Note that the sacrificial packets are not displayed due to the event detection algorithm (Nakajima et al. 2008).

Here we show some results after the CTI correction. Figure 3.12a shows center energies of the Mn I Kα line as a function of time. The time-averaged uncertainty of the absolute energy is greatly improved to $\sim \pm$ 0.1 % . Figure 3.12b shows the center energies of the O VIII Kα line from the supernova remnant 1E 0102.2 − 7219. The uncertainty of the absolute energy is $\sim \pm$ 0.2%.

Figure 3.13 shows the energy resolution of the Mn I Kα line after our new CTI correction. We also plot the results of the traditional correction method. The energy resolution has greatly improved by the column-to-column CTI correction using the results of the CFCI experiments.

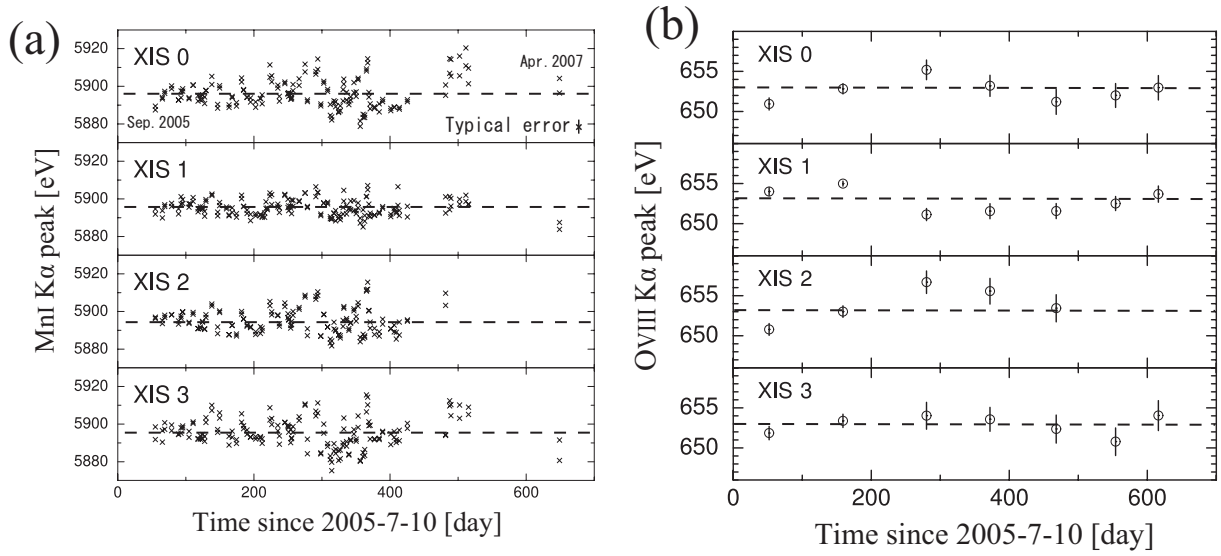

Fig. 3.12.—: Center energy after the CTI correction for (a) the Mn I Kα line from onboard calibration sources and (b) the O VIII Kα line from 1E 0102.2 − 7219. The theoretical centroids are shown with dotted lines (Ozawa et al. 2009b).

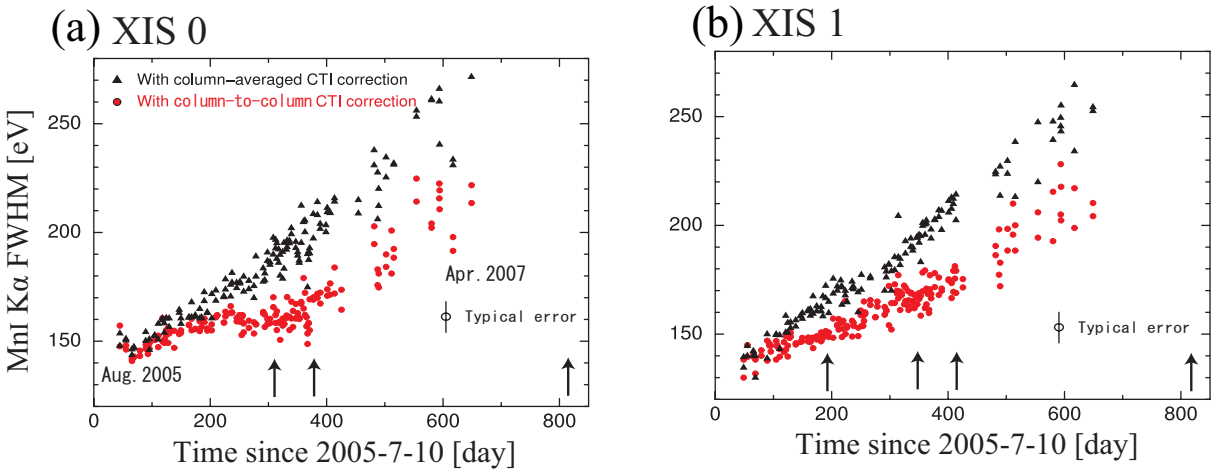

Fig. 3.13.—: Energy resolution of Mn I Kα for (a) XIS 0 and (b) XIS 1. Arrows indicate the days we performed the CFCI experiments. We compare the results of a new column-to-column (circle) and traditional column-averaged (triangle) CTI corrections. Note our new methods has greatly improved the energy resolution (Ozawa et al. 2009b).

Spaced-row Charge Injection (SCI)

The new CTI correction using the CFCI have greatly improved the energy resolution. The degradation, however, cannot be fully restored using this method. The charge injection can be used in another way to mitigate the effect of the radiation damage. The SCI technique can reduce the CTI actively and improve the energy resolution. In the SCI, a charge is injected into CCD rows periodically. The injected charge fills the charge traps as a "sacrifice".

The XIS performed the SCI in orbit for the first time in August 2006, and the energy resolution was improved from ∼200 eV to ∼140 eV (@5.9 keV). The SCI has been a normal observation mode since October 2006. The details of the SCI are in Uchiyama et al. (2009).

Observing Condition

Since the Suzaku launch, the XIS has been functioning well. However, in November 2006, XIS 2 suddenly showed an anomaly. About 2/3 of the image was unusable due to a large amount of charge leakage. This event was possibly caused by a micro-meteoroid impact. Since this anomaly, XIS 2 has been dysfunctional. Furthermore, in June 2009, a part of XIS 0 suddenly showed an anomaly in Segment A. The history of these anomaly and the observing condition of the data in this thesis are summarized in figure 3.14.

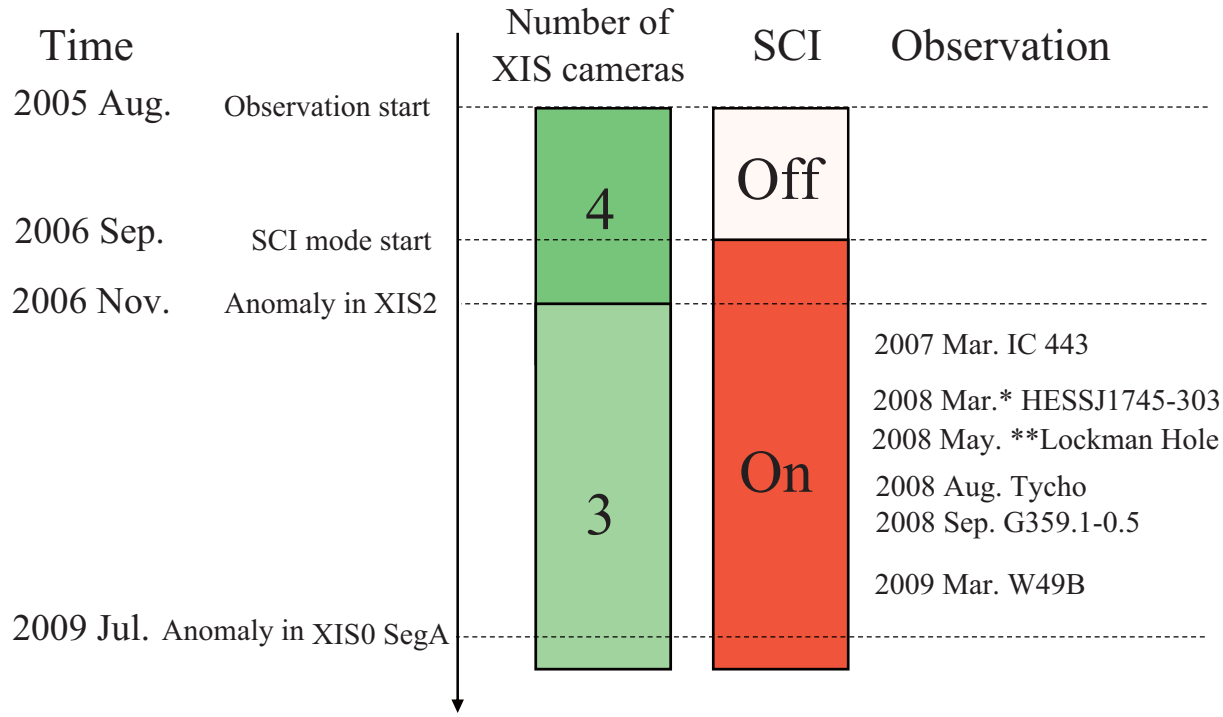

Fig. 3.14.—: History of the observing condition of the XIS. *Used as background data of G359.1-0.5. **Used as background data of Tycho.

Chapter 4

Thin Thermal Plasma

In this chapter, we classify the thin thermal plasma based on the ionization balance, and introduce ionizing, equilibrium, and recombining plasmas. Because these plasmas exhibit different spectra, we can classify and diagnose the plasma states from an observed X-ray spectrum. For example, electron and ionization temperatures, and volume emission measures are determined from the spectra in these states.

4.1 Classification

In a thin thermal plasma, we assume that the electron distribution is given by the Maxwell-Boltzmann distribution law

$$f(v) = 4\pi v^2 \Big(\frac{m}{2\pi k T_{\rm e}}\Big)^{3/2} \exp\Big(-\frac{mv^2}{2kT_{\rm e}}\Big), \tag{4.1}$$

where $f(v)$, k, m, and v are the velocity probability density, Boltzmann constant, mass and velocity of an electron, respectively. The key parameter is the electron temperature designated as $kT_{\rm e}$. We also designate the ionization temperature as kT_z, which determines the ion fractions (ionization degree of ions). With these definitions, the plasma can be classified into three cases as below.

1. $kT_z < kT_{\rm e}$: underionized
2. $kT_z = kT_{\rm e}$: ionization equilibrium
3. $kT_z > kT_{\rm e}$: overionized

These three cases are determined by the competition between ionization and recombination processes. The ionization processes are due to electron impact (collisional ionization), photo electric ionization, and autoionization. As the inverse of these processes, the recombination processes are due to 3-body recombination, radiative recombination, and dielectronic recombination.

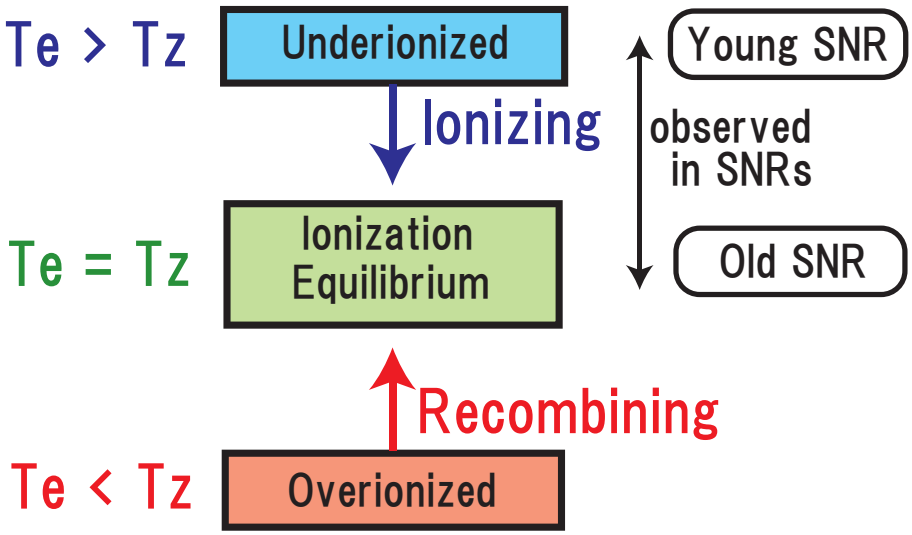

Fig. 4.1.—: Schematic view of plasma states. Note that almost all the observed thin thermal X-ray spectra of SNRs indicate underionized or ionization equilibrium states.

1) Underionized: Thermal energy of electrons exceeds the ionization energy. In the underionized case[1], ionization dominates recombination. We hence describe the plasma in this state "**ionizing plasma**". Ionizing plasma has been observed in almost all the young SNRs, such as Cassiopeia A, SN 1006, and Tycho.

2) Ionization equilibrium: This is the final state for a thermal plasma, in which the balance between the ionization and recombination rates is achieved. Because ionization is due to electron collisions in most cases, we describe the plasma in this state as "**collisional ionization equilibrium (CIE) plasma**". Such a CIE plasma has been observed in old SNRs.

3) Overionized: This is the opposite of case (1). Recombination dominates ionization. We designate the plasma in this state as "**recombining plasma**". No one has observed the recombining plasma in SNRs.

A schematic view of these plasma states is summarized in figure 4.1.

[1]We here only assume the case with no external factor, such as a strong X-ray irradiation source, electric or magnetic field, or rapid expansion or contraction of the plasma.

4.2 X-ray Emission

The appropriate plasma emission model depends not only on the temperature, but also on the density. Focusing on low density ($\sim 1/\mathrm{cm}^3$) and high temperature ($10^6 \sim 10^8$ K) plasma condition which is typical of SNRs, we assume some approximations below.

- Low density and collisionally ionized plasma (Coronal approximation).
  In this approximation, most ions are in the ground state.
- Electrons are Maxwellian distributed.
- External electric and magnetic field effects are ignored.

Figure 4.2 shows the predicted spectrum from a thin thermal plasma in CIE state with above assumptions. We can see complicated structures of many line and continuum emissions. In this section, we summarize these emission mechanisms.

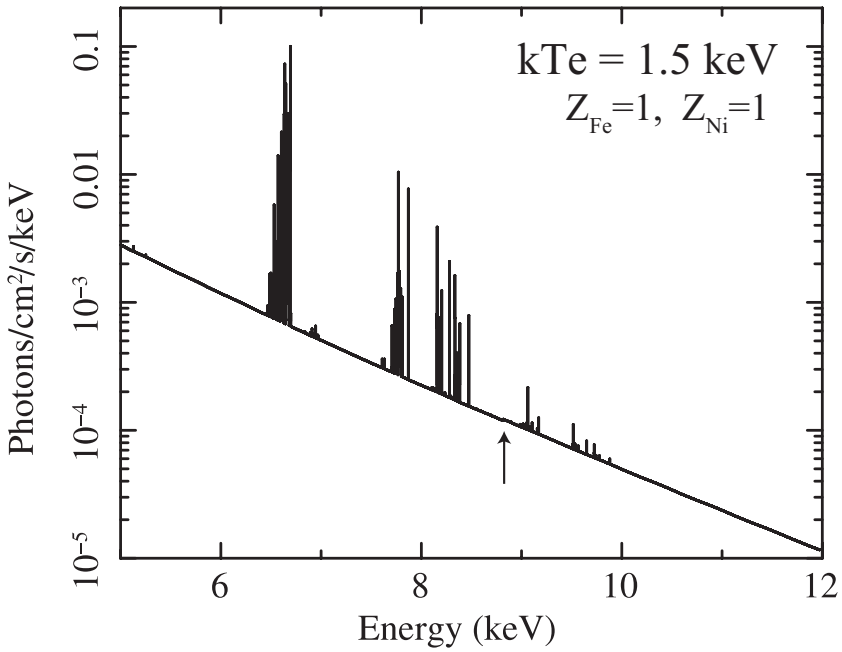

Fig. 4.2.—: Predicted thin thermal spectrum for electron temperature of 1.5 keV and abundances of solar values. We show the 5–12 keV band, where emission lines mainly originate from Fe. Most of the continuum emission is due to the bremsstrahlung radiation. A very small continuum jump at 8.83 keV (arrow) corresponds to the edge energy of a radiative recombination continuum of H-like Fe. This figure is derived from the APEC code assuming the CIE state.

4.2.1 Continua

There are three radiative processes for continuum emission; thermal bremsstrahlung, radiative recombination, and 2-photon radiation. These emissions are due to free-free, free-bound, and bound-bound transitions of electrons, respectively. The most intense continuum emission is the thermal bremsstrahlung in a CIE plasma of kT of the order of keV.

Free-free Emission: Bremsstrahlung

Electrons emit photons by the bremsstrahlung process in the Coulomb field made by ions. The emission power in an isotropic thermal distribution (thermal equilibrium) is described as

$$\frac{dW}{dV\,dt\,d\nu} = \frac{32\pi e^6}{3mc^3}\left(\frac{2\pi}{3km}\right)^{1/2} T_e^{-1/2} A^2 n_e n_i \mathrm{e}^{-h\nu/kT_e}\overline{g_{ff}} \tag{4.2}$$

$$= 6.8\times10^{-38} A^2 n_e n_i T_e^{-1/2} \mathrm{e}^{-h\nu/kT_e}\overline{g_{ff}} \quad [\mathrm{ergs\ s^{-1}\ cm^{-3}\ Hz^{-1}}], \tag{4.3}$$

where e, c, A, n_e, n_i, and $\overline{g_{ff}}$ are the electron charge, light speed, atomic number, electron and ion densities, and velocity averaged Gaunt factor.

Gaunt factor is a function of the electron energy and the emission frequency [2]. For a typical X-ray emitting thermal plasma,

$$\overline{g_{ff}} = \left(\frac{3}{\pi}\frac{kT_e}{h\nu}\right)^{1/2}. \tag{4.4}$$

As we see in the above formula, we can investigate electron and ion densities and electron temperature from the intensity and shape of the bremsstrahlung continuum spectrum. In figure 4.3a, we show one example of bremsstrahlung emission.

[2] This is reviewed in Bressaard & van de Hulst (1962), and Karzas and Latter (1961).

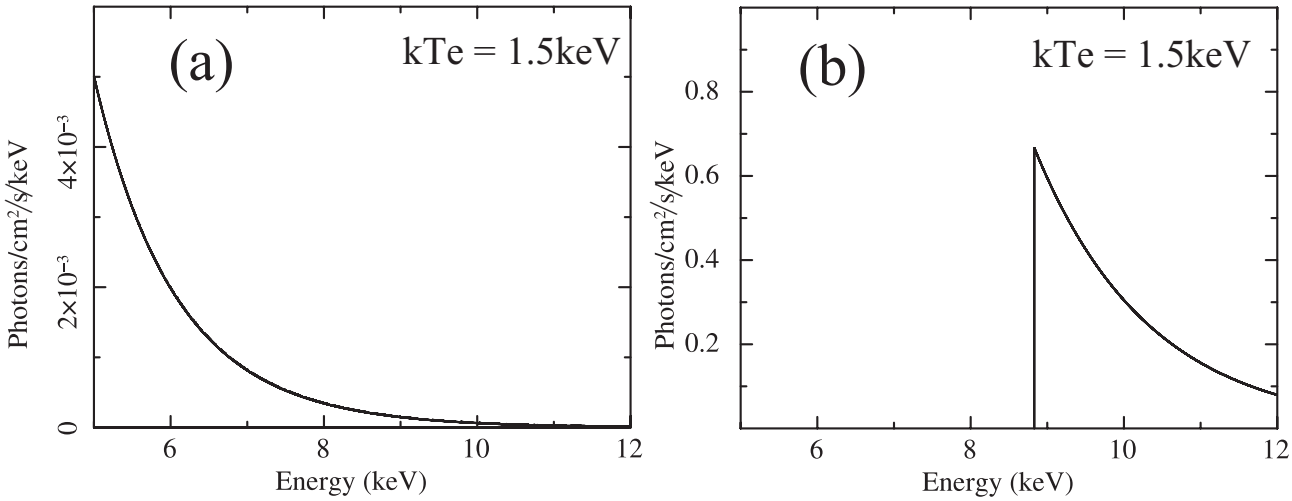

Fig. 4.3.—: Predicted continuum spectra in the 5–12 keV band for electron temperature of 1.5 keV. (a) Bremsstrahlung continuum due to free-free transitions of electrons. (b) Radiative recombination continuum due to free-bound transitions of electrons. We show the continuum structure made by H-like Fe ions.

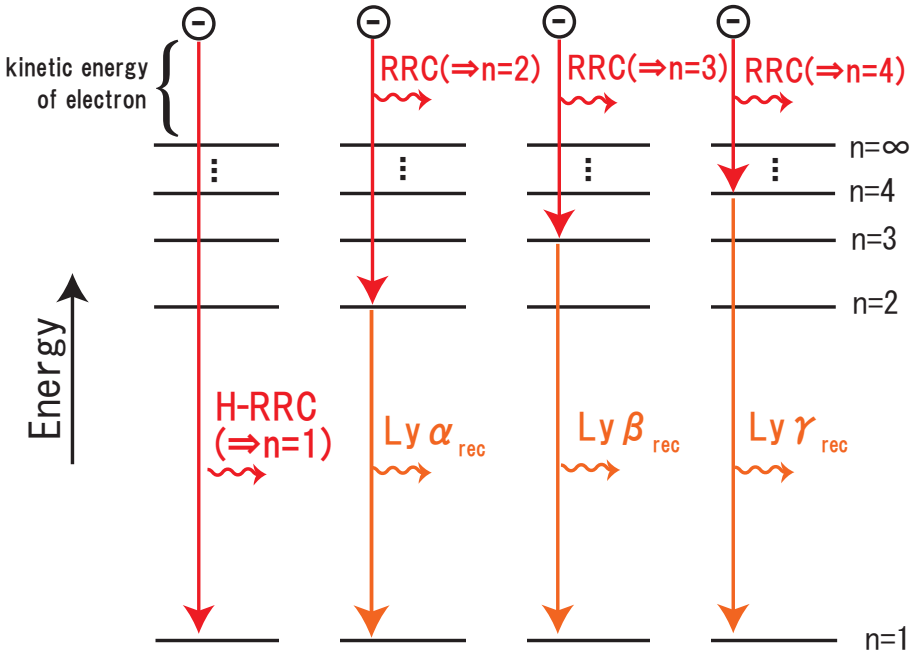

Fig. 4.4.—: Schematic illustration of emission mechanisms for radiative recombination continua and recombination lines.

Free-bound Emission: Radiative Recombination Continuum

When an electron recombines with an ion, a photon is emitted. The energy of this photon equals the kinetic energy of the electron plus the binding energy of the newly-recombined electron. Since the kinetic energy of the electron is not unique, this forms a continuous spectrum with a sharp edge at the binding energy of the levels. This emission is called a radiative recombination continuum (RRC). We show the schematic illustration of the RRC emission mechanism in figure 4.4.

The power emitted by this process is described in Tucker & Gould (1996) as:

$$\frac{dE}{dV\,dt\,d\omega} = \frac{dW}{dE} = n_{\rm e} n_{A,j+1} v E \cdot \sigma_n^{\rm rec}(E_{\rm e}) \cdot \frac{f(v)dv}{dE}, \tag{4.5}$$

where $n_{A,j+1}$, E, and $\sigma_n^{\rm rec}(E_{\rm e})$ are the density of the ion of the atomic number A and the ionization state $j+1$, the energy of the emitted photon, and the recombination cross section to the level n at the electron energy $E_{\rm e}$, respectively. In our assumption, $f(v)$ is the Maxwell-Boltzman distribution described in equation 4.1.

This equation can be simplified considerably if we define $E_{\rm edge}$ to be the electron binding energy[3]. Substituting $E_{\rm e} = mv^2/2$ and the Maxwell-Boltzmann equation for $f(v)$, we can rewrite equation 4.5 as below.

$$\frac{dW}{dE} = 4 n_{\rm e} n_{A,j+1} E\Big(\frac{E - E_{\rm edge}}{kT_{\rm e}}\Big)\sqrt{\frac{1}{2\pi m k T_{\rm e}}} \cdot \sigma_n^{\rm rec}(E - E_{\rm edge}) \cdot \exp\Big(-\frac{E - E_{\rm edge}}{kT_{\rm e}}\Big), \tag{4.6}$$

This equation completely describes the spectrum of the RRC[4].

We can approximate this formula when the electron temperature is much lower than the K-edge energy ($kT_{\rm e} \ll E_{\rm edge}$) as below:

$$\frac{dW}{dE} \propto \exp\left(-\frac{E - E_{\rm edge}}{kT_{\rm e}}\right), \quad \text{for } E \geq E_{\rm edge} \ . \tag{4.7}$$

Note that $dW/dE = 0$ for $E < E_{\rm edge}$. In the spectral analyses of the following chapters, we adopt this formula. In figure 4.3b, we show the RRC spectrum from H-like Fe ions assuming this equation.

In this thesis, we describe the RRC accompanied by the recombination of H-like ions to the ground state of He-like ions as "He-RRC". In the same way, we designate that of fully ionized ions to the ground state of H-like ions as "H-RRC". In table 4.1, we summarize the edge energies of He-RRC and H-RRC for major elements.

[3] $E_{\rm edge}$ corresponds to the spectral edge energy of the recombination continuum.
[4] More details are described in http://cxc.harvard.edu/atomdb/physics/plasma/plasma.html.

Table 4.1—: K-shell edge energies ($E_{\rm edge}$) of He-RRC and H-RRC. These values correspond to the K-shell binding potential of He-like and H-like ions, respectively.

A	Element	$E_{\rm edge}$ (keV)	
		He-RRC	H-RRC
12	Mg	1.763	1.958
14	Si	2.439	2.666
16	S	3.225	3.482
18	Ar	4.121	4.406
20	Ca	5.128	5.440
26	Fe	8.830	9.194

Bound-bound Emission: 2-Photon Decay

If the direct transition between two bound states is forbidden by a selection rule, two-photon process occurs. The simplified level scheme is shown in figure 4.5a. Because only the sum of the emitted two photons are conserved, the energy of each photon is not uniquely determined. For this reason, bound-bound transition associated with two photon radiation forms a continuous spectrum.

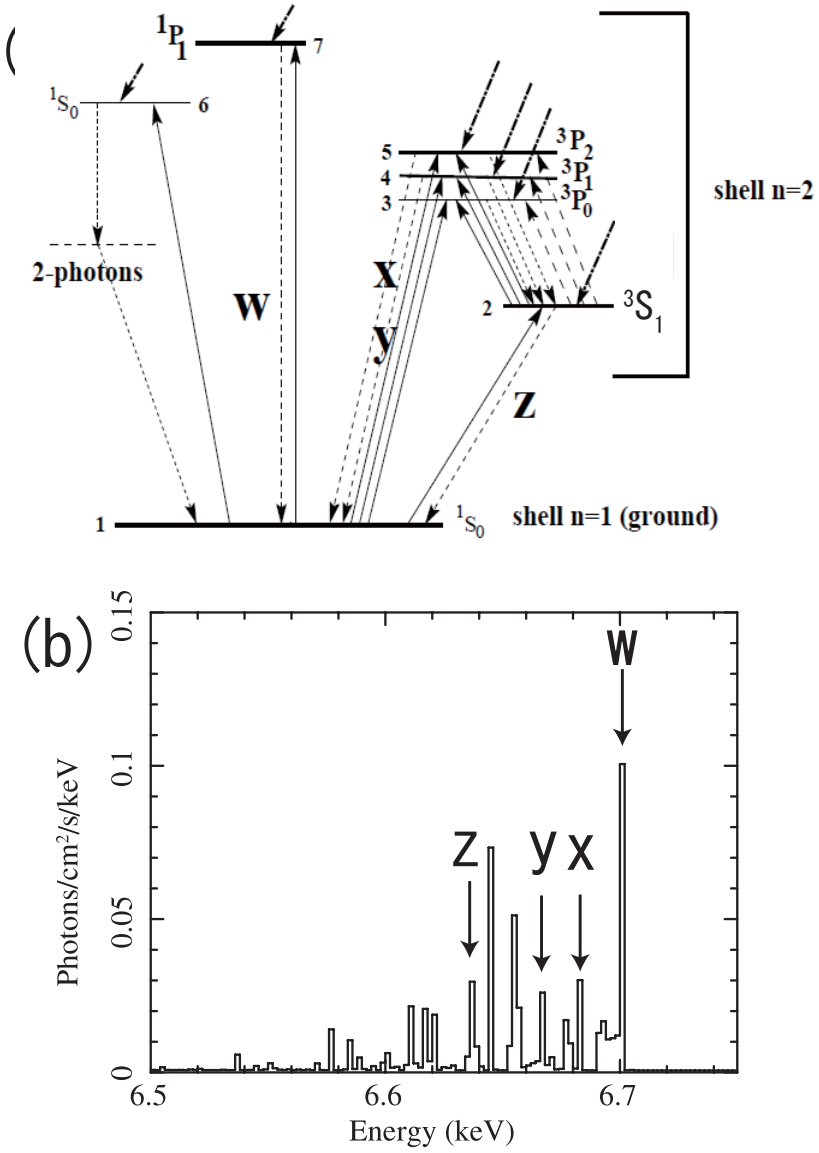

Fig. 4.5.—: (a) Simplified level scheme for He-like ions. w, x and y, and z represent resonance, inter-combination, and forbidden lines, respectively. Solid upward arrows indicate the collisional excitation transitions. Broken arrows are radiative transitions (including photo-excitation from $^3S_1$ to $^3P_{0,1,2}$ levels, and 2-photon continuum from $^1S_0$ to the ground level). Thick skew arrows are recombination (radiative and di-elecrtonic) plus cascade processes. This figure is taken from Porquet et al. (2001). (b) Prospective spectrum for the electron temperature of 1.5 keV in CIE. We show the energy band around the Kα energy of a He-like Fe ion. We can see the resonance (w), inter-combination (x and y), and forbidden (z) lines. Other lines mainly originate from the dielectronic recombination processes of He, Li, and Be-like Fe ions. This figure is derived from the APEC code.

4.2.2 Lines

The bound-bound transitions between two discrete quantum levels accompany photon emission called line emission. In the cases of a hydrogen atom or other H-like ion[5], a fairly complete discussion of transition rates can be given by quantum theory. For a hydrogen atom, the energy of a photon absorbed or emitted in a transition between two discrete levels (n and n') is given by

$$E = R_y \left(\frac{1}{n^2} - \frac{1}{n'^2} \right) , \tag{4.8}$$

where R_y is Rydberg constant (13.6 eV). For heavy elements, E roughly becomes

$$E \sim A^2 R_y \left(\frac{1}{n^2} - \frac{1}{n'^2} \right) . \tag{4.9}$$

The emission lines are referred to as Lyα (H-like Kα; $2p \rightarrow 1s$), Lyβ (H-like Kβ; $3p \rightarrow 1s$), Lyγ (H-like Kγ; $4p \rightarrow 1s$), and so on. Mean azimuthal (orbital angular momentum) quantum numbers (l) are 0 for s, and 1 for p. The line energies of Lyman series of major elements are listed in table 4.2.

The emission mechanisms for He-like ions[6] are summarized in figure 4.5. He-like ions emit three intense lines: resonance ($1s2p\ ^1\mathrm{P}_1 \rightarrow 1s^2\ ^1\mathrm{S}_0$), forbidden ($1s2s\ ^3\mathrm{S}_1 \rightarrow 1s^2\ ^1\mathrm{S}_0$), and inter-combination ($1s2p\ ^3\mathrm{P}_{2,1} \rightarrow 1s^2\ ^1\mathrm{S}_0$) transition lines. In this thesis, the sum of Kα lines is denoted by "Heα" ($n = 2 \rightarrow 1$), and He-like Kβ by "Heβ" ($3 \rightarrow 1$), He-like Kγ by "Heγ" ($4 \rightarrow 1$), and so on.

Table 4.2—: K-shell line energies of H-like and He-like ions.

	Lyα	Lyβ	Lyγ		Heα		Heβ	Heγ
				res.*	forb.*	int.*		
Mg	1472	1745	1840	1352	1330	1343	1579	1660
Si	2006	2377	2506	1865	1840	1854	2183	2294
S	2623	3107	3277	2461	2431	2447	2884	3033
Ar	3323	3936	4151	3140	3104	3124	3685	3875
Ca	4106	4864	5130	3908	3845	3892	4582	4819
Fe	6966	8266	8732	6702	6641	6670	7798	8217

*res., forb., and int. indicate resonance, forbidden, and inter-combination lines, respectively.

[5] An ion which contains only one electron is called a H-like ion.
[6] An ion which contains two electrons is called a He-like ion.

The ionization states of ions depend on the plasma temperature. Figure 4.6 shows the ion fractions of major elements in the CIE state as a function of temperature. When the plasma temperature becomes low, the fraction of low-ionized ions increases. For this reason, a weighted line center energy of emission lines becomes low. We show this effect in figure 4.7.

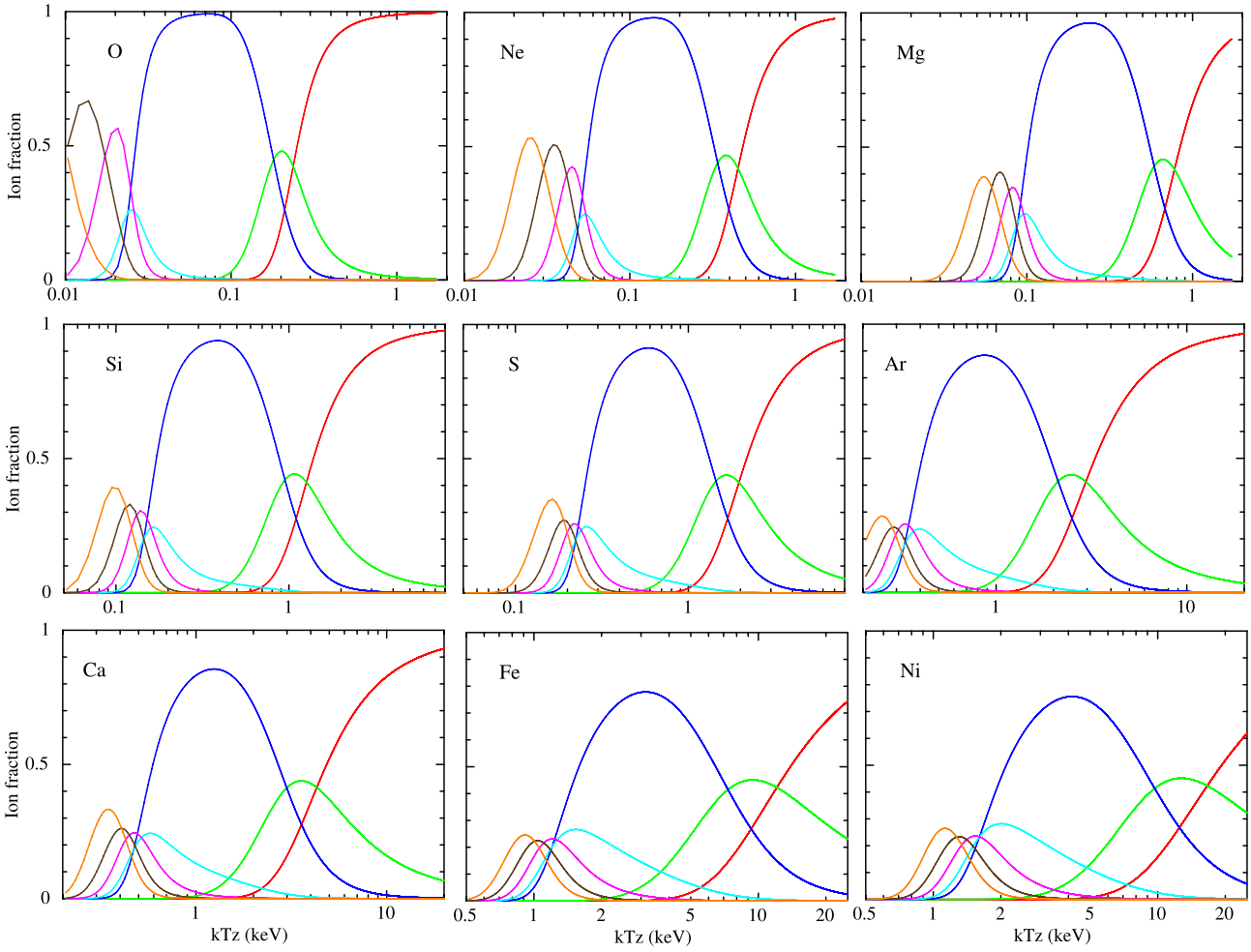

Fig. 4.6.—: Ion fractions of heavy elements as a function of plasma (ionization) temperature. Red, green, blue, aqua, purple, brown and orange colors represent fully-ionized, H-, He-, Li-, Be- B- and C-like ions, respectively.

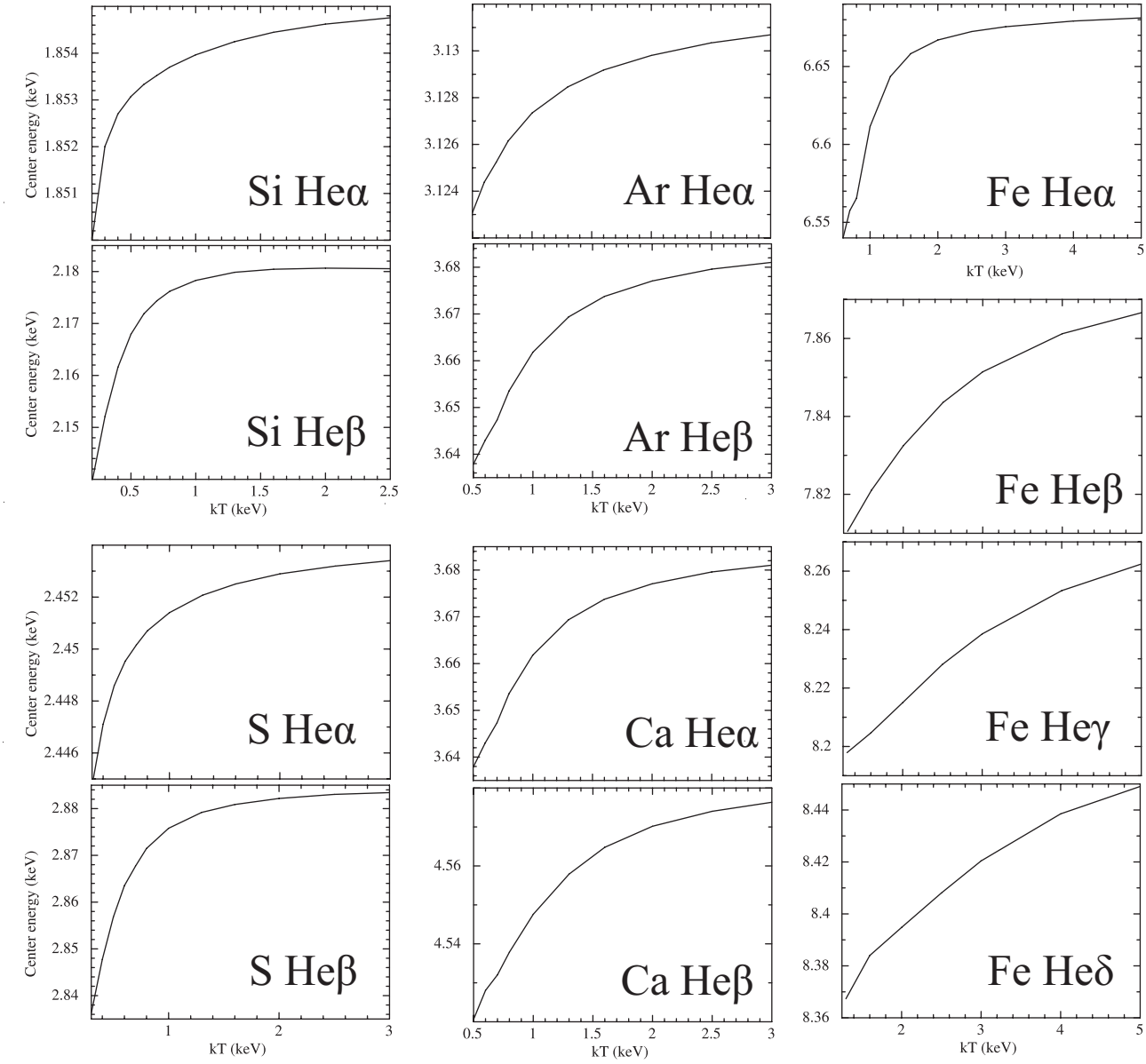

Fig. 4.7.—: Weighted line center energies for He-like and lower ionized ions as a function of plasma temperature. Plasma condition is assumed be in a CIE state. Low center energies at low temperatures are mainly due to dielectronic recombination processes. These figures are derived from the APEC code.

Here we mention the radiative processes of line emission. When an electron collides with an ion, it may excite the ion (**electron impact excitation**), or it may ionize the ion (**electron impact ionization**) flicking the bound electron at the inner-shell[7]. If an electron in an upper level decays to a lower bound state subsequently, a monochromatic photon is emitted.

Dielectronic Recombination is other important process. An electron recombines with an ion to an excited level and subsequently another electron is excited to a higher level. Thus the ion is left in a highly excited state, which may then autoionize or radiatively decay. In the latter case, one of the excited electrons decay to a lower level, creates a satellite line at a slightly lower energy than the normal transition. "Satellite" is named for the energy in the vicinity of the main transition line, because another electron is still at the upper level.

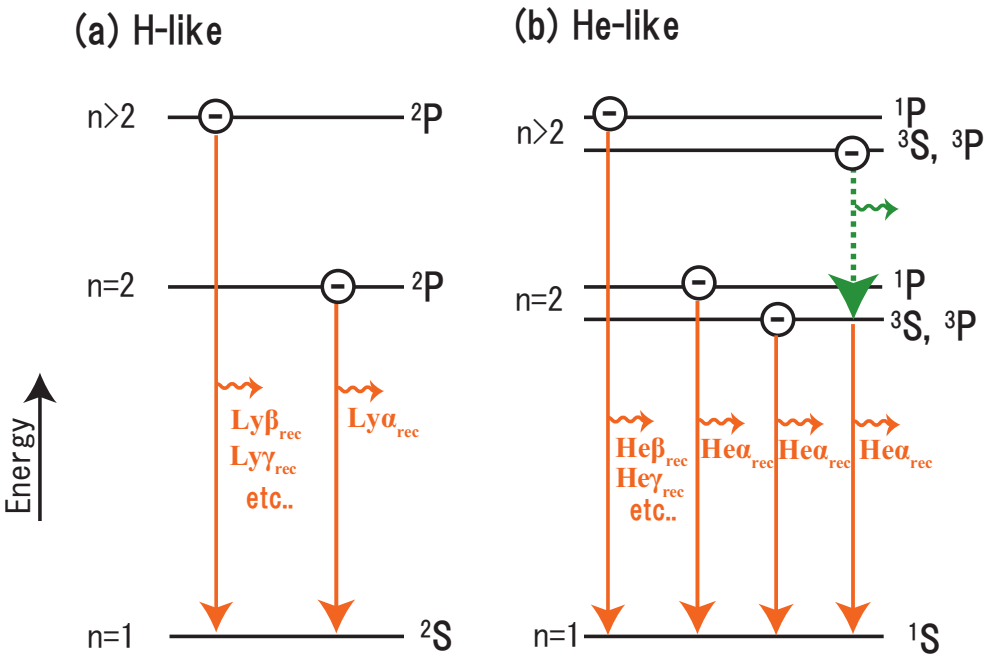

Fig. 4.8.—: Schematic illustrations of emission mechanisms for cascade lines. (a) Simplified level scheme for H-like ions. Most free-bound electrons captured into excited levels are straightforwardly transit to the ground state and produce radiate recombination (cascade) lines. (b) Same for He-like ions. Most electrons captured into excited "singlet" levels are straightforwardly transit to the ground state. On the contrary, most electrons into "triplet" levels are once transit to triplet levels of $n = 2$ (dotted arrow), and then transit to the ground state because of the selection rules for radiative transitions.

[7]It is called the inner-shell ionization.

Cascade Decay is an important process in recombination-dominant plasmas. Cascade decay is accompanied by the recombination of electrons into higher excited levels in the free–bound transitions. Figure 4.8 shows schematic illustrations of cascade line emission mechanisms for H-like (figure 4.8a) and He-like (figure 4.8b) ions. Throughout this thesis, we designate the cascade lines of H-like ions as Ly$\alpha_{\rm rec}$ ($n = 2\rightarrow1$), Ly$\beta_{\rm rec}$ ($3\rightarrow1$), Ly$\gamma_{\rm rec}$ ($4\rightarrow1$), and so on. We also designate the cascade lines of He-like ions as He$\alpha_{\rm rec}$ ($n = 2\rightarrow1$), He$\beta_{\rm rec}$ ($3\rightarrow1$), He$\gamma_{\rm rec}$ ($4\rightarrow1$), and so on.

In the case of H-like ions, most electrons captured into upper levels are straightforwardly decay to the ground state. In the case of He-like ions, the transition processes are very complicated. In the first-order approximation, however, most electrons captured into upper "singlet" levels are straightforwardly decay to the ground state. On the other hand, most electrons captured into "triplet" levels transit via triplet levels of $n = 2$ to the ground state. This is because of the selection rules for radiative transitions.

In recombination-dominant plasmas, as we can expect from figure 4.8b, these cascade processes increase the intensity ratio of the forbidden and inter-combination lines to the resonance line compared to the ratio in collisional-dominant plasmas. Hence, the Heα line center of a recombination-dominant plasma is significantly lower than that of the collisional-dominant case. In fact, the experimental weighted line center for Fe Heα in the recombination-dominant condition is 6.666 ($\pm$0.005) keV (Wargelin et al. 2005) [8]. On the other hand, the predicted weighted center for Fe Heα in collisional-dominant plasma at sufficiently high temperatures ($kT >$4 keV) is 6.685 keV (figrue 4.7). There is a $\sim$20 eV line center difference between collisional-dominant and recombination-dominant plasmas. This difference ($\sim$20 eV) is significantly larger than the calibration uncertainty of the Suzaku XIS at $\sim$6 keV ($\sim$12 eV; Ozawa et al. 2009b). Thus, we can in principle derive the difference with very good conditions [9] of high statics in the nearly CIE state plasma [10].

[8] Strictly speaking, this is the result of the charge exchange process. In this process, a H-like Fe ion rip an electron from the neutral atom or molecular. In perspective of the recombination-dominant condition, however, the essential mechanisms are the same.

[9] This method is applied to the Galactic center diffuse X-rays (Koyama et al. 2007b). Because the observed line center of Fe Heα is 6.680 ($\pm$0.001) keV, they concluded the X-ray emission mainly originate from the excitation of electrons.

[10] Note that the weighted line center energy also becomes low in the underionized case because there are many low-ionized ions.

In figure 4.9, we illustrate the expected spectrum for a recombination-dominant plasma. We ignore the dielectronic recombination lines here. The recombination structures are composed of RRC into each principle number (n), and cascade lines below the K-edge energy of the RRC ($E_{\rm edge}$).

The emission flux of the RRC is most intense in the case of RRC[→1] [11]. We can confirm this from the approximated recombination cross section for H-like ions into a level of n (Nakayama & Masai 2001).

$$\sigma_n \propto \frac{1}{n^3}\left(\frac{3}{2}\frac{kT_{\rm e}}{E_{\rm edge}}+\frac{1}{n^2}\right)^{-1} \tag{4.10}$$

Note that in the case of He-like ions, this formula is still a good approximation but σ_1 should be reduced by half because one electron exists already in the ground state. Using this equation, we can estimate the flux ratios between RRC[→>1] [12] and RRC[→1]. For example, in the case of Si H-RRC at $kT_{\rm e}$ = 0.5 keV, the flux ratio of RRC[→2]/RRC[→1] is derived from σ_2/σ_1 as ∼0.29. In the same way, the ratio RRC[→3]/RRC[→1] is derived from σ_3/σ_1 as ∼0.12. In the following analysis chapters, we mention only the most intense RRC[→1].

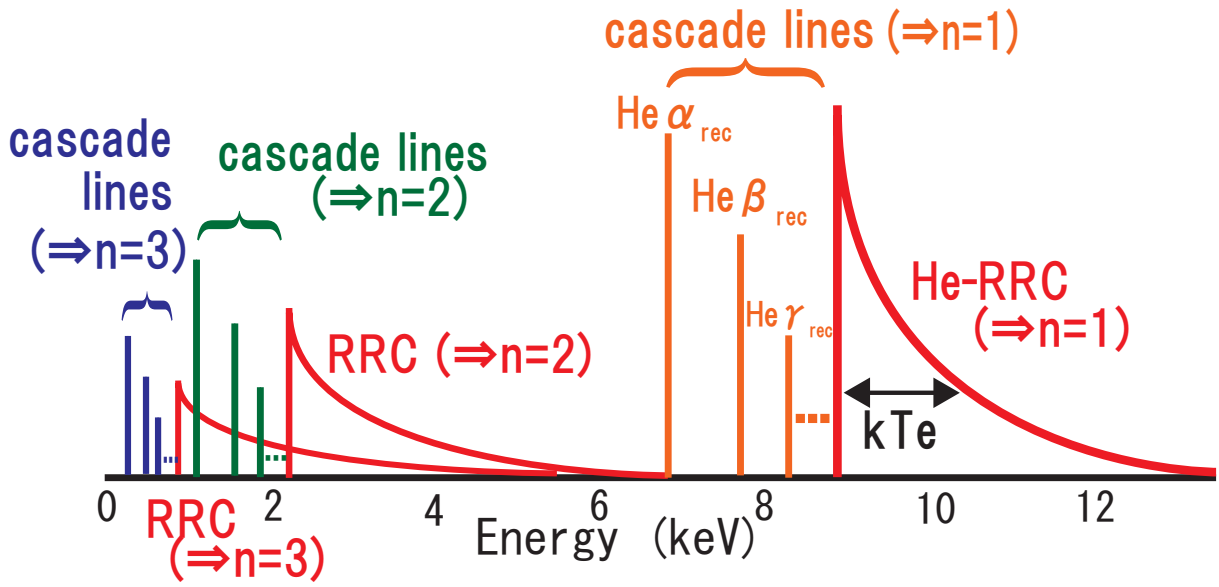

Fig. 4.9.—: Spectrum expected for a recombination-dominant plasma. We show the structures accompanied by the electron recombination with H-like Fe ions to He-like Fe ions. Here we ignore the dielectronic recombination lines. In our spectral analysis in the W49B chapter (in the energy band of 5–12 keV), major recombination structures are due to the transition of electrons into the ground state (n = 1).

[11] This notation means the RRC into the ground state.
[12] This means the RRC into n >1.

4.3 Temperature Measurement

We can derive the electron and ionization temperatures from an observed X-ray spectrum in several independent methods. We explain how to obtain these temperatures.

4.3.1 Electron Temperature (kT_e)

The electron temperature is measured by three independent methods. As we see from equation 4.2, the **Bremsstrahlung Continuum Shape** is a simple function of kT_e, hence kT_e is determined. This has been almost only way to determine kT_e before the Suzaku era.

In addition to this method, we have developed two independent methods. One way is to use the **Line Flux Ratios**. The probability ratio of collisional excitation between $n = 1 \rightarrow 2$ and $n = 1 \rightarrow 3$ only depends on the energy of a colliding electron (i.e. electron temperature). If collisional excitation is a major process in the plasma, which is true for most SNRs, the Kβ/Kα flux ratio directly reflects the transition probability ratio. In the extreme recombining plasma, there is cascade decay contribution for line emission in some measure. However, this contribution is negligible for most cases [13]. In figure 4.10, we show the flux ratios of Heβ/Heα (a) and Lyβ/Lyα (b) of Si, S, Ar, Ca, Fe in the CIE state. We also show Heγ/Heα and Heδ/Heα of Fe (a). All of the ratios are monotonically increasing functions of the plasma temperature.

The other way is to use the **Width of Recombination Continuum**. From equation 4.7, we see that kT_e reflect the continuum shape. Thus, we can derive kT_e from the width of the RRC.

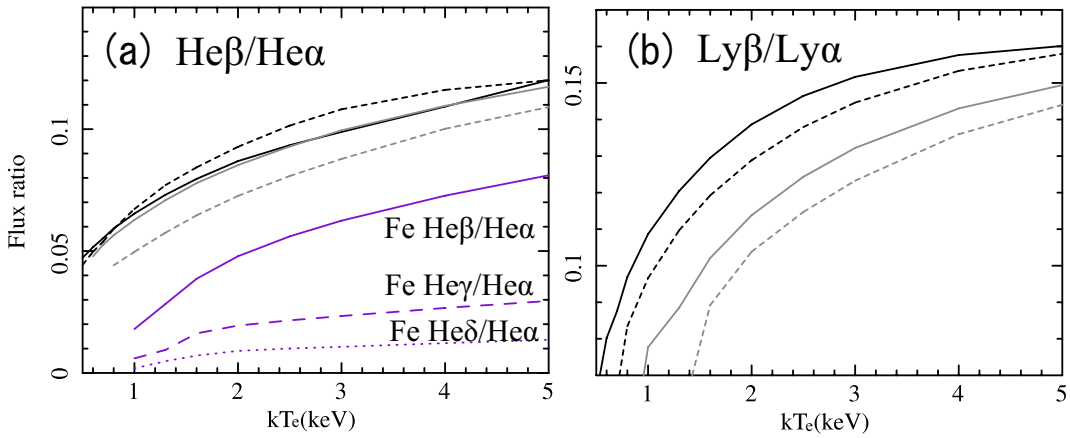

Fig. 4.10.—: (a) Predicted emissivity ratios of Heβ/Heα for Si (black solid), S (black dashed), Ar (gray solid), and Ca (gray dashed) as a function of plasma temperature. We also show ratios of Heβ/Heα (solid), Heγ/Heα (dashed) and Heδ/Heα (dotted) of Fe. (b) Predicted emissivity ratios of Lyβ/Lyα as a function of plasma temperature. The meanings of colors and lines are same as (a). These figures are derived from the APEC code, assuming the CIE state.

[13] Note in the photoionized plasma, the contribution becomes dominant.

4.3.2 Ionization Temperature (kT_z)

The ionization temperature directly reflects the ion fractions by definition. Hence, we can derive the ionization temperature using the flux ratios of ions in different ionization states.

The most direct method is to use the **Line Flux Ratios**. One example is Lyα/Heα. In figure 4.11, we show flux ratios of Lyα/Heα in the (a) CIE, (b) overionized, and (c) underionized cases. All cases exhibit monotonically increasing functions of the plasma temperature.

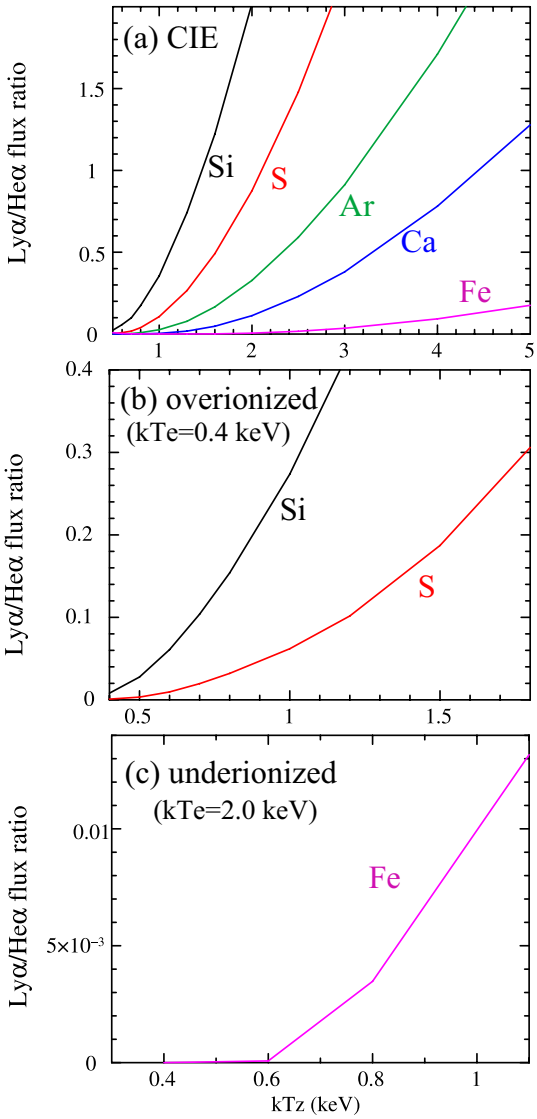

Fig. 4.11.—: Predicted emissivity ratios of Lyα/Heα for several elements as a function of ionization temperature. (a) Ratios for the CIE state. (b) Same for the overionized state at $kT_e = 0.4$ keV (c) Same for the underionized state at $kT_e = 2$ keV. These figures are derived from the plasma code of APEC (a) and Masai (b and c).

The other new method we have developed is to **use the fluxes of He-RRC and H-RRC**. Since the fluxes of He-RRC and H-RRC directly reflect the amount of H-like and fully ionized atoms, respectively, their flux ratio or to Heα is sensitive to the ionization temperature. In figure 4.12, we show some examples of (a) He-RRC/Heα, (b) H-RRC/He-RRC, and (c) H-RRC/Heα for several $kT_{\rm e}$ cases. All ratios are monotonically increasing functions of kT_z, and hence these ratios can be used to derive kT_z.

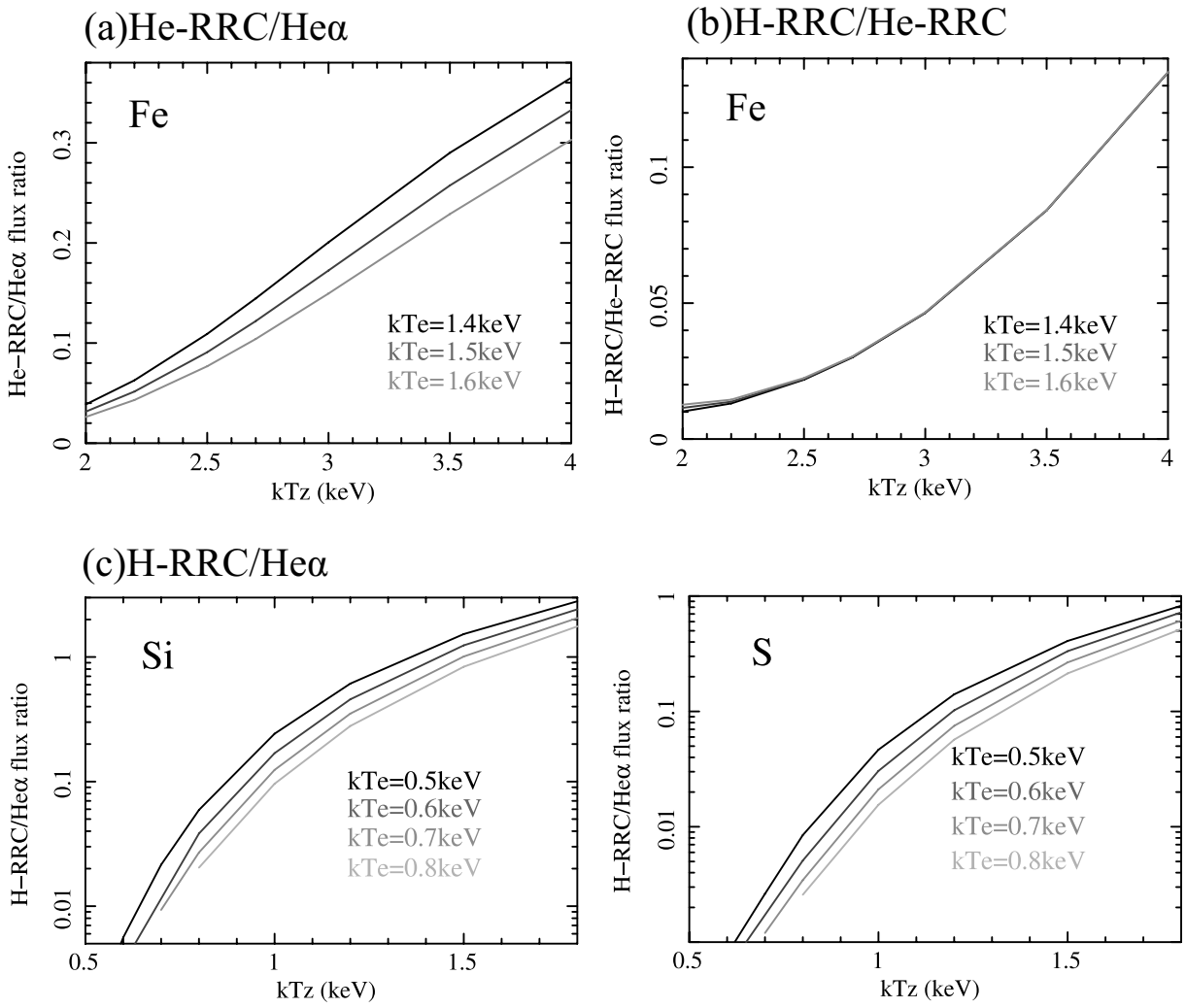

Fig. 4.12.—: Predicted emissivity ratios using the RRC as a function of ionization temperature for several electron temperatures. (a) He-RRC/Heα of Fe. (b) H-RRC/He-RRC of Fe. (c) H-RRC/Heα of Si (left) and S (right). These figures are derived from the plasma radiation code of Masai (1994).

4.4 Volume Emission Measure Measurement

A volume emission measure (VEM) is one of the physical parameters. It is given by

$$\mathrm{VEM} \equiv \frac{\int n_e n_{\mathrm{H}} dV}{4\pi D^2}, \tag{4.11}$$

where n_e, n_{H}, V, and D are the electron and hydrogen densities (cm^{-3}), emitting volume (cm^3), and distance to the source (cm), respectively. A VEM is proportional to the observed flux and used to estimate the total amount of the plasma. In the following chapters of SNR analyses, we derive VEMs from the emission of electrons' bremsstrahlung and recombination components. In this section, we summarize how to derive VEMs of these components from an observed X-ray spectrum.

4.4.1 Bremsstrahlung Component

The continuum spectrum of bremsstrahlung is given in equation 4.2. We obtain the VEM from the normalization parameter of the fitting model which reproduce the observed spectrum. For the VAPEC model which we use in our analyses[14], the normalization is given in unit of $10^{-14} \int n_e n_{\mathrm{H}}\ dV/(4\pi D^2)$, and hence it is directly converted to the VEM.

Table 4.3—: Solar number densities of major elements normalized by hydrogen (Anders & Grevesse 1989).

A	Element	$n_{\mathrm{X}}/n_{\mathrm{H}}\vert_{\mathrm{solar}}$
1	H	$1.00\times10^{+0}$
2	He	9.77×10^{-2}
6	C	3.63×10^{-4}
7	N	1.12×10^{-4}
8	O	8.51×10^{-4}
10	Ne	1.23×10^{-4}
12	Mg	3.80×10^{-5}
14	Si	3.55×10^{-5}
16	S	1.62×10^{-5}
18	Ar	3.63×10^{-6}
20	Ca	2.29×10^{-6}
24	Cr	4.68×10^{-7}
25	Mn	2.45×10^{-7}
26	Fe	4.68×10^{-5}
28	Ni	1.78×10^{-6}

[14]This is a thin thermal plasma model in the CIE state (Smith et al. 2001).

4.4.2 Recombination Component

We here explain how to derive the VEM from the H-RRC of an element X. Note that the procedure is essentially the same for the He-RRC.

The flux of RRC ($F_{\rm RRC}$) accompanied by the capture of electrons into the ground state of H-like X is given as,

$$F_{\rm RRC} = \alpha_1(kT_{\rm e}) \cdot Y_{\rm X} \cdot {\rm VEM}_{\rm RRC}, \tag{4.12}$$

where $\alpha_1(kT_{\rm e})$, $Y_{\rm X}$, and ${\rm VEM}_{\rm RRC}$ are a recombination rate coefficient into the ground state of H-like X at electron temperature $kT_{\rm e}$ (cm^3 s^{-1}), a particle number of H-like X, and a VEM for the recombination component (cm^{-5}).

The value $\alpha_1(kT_{\rm e})$ is given by

$$\alpha_1(kT_{\rm e}) = \alpha(kT_{\rm e}) \cdot \frac{\sigma_1}{(\sigma_1 + \sigma_2 + \sigma_3 + ...)}, \tag{4.13}$$

where $\alpha(kT_{\rm e})$ is the total K-shell recombination rate coefficient (cm^3 s^{-1}). σ_n (cm^2) means transition cross section to the excited level n. For $\alpha(kT_{\rm e})$, we use the results of Badnell (2006), who calculated the collisional-radiative population equations. The value $\sigma_1/(\sigma_1 + \sigma_2 + \sigma_3 + ...)$ can be derived from equation 4.10.

The value $Y_{\rm X}$ is given by

$$Y_{\rm X} = Z_{\rm X} \cdot \frac{n_{\rm X}}{n_{\rm H}}\Big|_{\rm solar} \cdot \kappa(kT_z), \tag{4.14}$$

where $Z_{\rm X}$, $n_{\rm X}/n_{\rm H}|_{\rm solar}$, and $\kappa(kT_z)$ are an abundance of X in unit of the solar value, number density ratios between X and hydrogen in the solar photosphere, and an ion fraction of fully ionized X at ionization temperature kT_z. In Anders & Grevesse (1989), number densities ($n_{\rm X}$) of major elements are listed up. In table 4.3, we summarize these values. We should note that $Z_{\rm X}$ is the abundance for the "recombining" component. Since we have no available radiative code for the recombining plasma, we substitute $Z_{\rm X}$ for the abundance of the "bremsstrahlung" (APEC) component, unless otherwise mentioned. From equations 4.12, 4.13 and 4.14 , we can derive ${\rm VEM}_{\rm RRC}$.

Chapter 5

W49B

W49B is one of the X-ray brightest Galactic SNRs. Using ASCA data, Kawasaki et al. (2005) claimed that the plasma of W49B is overionized. Hence, this is one of the best candidates of recombining plasma in SNRs. In fact, we can see strong Lyα lines of Si, S, Ar, and Ca in the ASCA [1] spectrum, which are the indicators of highly ionized plasma. The spectrum of W49B is notable for a very strong Kα line of Fe. This SNR has a jet-like X-ray morphology, which is unusual for SNRs, and an incomplete shell-like structure in the radio band. In this chapter, we summarize the results of a Suzaku observation of W49B and discuss the state of the plasma.

5.1 Previous Results

W49B (G43.3−0.2) exhibits centrally filled X-rays inside a bright radio shell with a radius of 100 arcsec (Pye et al. 1984). The distance to W49B remains uncertain. It was estimated to lie at a distance of ∼8 kpc (Radhakrishnan et al. 1972; Moffett & Reynolds 1994). Using the spectral distribution of H I absorption, however, Brogan & Troland (2001) found no clear evidence that W49B is closer than W49A, which is located at a distance of ∼11.4 kpc (Gwinn et al. 1992). This may indicate a possible association of W49B with the star-forming region W49A (see figure 5.1). The near-infrared narrowband images indicate a barrel-shaped structure with coaxial rings, which is suggestive of bipolar wind structures surrounding massive stars (Keohane et al. 2007; figure 5.2). They also showed an X-ray image from Chandra, which has a jet-like structure along the axis of the barrel. They interpreted these findings as evidence that W49B had exploded inside a wind-blown bubble in a dense molecular cloud.

Using ASCA data, Hwang et al. (2000) showed that broadband modeling of the remnant's spectrum required two thermal components (0.2 keV and 2 keV) and significant overabundances of Si, S, Ar, Ca, Fe, and Ni. They confirmed that most of the X-ray emitting plasma was nearly in collisional ionization equilibrium (CIE). They also found evidence for Cr and Mn Kα emission.

Kawasaki et al. (2005) claimed the presence of "overionized" plasma in W49B through the analysis of ASCA 2.75–6.0 keV spectrum. They measured intensity ratios of the H-like Kα (Lyα)

[1] ASCA is the previous Japanese X-ray satellite.

to He-like Kα (Heα) lines of Ar and Ca to obtain the ionization temperature (kT_z), and found that kT_z ($\sim$2.5 keV) is significantly higher than the electron temperature ($kT_{\rm e}$) determined from the bremsstrahlung continuum shape ($\sim$1.8 keV). Miceli et al. (2006) adopted the same analysis procedure for the XMM-Newton spectrum of the central region but found no evidence for the overionized state.

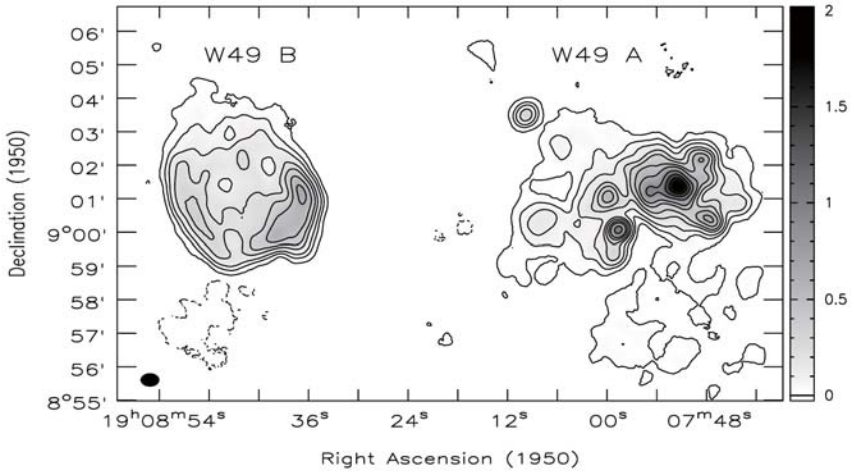

Fig. 5.1.—: 21 cm continuum image of the W49 complex with the H II region W49A to the west and the SNR W49B to the east. (Brogan & Troland 2001).

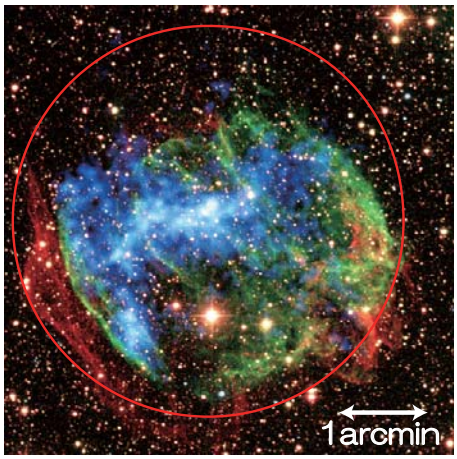

Fig. 5.2.—: Multiwavelength view of W49B (Keohane et al. 2007). (White) K_s band (2.2 μm). (Red) Infrared (2.12 μm) H_2 by Palomar. (Green) Infrared (1.64 μm) [Fe II] by Palomar. (Blue) X-ray by Chandra. We can see a barrel-shaped nebula consisting of bright infrared rings around a glowing bar of intense X-ray radiation along the axis. Red circle is a source region in our analysis.

5.2 Suzaku Observation

Table 5.1—: Observation log of W49B.

Start Date	Obs.ID	R. A.	Dec.	Exposure
		(J2000.0)		(ks)
2009-03-29	503084010	$19^{h}11^{m}08^{s}$	$09°06'57''$	52.2
2009-03-31	504035010	$19^{h}11^{m}08^{s}$	$09°06'55''$	61.4

We observed W49B twice with Suzaku. The observation log is given in table 5.1. Because the pointing positions and rotation angles do not differ significantly, we merged these two data sets. Three of the XISs were operated in the normal full-frame clocking mode with a SCI technique during our observations. Two are FI CCDs and the other is a BI CCD. Data were cleaned using processing version 2.2.11.24. We used HEASOFT version 6.5.1 for data reduction and XSPEC version 11.3.2 for spectral analysis. After screening with the standard criteria, [2] the net integration time was ∼113 ks.

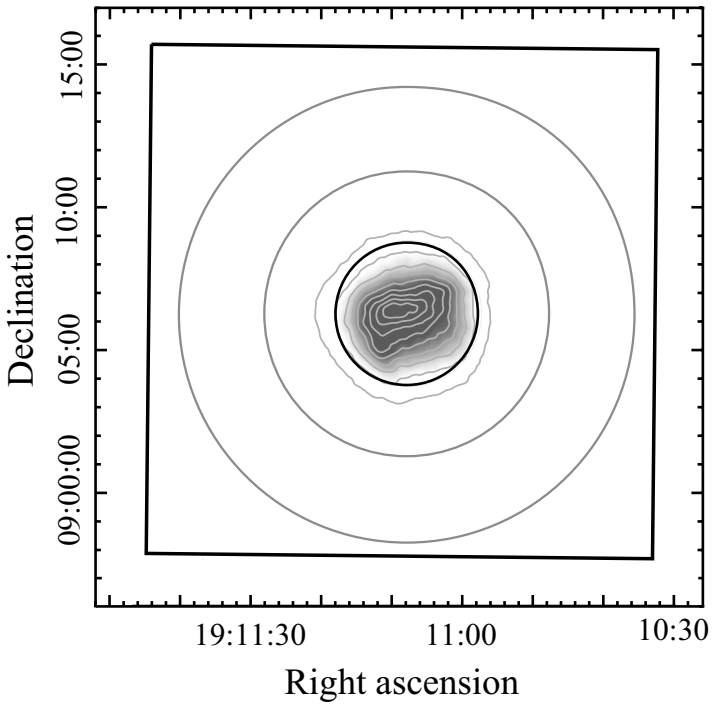

Fig. 5.3.—: Vignetting-corrected XIS image of W49B in the 1.5–7 keV band shown on a linear intensity scale. Data from the three active XISs are combined. Gray contours indicate every 10% intensity level relative to the peak surface brightness. The black circle and gray annulus indicate the source and background regions, respectively. The XIS field of view is shown by the black square. (Ozawa et al. 2009a)

[2] http://heasarc.nasa.gov/docs/suzaku/processing/criteria_xis.html

5.3 Results for Global Region

5.3.1 Overall Structure

Figure 5.3 shows the vignetting-corrected XIS image in 1.5–7 keV, the energy band including the major lines of K-shell emissions from Si, S, Ar, Ca, and Fe. We extracted the source spectrum from a circular region with a radius of 2.5 arcmin and the background spectrum from an annulus surrounding the source with inner and outer radii of 5 and 8 arcmin, respectively. The source spectrum was made by subtracting the background spectrum. The spectra of the two FI sensors were merged to improve the statistics because their response functions were almost identical. Figure 5.4 shows the merged FI spectrum. We can see several prominent lines of K-shell emission from He- and H-like ions.

5.3.2 Spectral Analysis

As shown in figure 5.4, the wide-band spectrum includes too many emission lines and possibly other complicated structures. For clean analyses and discussion, we focus on the 5–12 keV energy band, where emission lines and other structures mainly originate from Fe. We used only the FI data because the non-X-ray background (NXB) count rate of the BI data is much larger than the source rate in this energy band (see figure 3.9). We fixed the interstellar extinction to a hydrogen column density of 5×10^{22} cm^{-2} with the solar elemental abundances, following Hwang et al. (2000). To fine tune the energy scale, an offset was added as a free parameter and found to be –4.7 eV, which was within the allowable range of the calibration uncertainties. We added this offset for further spectral fitting.

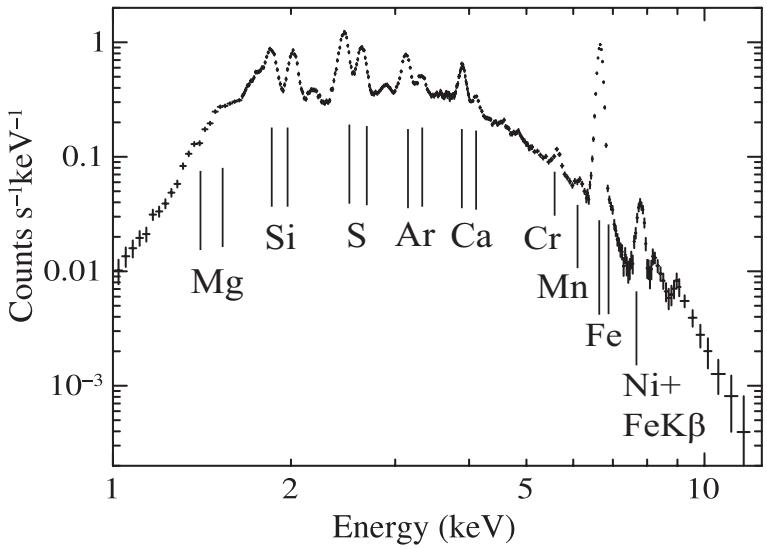

Fig. 5.4.—: Background-subtracted XIS FI spectrum. The energies of the prominent emission lines from specific elements are labeled. (Ozawa et al. 2009a)

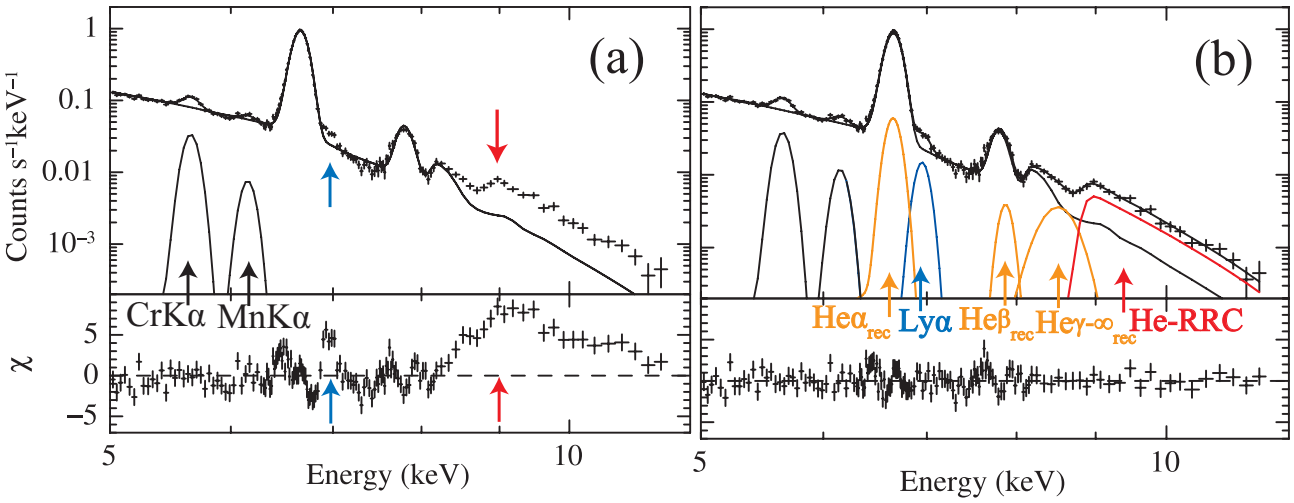

Fig. 5.5.—: (a) XIS FI spectrum in the 5–12 keV band. The best-fit VAPEC model and additional Kα lines of Cr and Mn (black arrows) with Gaussian functions are shown by solid lines. The lower panel shows the residual from the best-fit model. We can see large bumps at $\sim$7 keV (blue arrows) and around $\sim$9 keV (red arrows). (b) Same spectrum as (a), but with the radiative recombination continuum (red), recombination lines (orange), and a Lyα line (blue) of Fe. (Ozawa et al. 2009a)

CIE Model Fitting

We first fitted the spectrum with a VAPEC (CIE plasma) model (Smith et al. 2001). The Fe and Ni abundances (hereafter $Z_{\rm Fe}$ and $Z_{\rm Ni}$) normalized by the number fraction of the solar photosphere (Anders & Grevesse 1989) were free parameters. Since the Cr and Mn Kα emission lines are not included in the VAPEC model, we added these lines with Gaussian functions.

Figure 5.5a shows the fitting result of the one-VAPEC model, with a temperature of 1.64 keV. The model exhibited significant excess around the Fe Lyα line and above 8 keV, and hence was rejected with a large χ^2/degree of freedom (dof) of 1051/138.

We then tried a two-VAPEC model, assuming equal abundances between the two components. Fe Lyα was successfully reproduced, but the temperature of one component was unreasonably high ($\sim$70 keV), and a large residual above 8 keV remained with an unacceptable χ^2/dof of 562/136. Adding a further plasma or power-law component did not improve the fitting any more. In every case, the large bump above 8 keV was present.

To examine whether this bump is real or artificial, we checked the light curves of the source and background regions in the 8.5–10 keV band. They showed almost constant fluxes, indicating no flare-like event had occurred during the observations. In addition, we detected the bump in both FI spectra (XIS 0 and XIS 3) and even in the BI spectrum. Thus, the bump is a real structure.

Recombination Structures

The edge energy of the bump (∼9 keV) corresponds to the electron binding energy of Fe. This suggests that the saw-edged bump is likely due to a radiative recombination continuum (RRC). Both the line-like excess around Fe Lyα and this bump are suggestive of the overionized state because there should be a greater fraction of H-like ions in the overionized state than in the CIE. This excessive number of H-like ions causes strong He-RRC and Fe Lyα emissions. However, no current plasma code can be applied to the overionized plasma. We, therefore, introduce the Fe Lyα line and recombination structures consisting of the RRC and several emission lines below the K-edge energy of the RRC ($E_{\rm edge}$), in addition to the one-VAPEC model. We consider both He-RRC and H-RRC[3] for a consistency check.

We assume that the RRC is expressed as equation 4.7. This formula gives a good approximation when the electron temperature is much lower than the K-edge energy ($kT_{\rm e} \ll E_{\rm edge}$). In the case of W49B, $kT_{\rm e}$ is ∼1.5 keV, as we confirm later, while $E_{\rm edge}$ of Fe is ∼9 keV. Thus, we can safely adopt this formula.

For the recombination lines which originate from cascade decays of free-bound electrons, we consider He$\alpha_{\rm rec}$ ($n = 2 \rightarrow 1$), He$\beta_{\rm rec}$ ($3 \rightarrow 1$), and Heγ-$\infty_{\rm rec}$ ($n \geq 4 \rightarrow 1$; we combine them into one broad Gaussian function) [4]. The line widths and center energies of He$\alpha_{\rm rec}$ and He$\beta_{\rm rec}$ are fixed at zero and the experimental values for a charge exchange process, respectively (Wargelin et al. 2005). Those of Heγ-$\infty_{\rm rec}$ are allowed to vary freely. The fluxes of all these lines are free parameters.

The resultant best-fit parameters and models are given in table 5.2 and figure 5.5b, respectively. With this model, χ^2/dof is greatly improved to 193/128, although this is still unacceptable in a purely statistical sense. We can see significant data excesses at the lower energy sides of the Heα lines of Fe (∼6.5 keV) and Ni (∼7.6 keV). The former is likely due to the incomplete response function. We should note that Fe Heα statics are superior to those for any other objects observed with Suzaku, and no significant residual has appeared so far. If we observe carefully, we find a similar feature in the Mn-Kα line from the onboard calibration source. The latter would be partially due to the same reason given above, but is mainly due to lack of satellite lines of the Li-like and lower ionization states[5] of Ni in the VAPEC model. If we ignore the 6.4–6.6 keV and 7.6–7.7 keV band to escape these effects, an acceptable χ^2/dof of 118/107 is obtained.

[3] See chapter 4 for these notations.
[4] See chapter 4 for details of cascade lines.
[5] As for Fe, such satellite lines are included in the VAPEC model.

Table 5.2—: Best-fit spectral parameters of W49B.

CIE (VAPEC)	kT_e [keV]	Z_{Fe} [solar]	Z_{Ni} [solar]	Normalization[a]
	1.52 (1.50–1.53)	4.44 (4.36–4.53)[b]	10.9 (9.14–12.7)[b]	1.61 (1.60–1.62)
Line		Center energy [keV]	Line width [keV]	Normalization[c]
	Cr Kα	5.655 (5.646–5.663)	0 (fixed)	2.85 (2.59–3.11)
	Mn Kα	6.162 (6.142–6.183)	0 (fixed)	0.957 (0.750–1.16)
	Fe Heα_{rec}[d]	6.666 (fixed[e])	0 (fixed)	5.30 (4.20–6.39)
	Fe Lyα	6.961 (6.946–6.971)	0 (fixed)	1.46 (1.27–1.65)
	Fe Heβ_{rec}[d]	7.880 (fixed[e])	0 (fixed)	0.593 (0.338–0.847)
	Fe Heγ-∞_{rec}[d]	8.538 (8.492–8.585)	0.200 (0.163–0.246)	2.12 (1.81–2.43)
RRC		Edge energy [keV]	kT_e [keV]	Normalization[c]
	Fe He-RRC	8.830 (fixed)	1.43 (1.30–1.59)[f]	11.2 (10.4–11.9)
	Fe H-RRC	9.194 (fixed)	1.43 (1.30–1.59)[f]	0.257 (0.00–1.04)

The uncertainties in the parentheses are the 90% confidence range. [a]The unit is $10^{-13}\int n_e n_H\, dV/(4\pi D^2)$ (cm^{-5}), where n_e, n_H, V, and D are the electron and hydrogen densities (cm^{-3}), emitting volume (cm^3), and distance to the source (cm), respectively. [b]These values should be modified in the case of the overionized plasma. See discussion for W49B for details. [c]The unit is 10^{-5} cm^{-2} s^{-1}. [d]Lines emitted by a recombination process. [e]Fixed at the experimental values (Wargelin et al. 2005). [f]We assumed the same kT_e.

5.3.3 Contribution of Recombination Lines

We have found the strong He-RRC of Fe from W49B. We also discovered RRC-accompanied recombination lines, which may provide good diagnostics for the overionized plasma. We first examine the validity of the best-fit fluxes of the RRC and recombination lines in table 5.2. The recombination cross section of the H-like ions into a level of n is approximately given in equation 4.10. We apply this approximation for the He-like ions, but σ_1 is reduced by half. In principle, the recombination line flux can be estimated by the branching ratio to various levels, but these processes are very complicated. We, therefore, base our discussion only on a simple picture.

We compare the predicted capture and observed transition rates normalized with the $n = 1$ value. We can estimate the capture rates using equation 4.10 as $\sigma_2/\sigma_1 = 0.62$, $\sigma_3/\sigma_1 = 0.25$, and $(\sigma_4 + \sigma_5 + \cdots)/\sigma_1 = 0.34$. On the other hand, the observed flux rates are Heα_{rec}/He-RRC = 0.47 ($\pm$0.10), Heβ_{rec}/He-RRC = 0.053 ($\pm$0.023), and Heγ-∞_{rec}/He-RRC = 0.19 ($\pm$0.03).[6] By taking the fractions between the observed and predicted rates, we obtain 76 ($\pm$16)%, 21 ($\pm$9)%, and 56 ($\pm$9)% for the Heα_{rec}, Heβ_{rec}, and Heγ-∞_{rec} lines, respectively.

These fractions for the Heβ_{rec} and Heγ-∞_{rec} lines may be conceivable, because one electron at $n = 1$ suppresses direct transitions from excited levels ($n \geq 3 \rightarrow 1$) for He-like ions (figure 4.4). The fraction of Heα_{rec} is slightly smaller than expected because there should be a significant contribution of the cascade decay electrons ($n \geq 3 \rightarrow 2 \rightarrow 1$). The real He$\alpha_{rec}$ flux may be somewhat larger, but the Heα_{rec} flux ratio relative to total Heα is only $\lesssim$10% and does not affect results and following discussion.

[6]Throughout this thesis, the errors in the parentheses are at 90% confidence level.

5.3.4 Electron and Ionization Temperatures

The electron temperatures determined by the bremsstrahlung continuum shape and the RRC width are 1.52 (1.50–1.53) keV and 1.43 (1.30–1.59) keV, respectively. These consistent results indicate a common origin of these emissions.

The ionization temperatures are determined from several flux ratios. From the best-fit model in table 5.2, the flux ratios of Lyα/Heα, He-RRC/Heα, and H-RRC/He-RRC are given as 0.016 (0.014–0.018), 0.12 (0.11–0.13), and 0.023 ($\leq$0.10). In figure 5.6, we compare these values with the modeled emissivity ratios derived from the radiation code of Masai (1994) for a plasma of $kT_{\rm e}$ = 1.5 keV. We obtain kT_z = 2.58 (2.46–2.68) keV, 2.68 (2.63–2.73) keV, and 2.55 ($\leq$3.65) keV, respectively, for the above ratios. The ionization temperatures ($\sim$2.7 keV) are significantly higher than the electron temperatures ($\sim$1.5 keV), indicating that the plasma is in a highly overionized state.

The first hint of overionized plasma in W49B was found by Kawasaki et al. (2005). Although they analyzed different elements (Ar and Ca) in different energy bands (2.75–6.0 keV), and derived kT_z from the Lyα/Heα ratio using the CIE plasma code, their results (kT_z $\sim$2.5 keV and $kT_{\rm e}$ $\sim$1.8 keV) are nearly consistent with ours. Our claim is more essential because it is based on clear detection of the recombination structures.

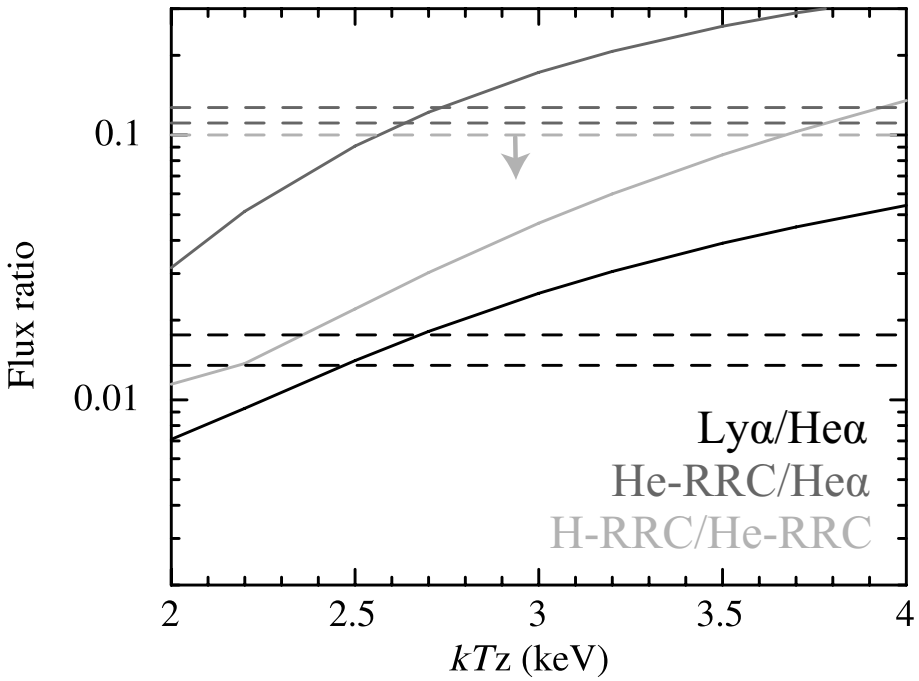

Fig. 5.6.—: Predicted emissivity ratios of Lyα/Heα (black), He-RRC/Heα (dark gray), and H-RRC/He-RRC (light gray) of Fe as a function of the ionization temperature (kT_z) for an electron temperature of 1.5 keV (Masai 1994). The horizontal dashed lines represent 90% errors of the observed values. (Ozawa et al. 2009a)

5.3.5 Abundance Correction for Overionization

The abundances listed in table 5.2 are valid only for the CIE state and should be modified in the overionized case. Since no plasma code can be applied to the overionized plasma currently, we make possible modifications using an available APEC code.

The Heα intensity is proportional to $Z \times \epsilon(kT_{\rm e}, kT_z)$, where Z and $\epsilon(kT_{\rm e}, kT_z)$ are the abundance of the element (solar) and the total emissivity for the Heα for $kT_{\rm e}$ and kT_z (cm^{3}s^{-1}), respectively. The emissivities of the He-, Li-, and Be-like ions for Fe and the He-like ions for Ni are modified by multiplying the ion-fraction ratio between kT_z = 2.7 keV and 1.5 keV (Mazzotta et al. 1998). The total emissivity is given by adding those in individual ionization states. Multiplying by ϵ(1.5 keV, 1.5 keV)/ϵ(1.5 keV, 2.7 keV), we obtain the real abundances in the overionized state as $Z_{\rm Fe}$ $\sim$3.0 solar and $Z_{\rm Ni}$ $\sim$2.8 solar. Both the elements are highly over abundant, indicating an ejecta origin of the plasma.

5.3.6 Volume Emission Measure

To check the consistency of the common origin of the bremsstrahlung and RRC emissions, we compare the volume emission measure (VEM) [7].

The VEM of the VAPEC component (VEM$_{\rm VAPEC}$) is derived from table 5.2 as VEM$_{\rm VAPEC}$ = 1.61 (1.60–1.62) $\times$ 10^{13} cm^{-5}. On the other hand, the VEM of the RRC plasma (VEM$_{\rm RRC}$) is calculated from equation 4.12. According to Badnell (2006), the total radiative recombination rate of He-like Fe at $kT_{\rm e}$ = 1.5 keV is given as $\sim$3.9 $\times 10^{-12}$ cm^{3}s^{-1}. The recombination rate into the ground state is given using equation 4.10 as $\sigma_1/(\sigma_1 + \sigma_2 + \cdots) \sim 0.45$. The value of $n_{\rm Fe}/n_{\rm H}$ is calculated using $Z_{\rm Fe}$ in previous subsection 5.3.5 and the number density of the solar photosphere. Using the observed He-RRC flux, we obtain[8] VEM$_{\rm RRC}$ = 1.3 (1.0–2.6) $\times 10^{13}$ cm^{-5}. The two independent estimations of VEM give consistent results, supporting the same origin of the overionized plasma.

[7] See Section 4.4 for detailed derivation methods.

[8] Here, we consider that the kT_z error is 2.4–2.8 keV. The large error of VEM$_{\rm RRC}$ is due to this effect.

5.4 Results for Segmented Region

In this section, we investigate the spatial distribution of the recombining plasma. We first made count maps to examine the plasma state. Figure 5.7 shows the NXB-subtracted and vignetting-corrected XIS band maps of Fe (a) Heα, (b) Heβ, and (c) He-RRC. All maps exhibit a center-filled structure.

In figure 5.8, we represent the count ratio maps. The ratio Heβ/Heα (a) is an indicator of the electron temperature, while the ratio He-RRC/Heα (b) shows the recombination degree. We can see the He-RRC/Heα ratio is significantly high in the west region.

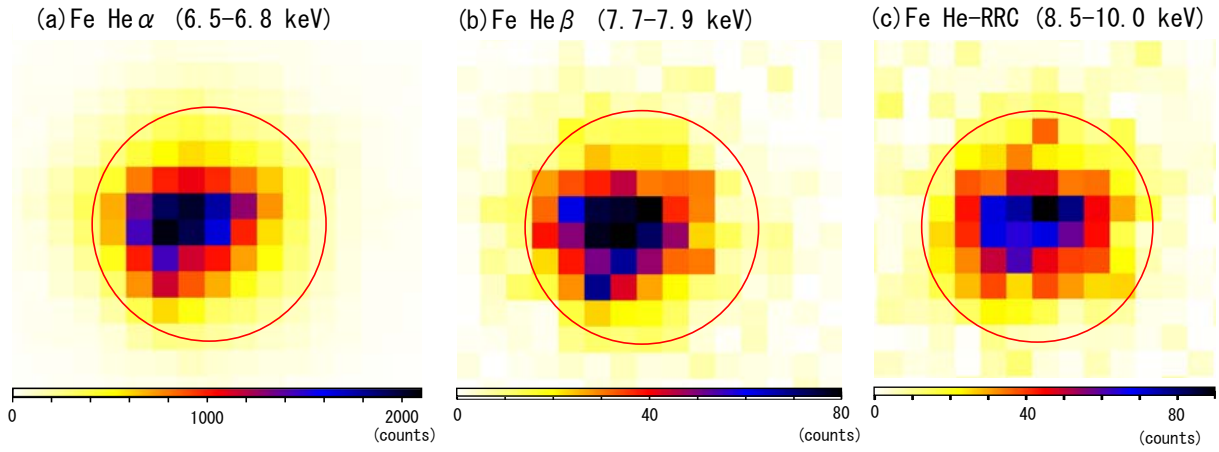

Fig. 5.7.—: NXB subtracted and vignetting corrected XIS FI count maps shown on a linear intensity scale. Each sell in these maps includes 32×32 CCD pixels. The red circle with a radius of 2.5 arcmin corresponds to the source region shown in figure 5.3.

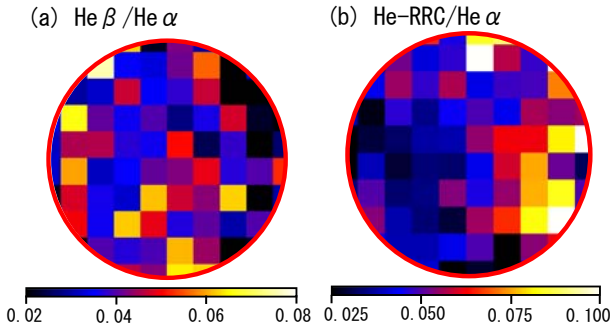

Fig. 5.8.—: XIS FI count ratio maps derived by taking ratios of figure 5.7. (a) Ratio between Fe Heβ (7.7–7.9 keV) and Heα (6.5–6.8 keV). (b) Ratio between Fe He-RRC (8.5–10 keV) and Heα (6.5–6.8 keV). We only show the results of statistically-significant regions inside the red circle with a radius of 2.5 arcmin.

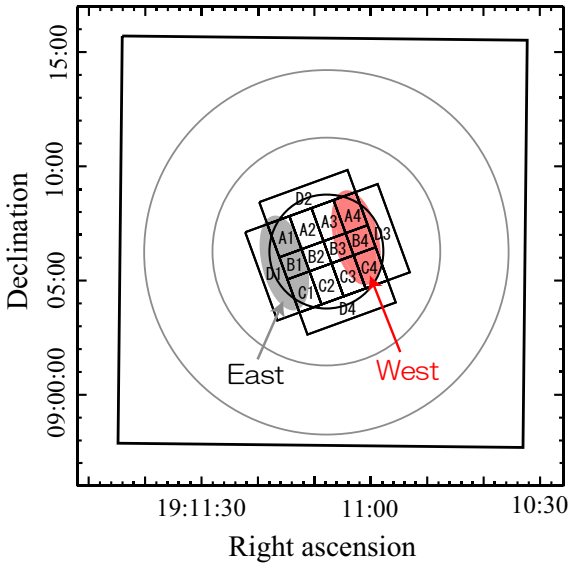

Fig. 5.9.—: Regions used in the segmented analyses. We named Regions A to D and Segment 1 to 4 for a 16-fraction analysis (boxes). Ellipses are East and West regions we used in an east-west analysis. Gray annulus represents the background region. We show the source region used in the global analysis with a black circle as a reference.

16-fraction Analysis

The count ratio map showed a spatial difference of the RRC intensity. In order to quantitatively confirm this implication, we carry out the spectral analysis for the 16 segmented regions (figure 5.9). We subtract the background spectrum taken from the orange annulus in figure 5.9 from the each source spectrum. Then we fit the each spectrum with the same model and energy band with those in table 5.2. Because of the limited photon flux in 16-fraction analysis, however, we take some restrictions into account as below: 1) Fix all the line centers and widths to those in table 5.2. 2) Fix the $Z_{\rm Ni}/Z_{\rm Fe}$ ratio to that in table 5.2. 3) Link electron temperatures of bremsstrahlung and recombination components [9]. 4) Ignore a Fe H-RRC. 5) Fix flux ratios between He$\alpha_{\rm rec}$, He$\beta_{\rm rec}$, Heγ-$\infty_{\rm rec}$, and He-RRC to those in table 5.2 [10].

Figure 5.10 shows the fitted spectra. We can see the flux ratios between recombination (red) and bremsstrahlung (black) components are high in the west and low in the east. Figure 5.11 is the fitting results. Electron temperatures are high in east (Segment 1 and 2), while low in west (Segment 3 and 4). In contrast, He-RRC/Heα ratios are high in west. Ionization temperatures are also high in west reflecting the high He-RRC/Heα ratios. In figure 5.12, we show color maps, which represent the best-fit values in figure 5.11.

[9]This procedure is natural because these components are likely to be the same origin. See section 5.3.4 for details.

[10]Strictly speaking, these ratios depend on the electron temperature. The influence, however, is small in the case of $kT_{\rm e}$ = 1.4-1.6 keV (we confirm these values later). For example, the ratio He$\alpha_{\rm rec}$/He-RRC differs only by 3% in the above $kT_{\rm e}$ range if we estimate from equation 4.10.

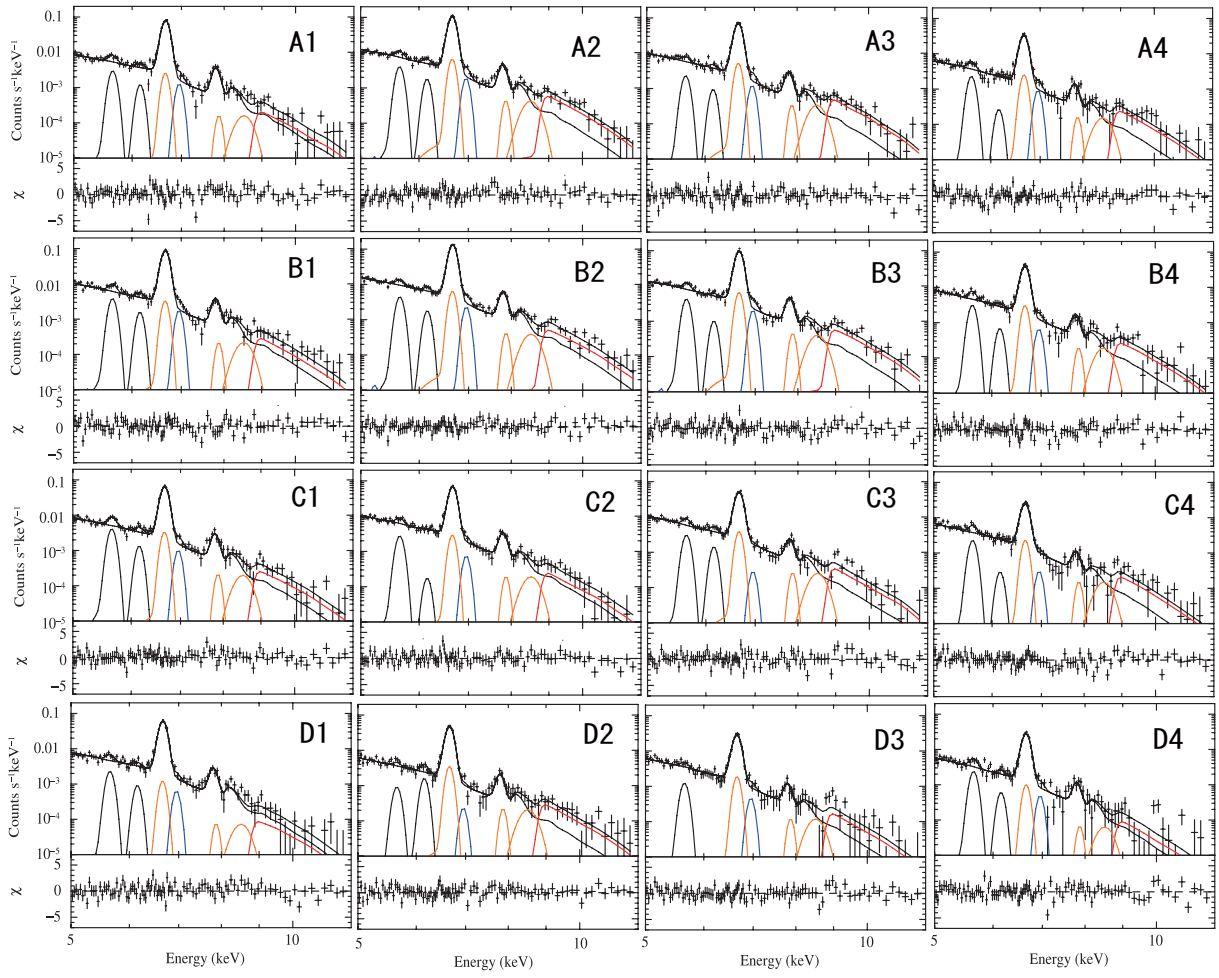

Fig. 5.10.—: Spectral fittings for the 16-fraction analysis. We modeled each spectrum with a CIE component, a Fe Lyα line, He-RRC, and recombination lines.

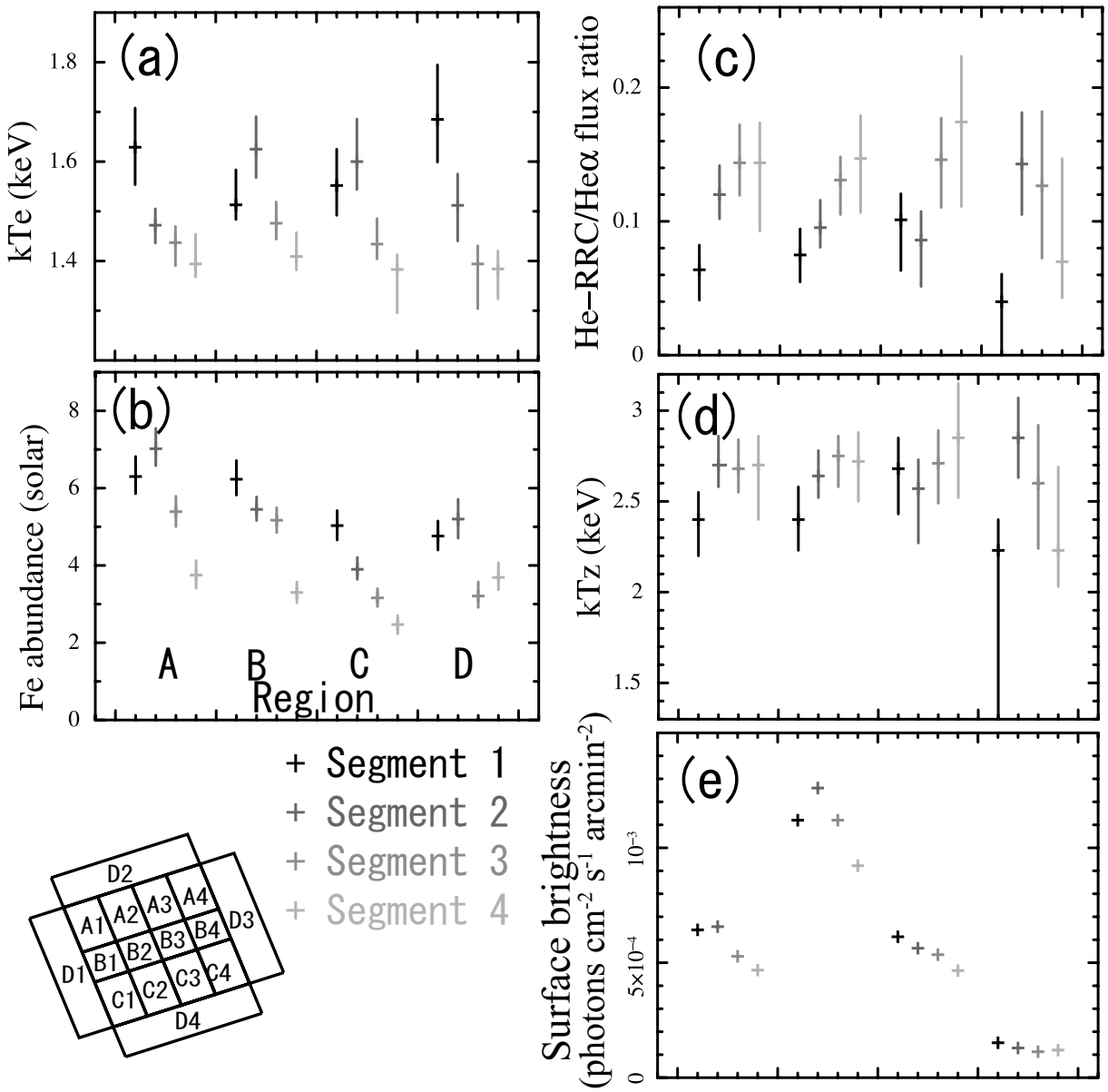

Fig. 5.11.—: Fitting parameters for the 16-fraction analysis. (a) Electron temperatures. (b) Fe abundances. Note that these values should be modified in the overionized case. (c) He-RRC/Heα flux ratios of Fe. (d) Ionization temperatures derived from (d) and a plasma radiation code of Masai (1994). (e) Surface brightness in the 5.0-6.4 keV band. We excluded the Cr and Mn Kα contributions.

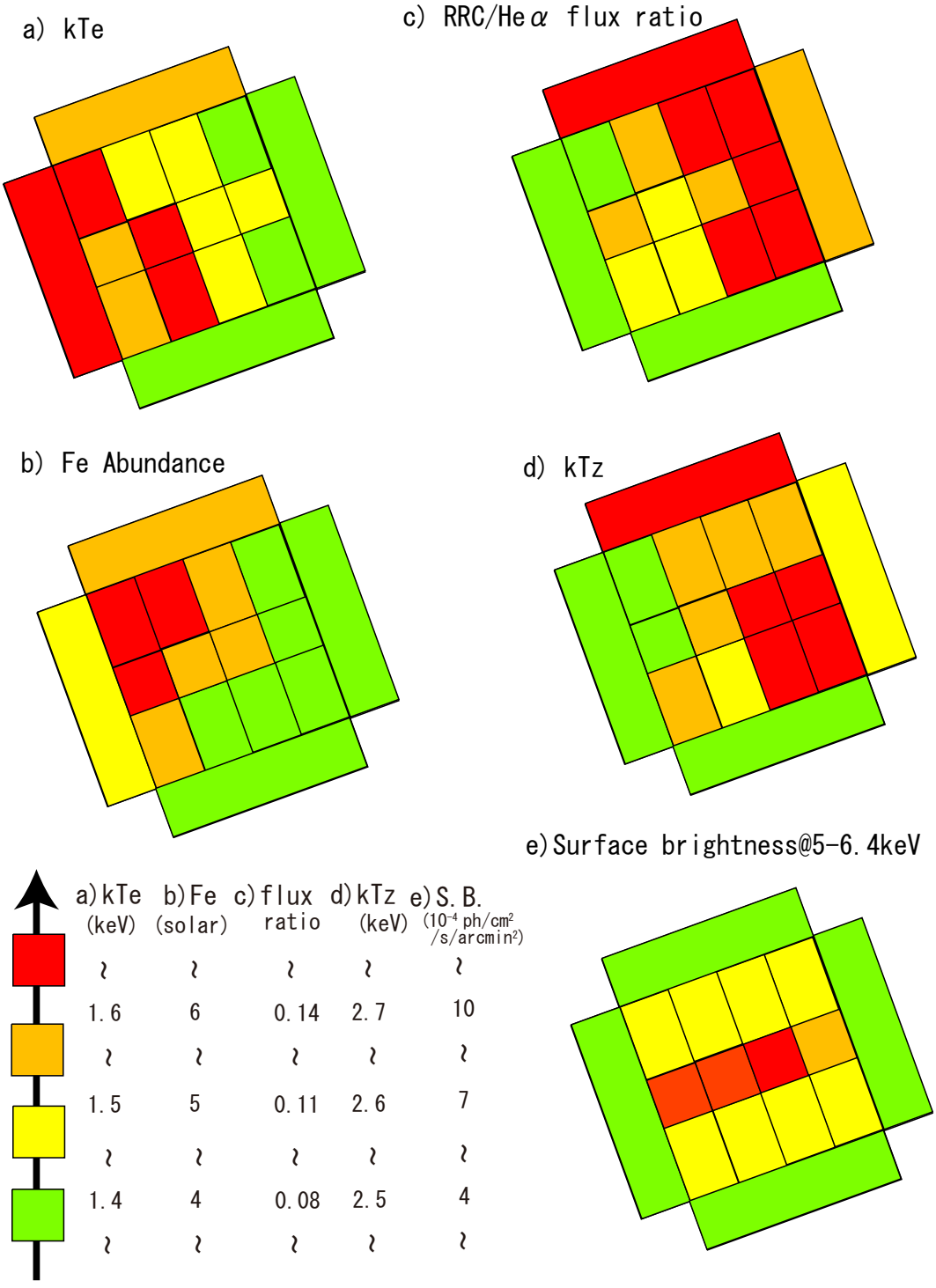

Fig. 5.12.—: Color maps representing the best-fit values of physical parameters which are derived from the 16-fraction analysis. Red, orange, yellow, and green colors are in the order of highest to lowest for the physical parameters. The meanings of (a) to (e) are the same as those in figure 5.11.

East-West Asymmetry Analysis

In the count map and 16-fraction analyses, we can see the anisotropy of physical parameters in the east and west regions of W49B. Hence, we directly investigate the difference between these two regions. We took the spectra from the two ellipse regions in figure 5.9. Hereafter we call "East" and "West" for the east and west ellipse regions, respectively. We took the background spectrum from the orange annulus in figure 5.9 and subtracted it from each source spectrum.

We fitted the spectra with the same model and restrictions with those of 16-fraction analysis. The fitted spectra and best-fit parameters are summarized in figure 5.13 and table 5.3. The line intensity of Fe Heα ($\sim$6.7 keV) and Heβ ($\sim$7.8 keV) is apparently more intense in East than West. On the contrary, the bump around $\sim$9 keV is evidently intense in West.

In figure 5.14, we show the electron and ionization temperatures of the East and West regions. We derived the ionization temperatures from the He-RRC/Heα flux ratios of Fe and figure 4.12. The electron temperature of West ($\sim$1.4 keV) is lower than that of East ($\sim$1.7 keV). On the other hand, ionization temperature of West ($\sim$3.0 keV) is significantly higher than that of East ($\sim$2.6 keV). The recombination and overionization degree is explicit in the West region, where the ionization temperature is more than twice as high as the electron temperature.

Table 5.3—: Best-fit spectral parameters in the East and West regions.

			East	West
CIE (VAPEC)	$kT_{\rm e}$ [keV]		1.64 (1.60–1.68)	1.42 (1.41–1.45)
	$Z_{\rm Fe}$ [solar]		5.18 (5.00–5.37)[a]	3.32 (3.18–3.43)[a]
	$Z_{\rm Ni}$ [solar]		2.45×[$Z_{\rm Fe}$][b]	
	Normalization[c]		0.42 (0.42–0.44)	0.75 (0.72–0.76)
	Center energy[d]	Line width[d]	Normalization[e]	
Cr Kα	5.655 (fixed[g])	0 (fixed)	1.14 (0.97–1.31)	1.10 (0.81–1.20)
Mn Kα	6.162 (fixed[g])	0 (fixed)	0.45 (0.32–0.59)	0.20 (0.06–0.35)
Fe He$\alpha_{\rm rec}$[f]	6.666 (fixed[h])	0 (fixed)	0.47×[RRC Norm][b]	
Fe Lyα	6.961 (fixed[g])	0 (fixed)	0.63 (0.45–0.77)	0.47 (0.34–0.61)
Fe He$\beta_{\rm rec}$[f]	7.880 (fixed[h])	0 (fixed)	0.053×[RRC Norm][b]	
Fe Heγ-$\infty_{\rm rec}$[f]	8.538 (fixed[g])	0.20 (fixed[g])	0.19×[RRC Norm][b]	
Fe He-RRC	Edge energy[d]	$kT_{\rm e}$ [keV]	Normalization[e]	
	8.830 (fixed)	linked[i]	3.01 (2.58–3.41)	4.51 (3.98–4.93)

[a]Should be modified in the overionized case. [b]Linked following table 5.2. [c]The unit is $10^{-13}\int n_e n_{\rm H}\, dV/(4\pi D^2)$ (cm^{-5}), [d] (keV), and [e]10^{-5} (cm^{-2} s^{-1}). [f]Lines emitted by a recombination process. [g]Fixed following table 5.2. [h]Fixed at the experimental values (Wargelin et al. 2005). [i]Linked to $kT_{\rm e}$ of the CIE component (VAPEC).

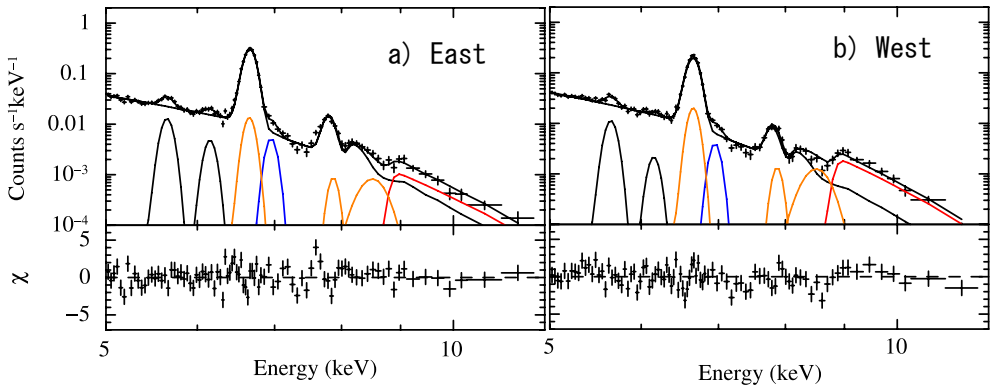

Fig. 5.13.—: Spectral fittings for the (a) East and (b) West regions. We modeled spectra with a CIE component, a Fe Lyα line, He-RRC, and recombination lines.

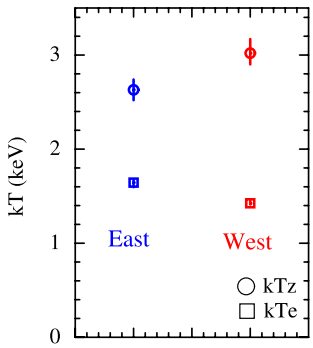

Fig. 5.14.—: Electron and ionization temperatures in the East and West regions of W49B.

5.5 Summary

We have presented an XIS spectrum of unprecedented quality of the Galactic SNR W49B obtained with Suzaku. The results and interpretations are summarized as follows:

- The spectrum exhibits an unusual structure consisting of a saw-edged bump above 8 keV. We firmly conclude that this bump is caused by the strong radiative recombination continuum (RRC) of iron, detected for the first time in an SNR.
- The electron temperature derived from the bremsstrahlung and RRC spectral shape is $\sim$1.5 keV. On the other hand, the ionization temperature derived from the observed intensity ratios between the RRC and lines of iron is $\sim$2.7 keV. Thus, the plasma is in a highly overionized state.
- Volume emission measures independently determined from the fluxes of the bremsstrahlung and recombination components are consistent, suggesting the same emission origin.
- There is significant spatial anisotropy of physical parameters between the west and east area of W49B. The strong plasma recombining region corresponds to the X-ray dim and low electron temperature area.

Chapter 6

IC 443

IC 443 is the first SNR whose plasma was claimed to be in the overionized state by the ASCA data (Kawasaki et al. 2002). The X-ray spectrum exhibits strong Lyα lines of Si and S, suggesting the plasma is highly ionized. Thus, this SNR is the best candidate which possesses a recombining plasma. In this chapter, we summarize the Suzaku results and discuss the plasma state [1].

6.1 Previous Results

IC 443 (G189.1+3.0, 3C157) is a Galactic mixed-morphology SNR. Figure 6.1 shows the multiwavelength view of IC 443. It has a center filled morphology in the X-ray band and a shell-like structure in the radio and optical bands (Rho & Petre 1998; Duin & van der Laan 1975; Braun & Strom 1986; Leahy 2004). It is located at a distance of 1.5 kpc (Welsh & Sallmen 2003) near the Gem OB1 association and a dense giant molecular cloud (Cornett et al. 1977) with OH maser emission (Claussen et al. 1997). A comprehensive X-ray study of IC 443 was first made with the Einstein and HEAO-A2 satellites (Petre et al. 1988). They estimated the SNR age to be $\sim$3000 yr. Recently, Troja et al. (2008) derived the age of $\sim$4000 yr from the morphologies of the shocked ejecta and interstellar medium (ISM) using XMM-Newton data. Thus, IC 443 is a middle-aged SNR. In figure 6.2, we show the XMM-Newton MOS images of IC 443. We can see the ring-shaped structure which is considered to be ejecta recently heated by the reverse shock (figure 6.2b).

The northeast shock front has been decelerated by the encounter with a H I cloud (Denoyer 1978; Dickel et al. 1989; Rho et al. 2001). It is strongly interacting with a nearby giant molecular cloud at several positions along the southern rim (Cornett et al. 1977; Giovanelli & Haynes 1979; Troja et al. 2006).

[1] Details are also in Yamaguchi et al. (2009).

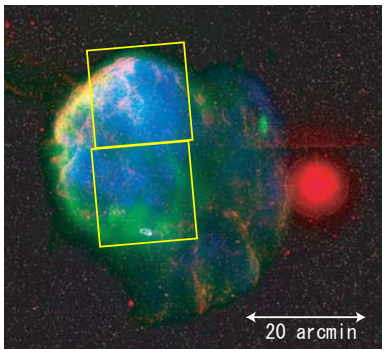

Fig. 6.1.—: Multiwavelength view of IC 443 (Gaensler et al. 2006). (Red) 670 nm emission [Second Palomar Observatory Sky Survey]. The bright star to the west is η Gem. (Green) 1.4 GHz radio data [DRAO Synthesis Telescope]. (Blue) 0.1–2.4 keV X-ray data [ROSAT PSPC]. (White contour) 8.5 GHz data, indicating a pulser wind nebula [Very Large Array]. We superimpose two yellow squares to show Suzaku XIS FOVs. Because IC 443 is extended with a diameter of ∼45 arcmin, two FOVs cannot cover the whole remnant.

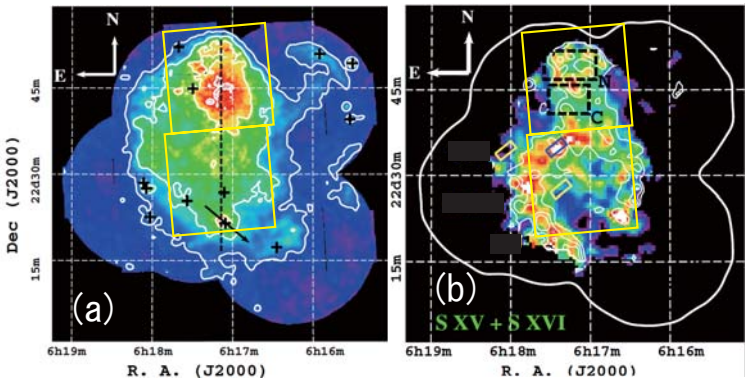

Fig. 6.2.—: XMM-Newton MOS image of IC 443. (a) Count map in the 1.4–5.0 keV energy band. Contour levels correspond to 0.4, 1.0, 2.7, and 5.8 × 10 $^{-2}$ cts s^{-1} arcmin^{-2}. Black crosses mark the position of the 12 hard X-ray point sources identified by Bocchino & Bikov (2003). The black arrow indicates the direction of PWN's motion (Gaensler et al. 2006). (b) Equivalent width map of S lines. We can see the ring-shaped structure. This is considered to be the ejecta recently heated by a reverse shock. Figures are taken from Troja et al. (2008). We superimposed yellow squares to show the XIS FOVs.

The bulk of its X-ray emission is thermal, fairly well described with two CIE components with ∼0.2 and ∼1.0 keV (Petre et al. 1988; Troja et al. 2006). Using Chandra data, Olbert et al. (2001) determined that the hard X-ray source at the southern edge of radio shell is a synchrotron pulsar wind nebula (PWN) powered by a compact source, which is possibly associated with the remnant. Hence, IC 443 is regarded as a core collapse SNR. The PWN can be identified by radio data with white contours in figure 6.1.

A previous ASCA observation revealed that the Lyα fluxes of Si and S are significantly higher than those expected from the electron temperature (Kawasaki et al. 2002). They then derived an ionization temperature of ∼1.5 keV, significantly above the electron temperature of ∼1.0 keV which was determined by its continuum shape of the spectrum. Thus, it was argued that the thermal plasma is in the overionized state (Kawasaki et al. 2002). On the other hand, XMM-Newton found that the plasma is in a CIE, or the overionization is only marginal (Troja et al. 2008).

6.2 Suzaku Observation

Table 6.1—: Observation log of IC 443.

Target	Start Date	Obs.ID	R. A.	Dec.	Exposure
			(J2000.0)		(ks)
IC 443 North	2007-03-06	501006010	$06^h17^m11^s$	$22°46'43''$	42.0
IC 443 South	2007-03-07	501006020	$06^h17^m11^s$	$22°29'02''$	44.0

Suzaku observed IC 443 with two pointings. The observation log is summarized in table 6.1. These two field of views (FOVs) are shown with yellow squares in figure 6.1 and 6.2. Note that IC 443 is extended ∼45 arcmin that two FOVs cannot cover the whole remnant.

Three of the XISs were operated in the normal full-frame clocking mode with a SCI technique during our observations. Two are FI CCDs and the other is a BI CCD. We used HEASOFT version 6.5.1 for data reduction and XSPEC version 11.3.2 for spectral analysis. After screening with the standard criteria, the net integration time is ∼40 ks for both observations.

6.3 Results for Global Region

6.3.1 Overall Structure

Figure 6.3 shows the vignetting-corrected XIS image in 0.7–3.0 keV, the energy band including the major K-shell emission lines from Ne, Mg, Si, and S, and L-shell emission blends from Fe. We can see the X-ray emission covers most of the FOVs, and is bright in the north FOV. We also show the hard (3.0-5.5 keV) emission with orange contours. The bright hard compact source at the southern edge corresponds to the PWN.

We extracted the source spectrum from an X-ray bright region with a 7.5 arcmin radius circle. Because there is no nearby background observation for IC 443, we subtracted the non-X-ray background (NXB) spectrum constructed with the `xisnxbgen` software from the source spectrum. The spectra of the two FI sensors were merged to improve the statistics. Figure 6.4 shows the merged FI spectrum. We can see prominent lines of K-shell emission from He- and H-like ions of O, Ne, Mg, Si, S, Ar, Ca, and Fe as well as L shell emission blends of Fe. We successfully resolved the Fe Kα line for the first time.

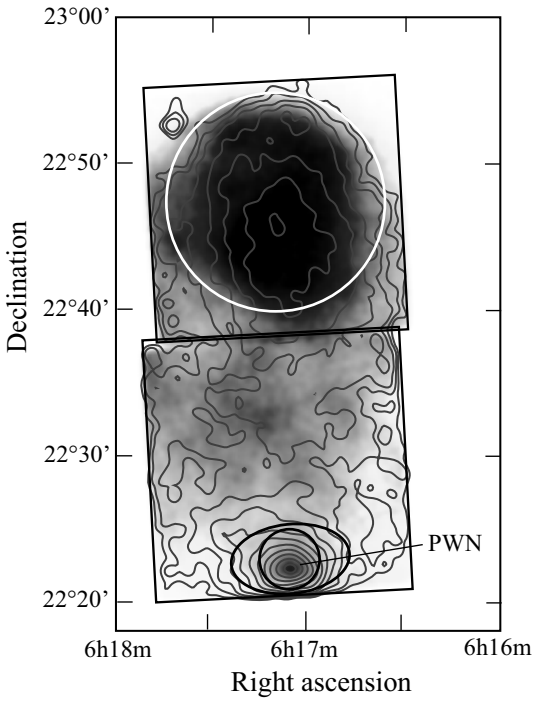

Fig. 6.3.—: Vignetting-corrected XIS image of IC 443 in the soft (0.7–3.0 keV; gray scale) and hard (3.0–5.5 keV; contour) bands shown on a logarithmic intensity scale. Data from the three active XISs are combined. The white circle indicates the source region. The black circle and ellipse are the source and background regions of the pulser wind nebula used in the following segmented analysis. The XIS field of views are shown by black squares.

In figure 6.4, we also show the cosmic X-ray background (CXB) level, which is still included in the NXB-subtracted spectrum. which is modeled following Kushino et al. (2002). This CXB spectrum is given by a power-law with an index of 1.412, and a flux in the 2–10 keV band with 6.38 $\times$ 10^{-8}erg cm^{-2}s^{-1}sr^{-1}. Throughout the spectral fitting, we fixed the CXB to the above value. Note that the contribution of the Galactic ridge emission is negligible because IC 443 is located at the Galactic anti-center direction (l=189.1).

6.3.2 Spectral Analysis

As shown in figure 6.4, the wide-band spectrum includes too many emission lines and possibly other complicated structures. In order to precisely examine the ionization states of Si and S, we hereafter focus on the spectrum in the 1.75–6.5 keV energy band. During the spectral analysis, we fixed the interstellar extinction to a hydrogen column density of 7×10^{21} cm^{-2} with the solar elemental abundances, following Kawasaki et al. (2002) and Troja et al. (2008).

The centroids of the Lyα lines of Si and S for the FI spectrum are measured with a power-law and Gaussian line model, and compared with the canonical values of the Astrophysical Plasma Emission Database (APED: Smith et al. 2001). The averaged center energy difference was +4 eV. Therefore, we added a 4 eV offset in the FI spectrum. In the same way, an offset of -8 eV was added to correct the energy scale for the BI spectrum.

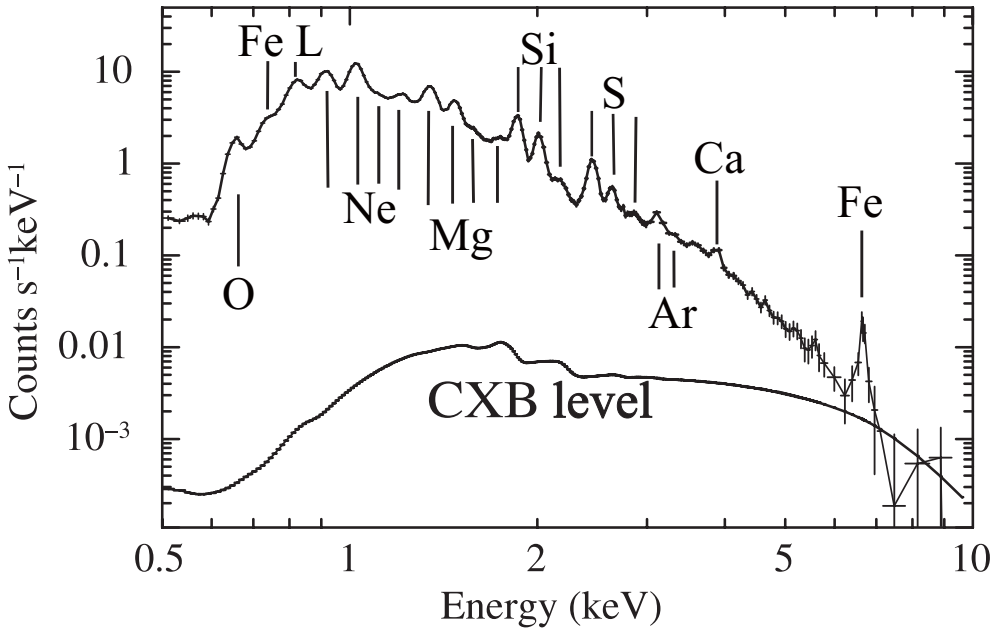

Fig. 6.4.—: NXB-subtracted XIS FI spectrum extracted from the red circle region in figure 6.3. The contribution of the cosmic X-ray background which is still included in the spectrum is shown by a solid line.

CIE Model Fitting

We first fitted the spectrum with a VAPEC model. The Si, S, and Ar abundances (hereafter $Z_{\rm Si}$, $Z_{\rm S}$, and $Z_{\rm Ar}$) were free parameters, while the Ca abundance ($Z_{\rm Ca}$) was tied to that for Ar because the Ca Kα line is not intense enough to independently determine the value. In the initial fit, we found a significant inconsistency between the FI and BI spectra around 1.84 keV, which corresponds to the neutral Si K-edge energy. This is due to the well-known calibration issue of the XIS. Since the calibration for the FI is currently better than that of the BI, we decided to ignore below 1.9 keV for the BI spectrum.

Figure 6.5a shows the fitting result of the one-VAPEC model, with a temperature of 1.1 keV. The model exhibited significant excess around the Lyα lines of S and Ar, and around 2.7 keV and 3.5 keV, and hence was rejected with a large χ^2/dof of 1466/242.

We then tried a two-VAPEC model, assuming equal abundances between the two components. However, it did not improve the fit with the temperatures of $\sim$0.2 keV and $\sim$1.1 keV, and the results were essentially the same as figure 6.5a with a large χ^2/dof of 1431/240. Adding a further plasma model component did not improve the fitting any more. In every case, the bumps around 2.7 keV and 3.5 keV were present.

We checked the light curves of the source region in the 2.5–4.0 keV band. They showed almost constant fluxes, indicating no flare-like event had occurred during the observations. We detected the bumps in all XIS sensors. Thus, the bumps are real structures.

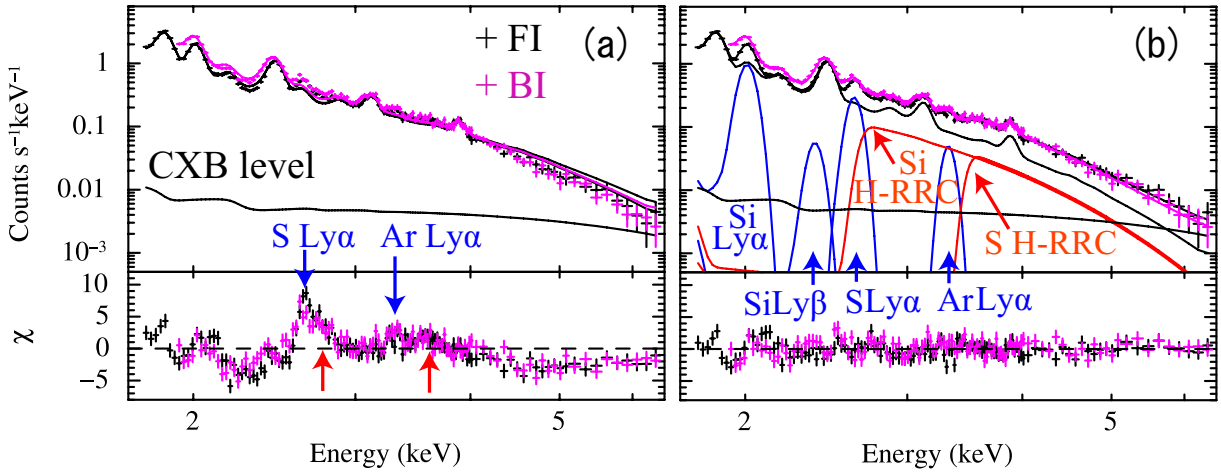

Fig. 6.5.—: (a) XIS spectra in the 1.75–6.5 keV band. The best-fit VPAEC model is shown by a solid line. The lower panel shows the residuals from the best-fit model. There are bumps at the energies of Lyα lines of S and Ar (down-pointing arrows), and around 2.7 keV and 3.5 keV (up-pointing arrows). (b) Same as (a), but with radiative recombination continua of Si and S and Lyα and Lyβ lines of Si, S, and Ar. The residuals seen in (a) have disappeared.

Recombination Structures

The energies of the bumps at ∼2.6 keV and ∼3.3 keV correspond to the Kα potential energies of H-like S and Ar ions, respectively. On the other hand, around the energies of the bumps for ∼2.7 keV and ∼3.5 keV, there is no emission line candidate for an abundant element. Furthermore, these bumps are too broad to be accounted for by a single emission line. The lower edges of unidentifiable bumps correspond to the electron K-shell binding potentials of H-like Si (2.666 keV) and S (3.482 keV). This suggests that these bumps are likely due to RRC.

We hence introduced the RRC and Lyα lines of abundant elements (Si, S, and Ar). Lyβ lines of these elements are also introduced, but they are not significant except for Si. The widths and center energies of these lines are fixed at zero and their theoretical values, respectively. The fluxes of all lines are free parameters. We assume that the RRC is expressed following equation 4.7. This formula gives a good approximation when $kT_{\rm e} \ll E_{\rm edge}$. In the case of IC 443, $kT_{\rm e}$ is ∼0.7 keV, as we confirm later, while $E_{\rm edge}$ of Si and S are ∼2.7 keV and ∼3.5 keV, respectively. Thus, we can safely adopt this formula. During the fitting in this subsection, we ignore the cascade lines. We consider them in subsection 6.3.3.

The resultant best-fit parameters and models are given in table 6.2 and figure 6.5b, respectively. With this model, χ^2/dof is greatly improved to 331/235, although this is still unacceptable in a purely statistical sense. This would be partially due to the calibration uncertainty. We can see the wave-shaped residuals in figure 6.5b around ∼2 keV. The XIS calibration around ∼2 keV is difficult and uncertainty of the gain and response is relatively high because there is a very limited number of calibration sources which can be used in this energy band. If we ignore below 2.1 keV, a χ^2/dof of 251/208 with null hypothesis probability of 0.021 is obtained. In this chapter, we discuss the implications based on the result in table 6.2.

Table 6.2—: Best-fit spectral parameters of IC 443.

CIE (VAPEC)	$kT_{\rm e}$ [keV]	0.74 (0.71–0.78)		
	$Z_{\rm Si}$ [solar]	0.82 (0.79–0.89)[b]		
	$Z_{\rm S}$ [solar]	1.40 (1.34–1.44)[b]		
	$Z_{\rm Ar}$=$Z_{\rm Ca}$ [solar]	1.96 (1.76–2.10)[b]		
	Normalization[a]	1.66 (1.56–1.75)		
Line		Center energy [keV]	Width [keV]	Normalization[c]
	Si Lyα	2.006 (fixed)	0 (fixed)	76 (69–78)
	Si Lyβ	2.377 (fixed)	0 (fixed)	5.5 (3.8–7.0)
	S Lyα	2.623 (fixed)	0 (fixed)	25 (23–26)
	Ar Lyα	3.323 (fixed)	0 (fixed)	3.7 (3.1–4.3)
RRC		Edge energy [keV]	$kT_{\rm e}$ [keV]	Normalization[c]
	Si H-RRC	2.666 (fixed)	0.58 (0.53–0.62)[d]	51 (45–55)
	S H-RRC	3.482 (fixed)	0.58 (0.53–0.62)[d]	13 (12–15)

[a]The unit is $10^{-13} \int n_e n_{\rm H}\, dV/(4\pi D^2)$ (cm^{-5}), where n_e, $n_{\rm H}$, V, and D are the electron and hydrogen densities (cm^{-3}), emitting volume (cm^3), and distance to the source (cm), respectively. [b]Should be modified in the overionization case (subsection 6.3.5). [c]The unit is 10^{-5} cm^{-2} s^{-1}. [d]We assumed the same $kT_{\rm e}$.

6.3.3 Contribution of Recombination Lines

We have found the strong H-RRC of Si and S from IC 443 for the first time, hence there should be accompanying recombination (cascade) lines. We first examine the contribution of cascade lines. In the spectral analysis, we required the Lyα lines of Si, S, and Ar, and Lyβ of Si. These lines are partially due to a greater number of H-like ions in the overionized state than in the CIE, and the remains originate from the recombination process. In the previous analysis, however, we did not consider the cascade lines from upper levels (n$\geq$4$\rightarrow$1). Here we estimate this effect.

We fix the contribution of the cascade lines of H-like Si and S using equation 4.10. We assume the electrons trapped in the upper levels straightforwardly fall into the ground state in the case of H-like ions. Based on this assumption, the prospective flux ratios of Ly$\alpha_{\rm rec}$/H-RRC, Ly$\beta_{\rm rec}$/H-RRC, and Lyγ-$\infty_{\rm rec}$/H-RRC are derived from σ_2/σ_1, σ_3/σ_1, and $(\sigma_4+\sigma_5+\sigma_6+...)/\sigma_1$, respectively. The resultant ratios are 0.27, 0.10, and 0.13 for Si, and 0.29, 0.12, and 0.15 for S, respectively. In the following fitting, we fix these ratios to above values.

The widths and center energies of Ly$\alpha_{\rm rec}$ and Ly$\beta_{\rm rec}$ are fixed to 0 and theoretical values, respectively. Those of Lyγ-$\infty_{\rm rec}$ are derived using the results of W49B as follows. The center energy is determined assuming the equation

$$\frac{E({\rm He}\gamma\text{-}\infty_{\rm rec})}{E({\rm He}\alpha_{\rm rec})} = \frac{E({\rm Ly}\gamma\text{-}\infty_{\rm rec})}{E({\rm Ly}\alpha_{\rm rec})}, \tag{6.1}$$

where $E({\rm He}\gamma\text{-}\infty_{\rm rec})$, $E({\rm He}\alpha_{\rm rec})$, $E({\rm Ly}\gamma\text{-}\infty_{\rm rec})$, and $E({\rm Ly}\alpha_{\rm rec})$ are the observed center energy of Fe Heγ-$\infty_{\rm rec}$ for W49B (8.538 keV), the fixed one of Fe He$\alpha_{\rm rec}$ for W49B (6.666 keV), the one we want to know of Si (or S) Lyγ-$\infty_{\rm rec}$ for IC 443, and the theoretical one of Si (or S) Ly$\alpha_{\rm rec}$ (2.006 keV for Si and 2.623 keV for S), respectively. In the same way, the width is determined assuming the equation

$$\frac{W({\rm He}\gamma\text{-}\infty_{\rm rec})}{E({\rm He}\gamma\text{-}\infty_{\rm rec})} = \frac{W({\rm Ly}\gamma\text{-}\infty_{\rm rec})}{E({\rm Ly}\gamma\text{-}\infty_{\rm rec})}, \tag{6.2}$$

where $W({\rm He}\gamma\text{-}\infty_{\rm rec})$ and $W({\rm Ly}\gamma\text{-}\infty_{\rm rec})$ are the observed line width of Fe Heγ-$\infty_{\rm rec}$ for W49B (0.200 keV), and the one we want to know of Si (or S) Lyγ-$\infty_{\rm rec}$ for IC 443, respectively. The resultant center energies and widths of Lyγ-$\infty_{\rm rec}$ are 2.57 keV and 0.060 keV for Si, and 3.36 keV and 0.078 keV for S, respectively.

We fix center energies and widths of cascade lines and fit the spectra (figure 6.6). The resultant parameters including the temperatures of the bremsstrahlung and recombining components ($\sim$0.74 keV and $\sim$0.57 keV, respectively), and the RRC fluxes ($\sim 5.0 \times 10^{-4}$cm^{-2} s^{-1} for Si H-RRC and $\sim 1.4 \times 10^{-4}$cm^{-2} s^{-1} for S H-RRC) do not significantly differ from those in table 6.2 within the margin of statistical error. Thus we can safely say that the inclusion of cascade lines does not change the result.

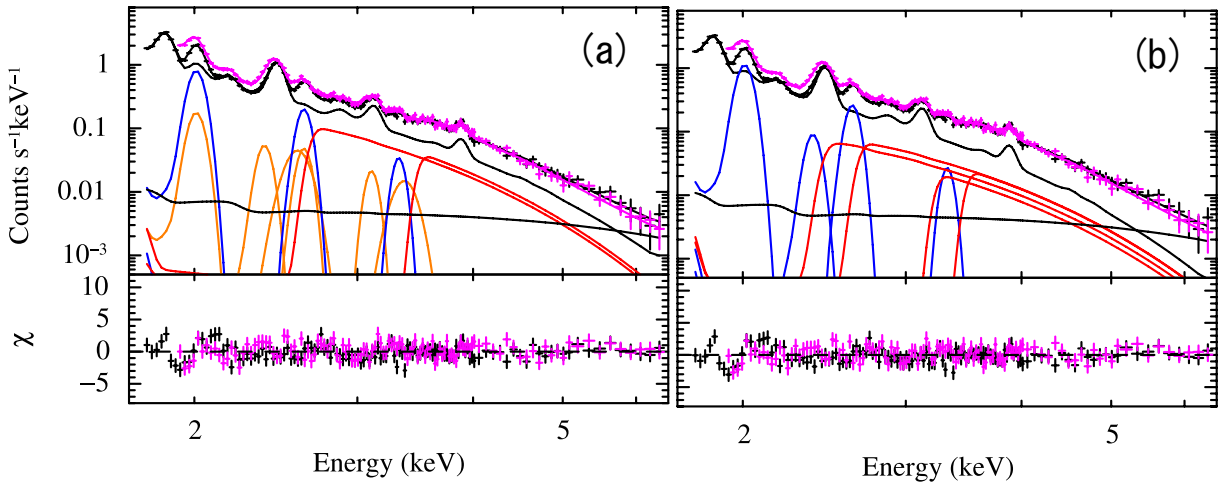

Fig. 6.6.—: (a) Same as figure 6.5b, but cascade lines (Ly$\alpha_{\rm rec}$, Ly$\beta_{\rm rec}$, and Lyγ-$\infty_{\rm rec}$) of H-like Si and S are added. (b) Same as figure 6.5b, but He-RRC of Si and S are added.

6.3.4 Electron and Ionization Temperatures

The electron temperatures in table 6.2 determined by the bremsstrahlung and RRC shapes are 0.74 (0.71–0.78) keV and 0.58 (0.53–0.62) keV, respectively. The $kT_{\rm e}$ derived from the bremsstrahlung is slightly higher than that from the RRC. However, if we introduce the He-RRC of Si and S (figure 6.6b), $kT_{\rm e}$ become 0.68 (0.65–0.72) keV and 0.62 (0.57–0.65) keV for each component. This procedure is natural, because in the case of kT_z ∼1.0 keV for Si and kT_z ∼1.2 keV for S as we confirm later, fully-ionized/H-like ion fraction ratios are ∼1/2 for Si and ∼1/5 for S. Considering that the recombination cross section into the ground state for fully-ionized ions is about twice as large as H-like ions, the resultant He-RRC flux is reasonable. Although we cannot strongly insist the existence of the He-RRC, it is plausible to think a common origin of the bremsstrahlung and recombining components with $kT_{\rm e}$ ∼0.7 keV.

The ionization temperatures are derived from H-RRC/Heα flux ratios of Si and S using figure 4.12. From the best-fit model in table 6.2, these ratios are given as 0.11 (±0.01) and 0.075 (±0.01), respectively. Assuming $kT_{\rm e}$ = 0.7 keV, we obtain kT_z = 0.96 (±0.04) keV for Si and 1.18 (±0.05) keV for S. The ionization temperatures (0.9–1.2 keV) are significantly higher than the electron temperatures (0.5–0.8 keV), confirming that the plasma is in a highly overionized state.

Kawasaki et al. (2002) found the first hint of overionized plasma in IC 443. Because they derived $kT_{\rm e}$ without considering the contribution of the RRC, they obtained relatively high value of ∼1.0 keV. They derived kT_z ∼ 1.5 keV from the Lyα/Heα ratio of S using the CIE plasma code. Our claim of overionization is more essential because it is based on clear detection of the RRC.

6.3.5 Abundance Correction for Overionization

The abundances listed in table 6.2 are valid only for the CIE state and should be modified in the overionized case. We make modifications using an available APEC code.

The Heα intensity is proportional to $Z \times \epsilon(kT_{\rm e}, kT_z)$, where Z and $\epsilon(kT_{\rm e}, kT_z)$ are the abundance of the element (solar) and the total emissivity for the Heα for $kT_{\rm e}$ and kT_z (cm^{3}s^{-1}), respectively. In the kT range of 0.7–1.2 keV, most Kα emissions of Si or S originate from He-like ions. Hence, the emissivity of the He-like ions is modified by multiplying the ion-fraction ratio between kT_z = 1.0 keV (for Si) or 1.2 keV (for S) and 0.7 keV. The ion fraction of Si in kT_z = 0.7 keV and 1.0 keV are 0.72 and 0.35, respectively. Thus, we can obtain the real abundance of Si is 0.82 $\times$ (0.72/0.35) $\sim$1.7 solar. In the same way, the ion fraction of S in kT_z = 0.7 keV and 1.2 keV are 0.90 and 0.59, respectively. Thus, we obtain the real abundance of S is 1.4 $\times$ (0.90/0.59) $\sim$2.1 solar.

6.3.6 Volume Emission Measure

We compare VEM to check the consistency of the common origin of the bremsstrahlung and RRC emissions. The VEM of the VAPEC component is derived from table 6.2 as $\sim 1.7 \times 10^{13}$ cm^{-5}. On the other hand, the VEM of the RRC plasma (VEM$_{\rm RRC}$) is calculated using equation 4.12. According to Badnell (2006), the total radiative recombination rate at $kT_{\rm e}$ = 0.7 keV is given as $\sim 2.0 \times 10^{-12}$ cm^{3}s^{-1} for H-like Si. The recombination rate into the ground state is given using equation 4.10 as $\sigma_1/(\sigma_1+\sigma_2+\cdots) \sim 0.67$. The value of $n_{\rm Si}/n_{\rm H}$ is calculated using $Z_{\rm Si}$ in the previous subsection. Using the observed H-RRC flux of Si and $\kappa_{\rm fully-ionized(Si)}(1.0\ {\rm keV}) = 0.19$, we obtain VEM$_{\rm RRC(Si)}$ $\sim 3.3 \times 10^{13}$ cm^{-5}. In the same way for S, using the total radiative recombination rate $\sim 2.8 \times 10^{-12}$ cm^{3}s^{-1}, $\sigma_1/(\sigma_1+\sigma_2+\cdots) \sim 0.64$, and $\kappa_{\rm fully-ionized(S)}(1.2\ {\rm keV}) = 0.06$, we obtain VEM$_{\rm RRC(S)}$ $\sim 3.7 \times 10^{13}$ cm^{-5}. These values are almost consistent with that of the bremsstrahlung component. Two independent estimations of VEM give nearly consistent results, supporting the same origin of the bremsstrahlung and recombination components in IC 443.

6.4 Results for Segmented Region

In this section, we investigate the spatial distribution of the recombining plasma. We divided each FOV into 16 regions as is shown in figure 6.7. We name Region A to H from north to south, and Segment 1 to 4 from east to west. We used only FI data for simplicity in this section. We subtract the NXB spectrum from each source spectrum. We modeled the CXB with a power-law model.

The PWN detected nearly at the edge of the south FOV is reported to be extended ∼2 arcmin (Gaensler et al. 2006). We therefore modeled the PWN spectrum and fixed it during the analysis. We extracted the PWN spectrum from the blue circle region in figue 6.3 with a radius of 2 arcmin and background from the surrounding ellipse region. The background subtracted spectrum is well approximated by a power-law model with a photon index of $\Gamma = 1.78$ and interstellar extinction of $N_{\rm H} = 4.4 \times 10^{21}$ cm^{-2} (figure 6.8). During the fitting in Region G and H in figure 6.7, we fixed the "shape" of the PWN spectrum with this model. The normalization of this component is a free parameter.

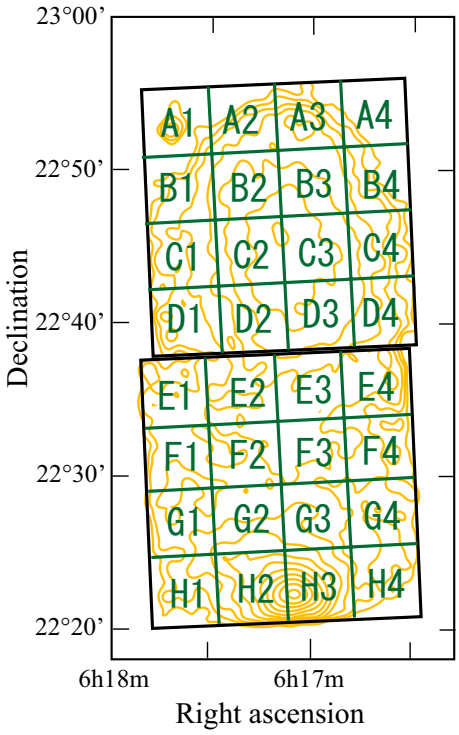

Fig. 6.7.—: Segmented regions used in our analysis. We named Region A to H from north to south, and Segment 1 to 4 from east to west. Contours indicate hard (3.0-5.5 keV) X-ray intensity on a logarithmic scale.

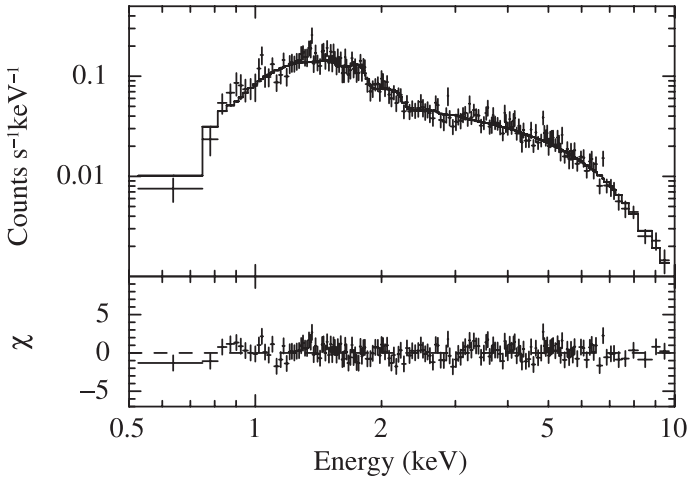

Fig. 6.8.—: Background subtracted spectrum of the pulser wind nebula. The best-fit power-law model is shown by a solid line.

We fitted each spectrum with the same model and energy band with those in table 6.2. Because of the limited photon statics, however, we ignored the Si Lyβ line. We further linked the temperatures of the CIE and RRC components because it is plausible that these components are the same origin. Figure 6.9 shows the fitted spectra. We excluded regions A1 and A4 because of poor statics. We can see the flux ratio between the RRC (red) and CIE (black) components is high around the border area of the two FOVs, while low in the X-ray bright north area.

We can see the hard X-ray component representing the PWN spectrum (shown in green curves in figure 6.9) significantly contaminate G1–G3 and H1–H3 regions. We should note that at the boundary regions of G2 and G3, and G1 and H1, hard X-ray point sources are detected with Chandra (Bocchino & Bicov 2003; the black crosses in figure 6.2). The fluxes of these two sources in the 2.0–10.0 keV band are both around one tenth of the PWN. Hence, the power-law spectra in these regions would include the emission from these point sources. Because spectra of these point sources are unclear, we should care that the systematic uncertainty of the parameters derived from Region G and H is high.

Figure 6.10 is the fitting results. We show the parameters of electron temperatures (a), $Z_{\rm Si}$ (b) and $Z_{\rm S}$ (c) without correction of the overionization effect, H-RRC/Heα ratios of Si (d), ionization temperatures derived from the Si H-RRC/Heα ratios and figure 4.12 (e), and surface brightness in the 1.75–6.5 keV band excluding PWN and CXB contributions (f).

Electron temperatures are high in the X-ray bright north region (Region A, B and C, especially in Segment 2 and 3), while low in the dim region (Region D, E, F, and G). The H-RRC/Heα ratio of Si, which is a good indicator for the recombination degree, is low in the X-ray bright region, while high in the dim regions. In figure 6.11, we show color maps, which represent the best-fit values in figure 6.10.

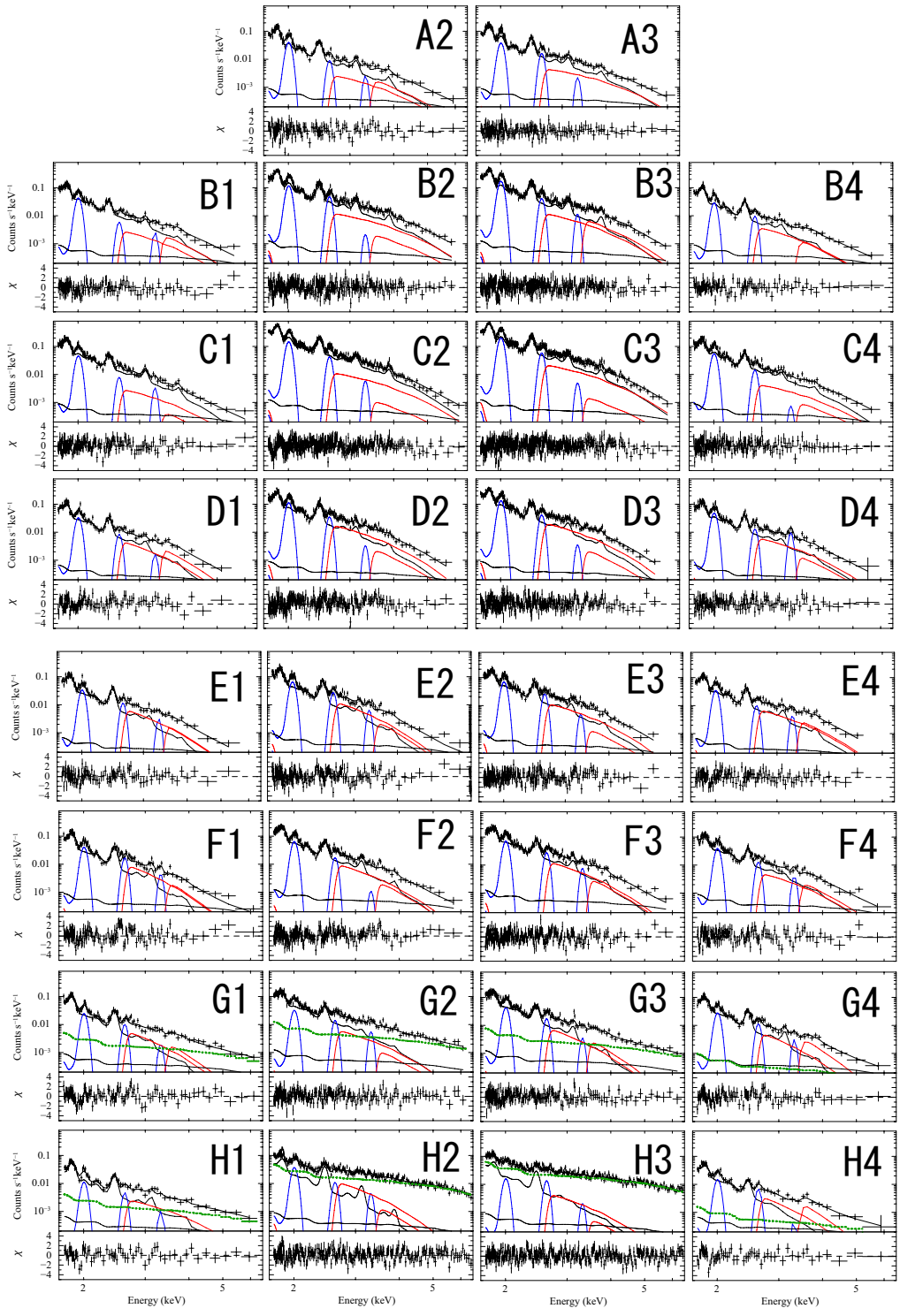

Fig. 6.9.—: Spectral fittings for the segmented regions. We modeled each spectrum with a CIE component, Lyα lines of Si, S, and Ar, and H-RRC of Si and S. The dotted curves represents the contribution of the pulser wind nebula and possibly other point sources.

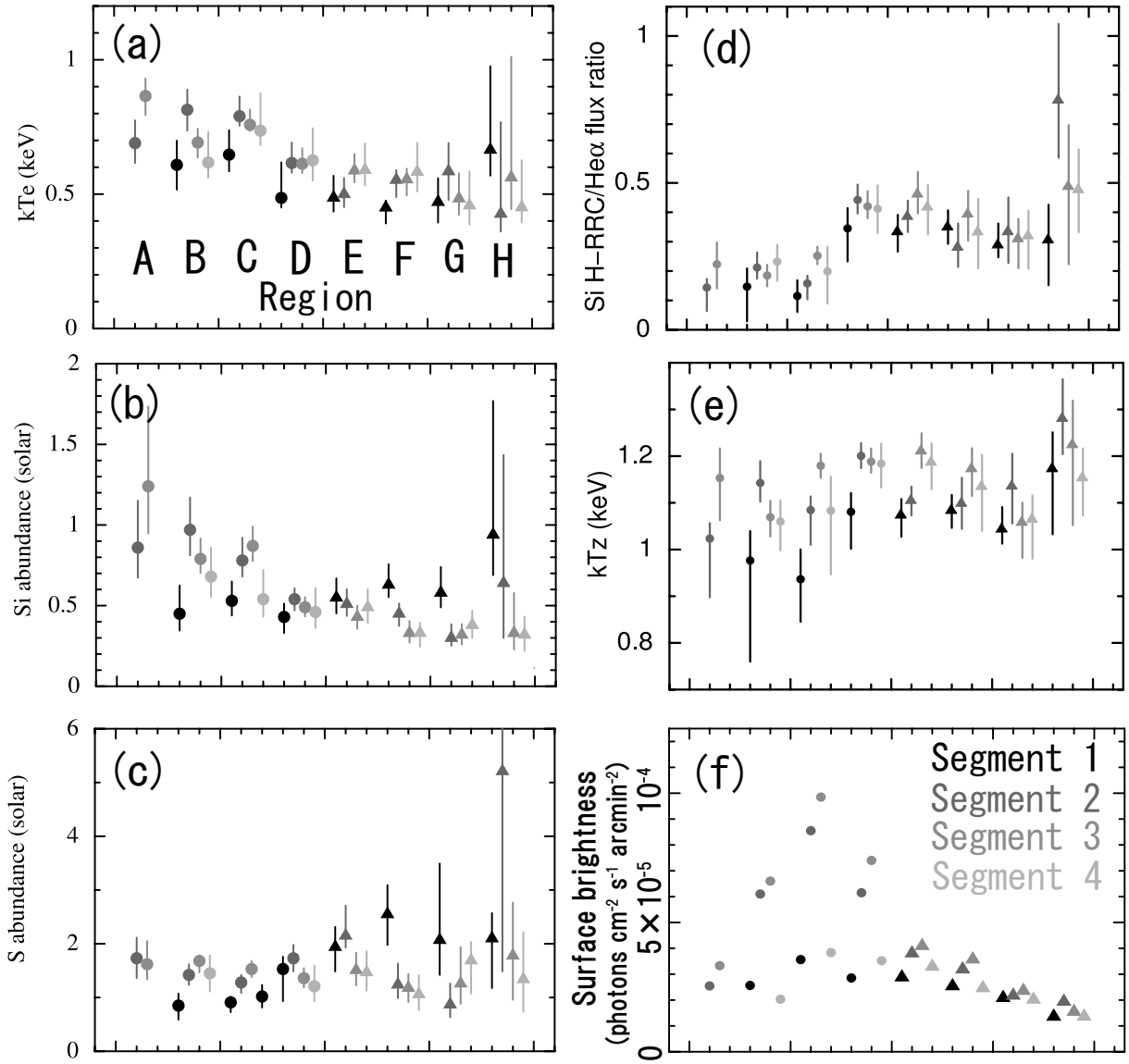

Fig. 6.10.—: Fitting parameters for the segmented analysis. (a) Electron temperatures. Si (b) and S (c) abundances. Note that these values should be modified in the overionized case. (d) H-RRC/Heα flux ratios of Si. (e) Ionization temperatures derived from (d) and a plasma radiation code of Masai (1994). (f) Surface brightness in the 1.75–6.5 keV band. We excluded the PWN and CXB contribution.

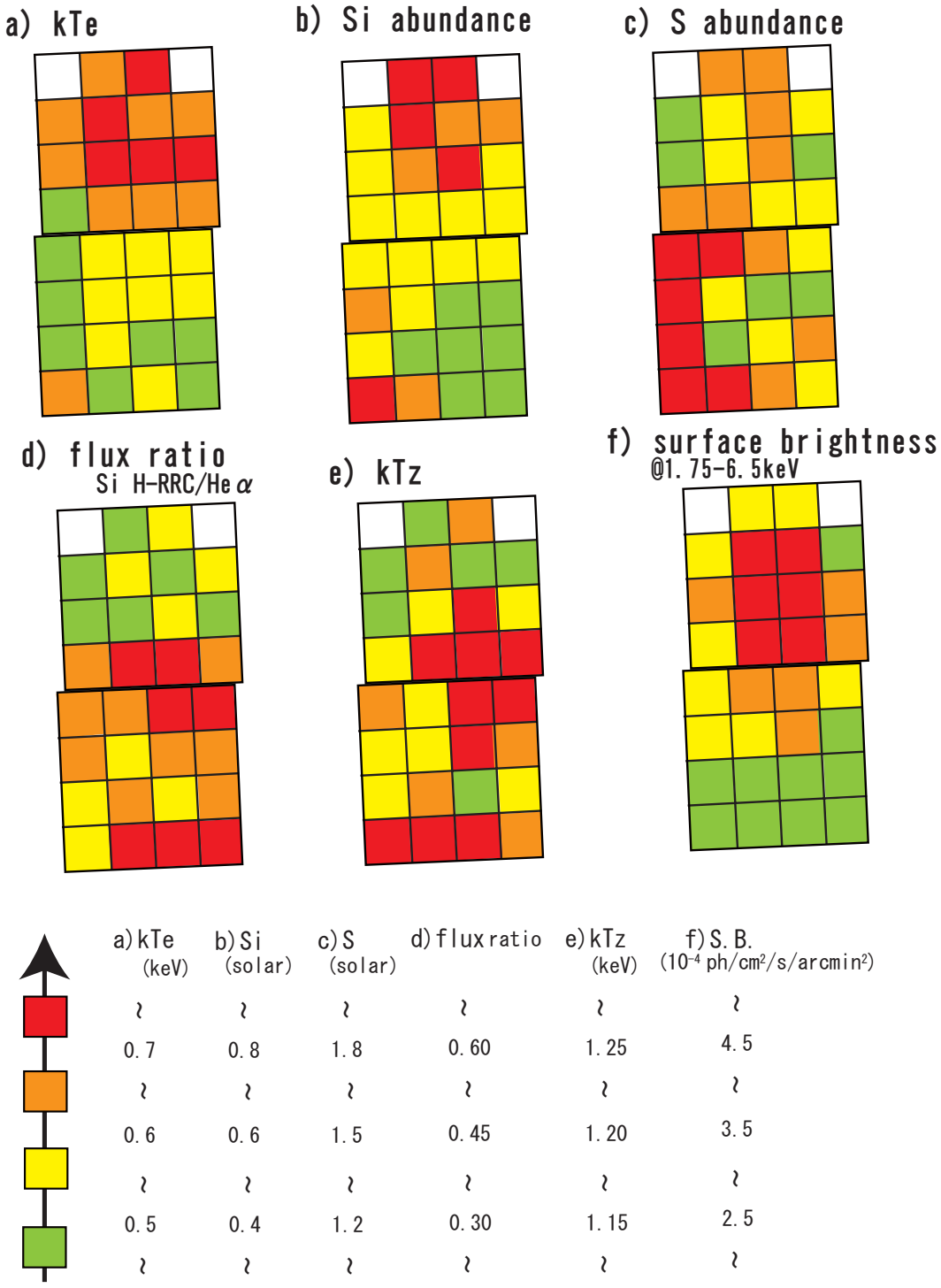

Fig. 6.11.—: Color maps derived from the segmented analysis. Red, orange, yellow, and green colors are in the order of highest to lowest for the physical parameters. The meanings of (a) to (f) are the same as figure 6.10.

6.5 Summary

We have presented the Suzaku XIS spectroscopic study of IC 443 in the X-ray bright north region. We have also examined the spatial distribution of the physical parameters. The results and interpretations are summarized as follows:

- Many emission lines from highly ionized heavy elements are clearly detected. Fe XXV Kα is resolved for the first time.
- The X-ray spectrum in the 1.75–6.0 keV band is described by a thin-thermal plasma with the electron temperature of ~ 0.7 keV and several additional Lyman lines. In addition, we firmly detect strong RRC of H-like Si and S for the first time.
- The ionization temperatures of Si and S determined from the intensity ratio between the RRC and He-like Kα line are ~ 1.0 keV and ~ 1.2 keV, respectively. We thus find evidence for strongly recombining and highly overionized plasma.
- Volume emission measures independently determined from the fluxes of the bremsstrahlung and recombination components are almost consistent, indicating the same plasma origin.
- Spatial analysis indicates the significant anisotropy of physical parameters in IC 443. Strongly recombining region corresponds to the high gradient area of the electron temperature and surface brightness.

Chapter 7

G359.1-0.5

Bamba et al. (2000) claimed that the ionization degree of Si and S in the Galactic SNR G359.1-0.5 is high using the ASCA data. Thus, this SNR is a candidate of the overionized and recombining plasma. We present a Suzaku spectroscopic analysis of G359.1-0.5.

7.1 Previous Results

G359.1-0.5 was identified as an SNR by radio observations (Downes et al. 1979). Uchida, Morris, and Yusef-Zadeh (1992) found the structure of the radio continuum emission surrounded by the ^{12}CO ring. Comparing the 21 cm absorption feature of the ^{12}CO ring with the Galactic rotation curve, they concluded the location of this SNR to be near to the Galactic center. We can see the shell-like radio morphology with a radius of 12 arcmin in figure 7.1a (gray scale). Unlike the radio, X-ray emission shows the center-filled morphology. Thus this SNR is classified as a mixed-morphology SNR.

Bamba et al. (2000) analyzed the X-ray spectrum of G359.1-0.5 taken with ASCA (figure 7.1). It shows prominent Kα lines of Si and S. They argued that the line center of Si Kα line was consistent with that from He-like ions, whereas that of S was consistent from H-like ions. However, this is unusual since the heavier elements are generally less ionized compared to the lighter ones in the other typical SNRs. In the ASCA GIS spectrum, however, the H-like and He-like lines could not be separately detected because of its limited energy resolution. It is important to separate these lines and examine the ionization states.

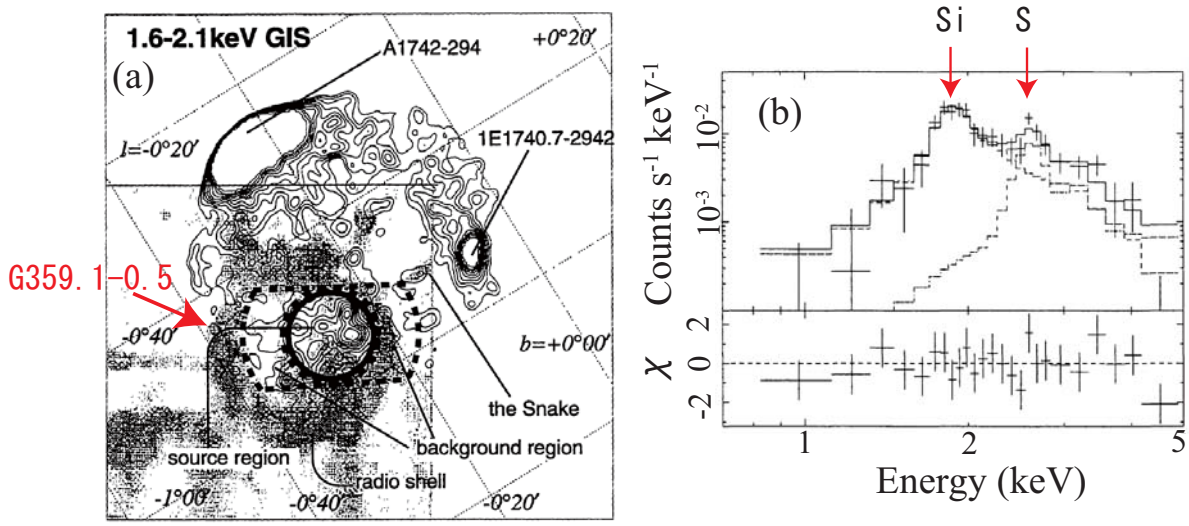

Fig. 7.1.—: (a) ASCA GIS contour map in the 1.6–2.1 keV band, superposed on the radio map (gray scale) by Gray (1994). The contour levels are linearly spaced and are saturated at A 1742-294 and 1E 1740.7-2942. (b) Background-subtracted ASCA GIS spectrum of G359.1-0.5. The plasma required two temperature components to describe prominent Kα lines of Si and S. These figures are taken from Bamba et al. (2000).

7.2 Suzaku Observation

We observed G359.1-0.5 with Suzaku (table 7.1). We used HESS J1745-303 data, a TeV unidentified source, as background. The X-ray emission from the HESS source has not been detected, and Bamba et al. (2009) derived a tight upper limit on the 2–10 keV emission as 2.1 $\times$ 10^{-13}erg s^{-1} cm^{-2}. Hence we can safely use the HESS observation for background.

Three of the XISs (two for FI and one for BI) were operated in the normal full-frame clocking mode with a SCI technique during all the observations. Data were cleaned using processing version 2.2.11.22. We used HEASOFT version 6.5.1 for data reduction and XSPEC version 11.3.2 for spectral analysis. After screening with the standard criteria, the net integration time is $\sim$60 ks for the source data and $\sim$70 ks for the background data.

Table 7.1—: Observation log of G359.1-0.5 and HESS J1745-303.

Target	Start Date	Obs.ID	R. A.	Dec.	Exposure
			(J2000.0)		(ks)
G359.1-0.5 *	2008-09-14	503012010	$17^{h}45^{m}12^{s}$	-29°45′12″	57.7
HESS J1745-303 **	2008-03-02	502016010	$17^{h}44^{m}54^{s}$	-30°06′35″	70.5

*Used as source data.**Used as background data.

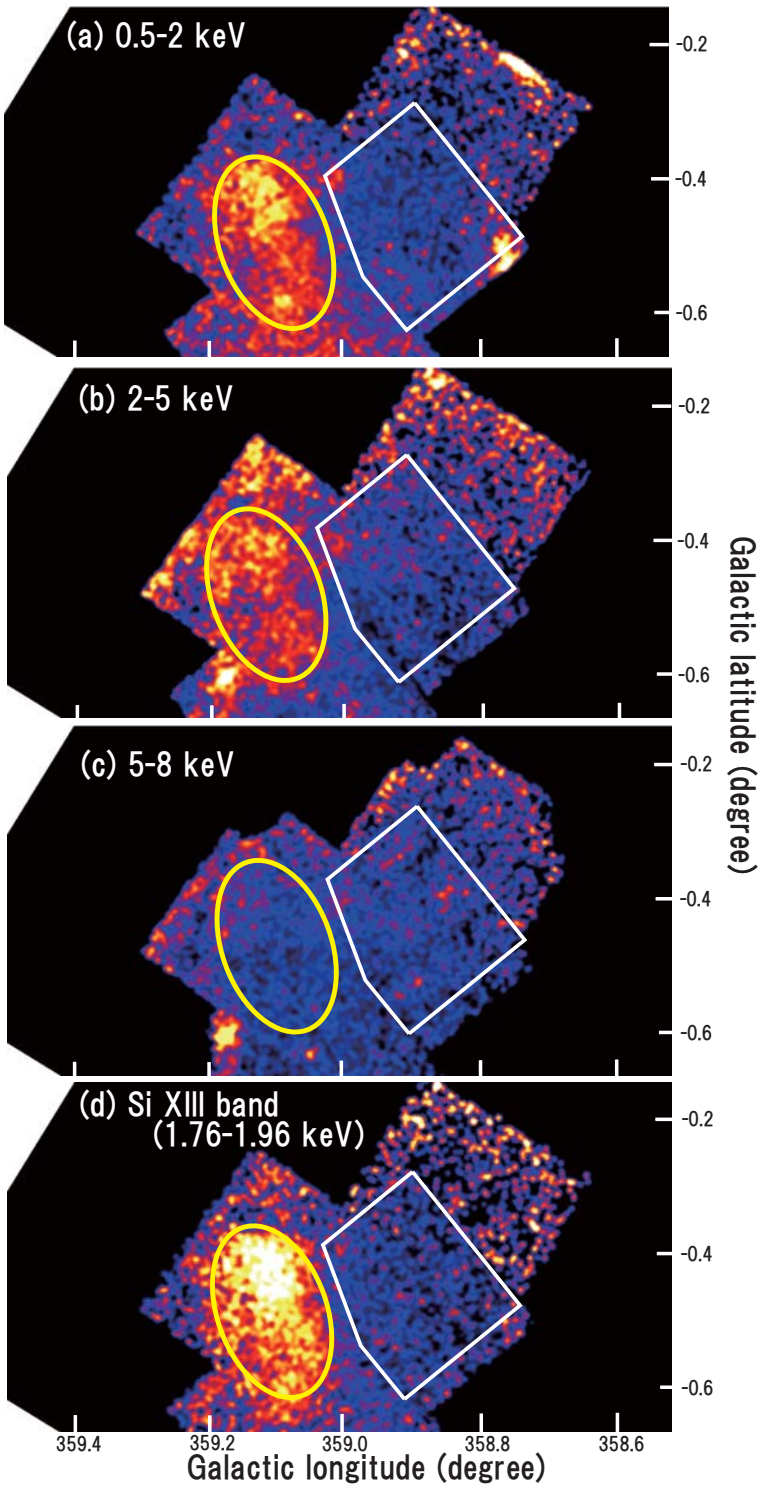

Fig. 7.2.—: Vignetting-corrected XIS image of G359.1-0.5 shown on a logarithmic intensity scale. Data from the three active XISs are combined. The yellow ellipse and white pentagon indicate the source and background regions, respectively.

7.3 Analysis and Results for Global Region

7.3.1 Overall Structure

Figure 7.2 shows the vignetting-corrected XIS image in several energy bands. The 1.76–1.96 keV band (figure 7.2d) corresponds to Kα emission of He-like Si. A strong Si Kα line is characteristic of SNR plasma. We can see a bright emission inside the yellow ellipse of figure 7.2d. We extracted a source spectrum from this region with radii of the major and minor axes of 4.9 and 7.9 arcmin, respectively. We excluded a background spectrum from the pentagonal region in figure 7.2. NXB spectra constructed with the `xisnxbgen` software were subtracted from both the source and background data. After correcting the vignetting and accumulation area, the source spectrum was made by subtracting the background spectrum. The spectra of the two FI sensors were merged to improve the statistics. In figure 7.3, we show the merged FI spectra. We can see several prominent lines of K-shell emission from He- and H-like ions of Mg, Si, and S from the source spectrum. Because G359.1-0.5 is located near the Galactic center, the emission is heavily contaminated by the Galactic center diffuse X-ray emission which is roughly expressed by the thin thermal plasma with $kT \sim 6$ keV and the neutral Fe line at $\sim$6.4 keV.

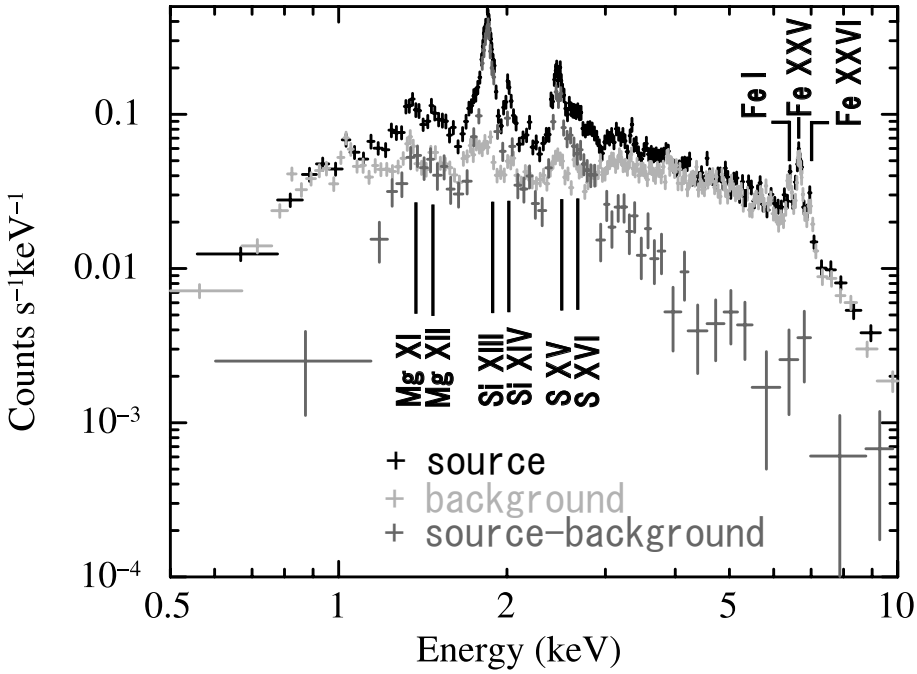

Fig. 7.3.—: XIS FI spectra of G359.1-0.5. We show the NXB-subtracted spectrum in the source region (black), NXB-subtracted and vignetting and accumulation corrected background spectrum (light gray), and background-subtracted source spectrum (dark gray). Note that, in the energy band below 1 keV and above 5 keV, the source emission is heavily contaminated by Galactic center diffuse X-ray emission. The energies of the prominent emission lines from specific elements are labeled.

7.3.2 Spectral Analysis

CIE Model Fitting

We here focus on 1-5 keV band, because the spectrum is heavily absorbed by the interstellar extinction below 1 keV and contaminated by Galactic center diffuse emission above 5 keV. We use only the FI data because the calibration for the FI is currently better around ∼2 keV.

We first fitted the spectrum with one VAPEC model. The Si and S abundances ($Z_{\rm Si}$ and $Z_{\rm S}$) were free parameters, while the Mg abundance ($Z_{\rm Mg}$) was fixed to the solar value. Figure 7.4a shows the fitting result with $kT_{\rm e}$ ∼0.8 keV. The model exhibited significant discrepancy around 2.7 keV, and was rejected with a large χ^2/dof of 382/96. We then tried a two-VAPEC model, assuming equal abundances between two components. Figure 7.4b shows the result with $kT_{\rm e}$ ∼0.5 keV and ∼2.6 keV. The large residual still remained with an unacceptable χ^2/dof of 224/94. Adding a further plasma component did not improve the fitting any more.

We checked the light curves of the source and background regions in the 2.5–3.0 keV band. They showed almost constant fluxes, hence no flare-like event had occurred during the observations. We detected the bump in all XIS sensors. Thus, the bump is a real structure.

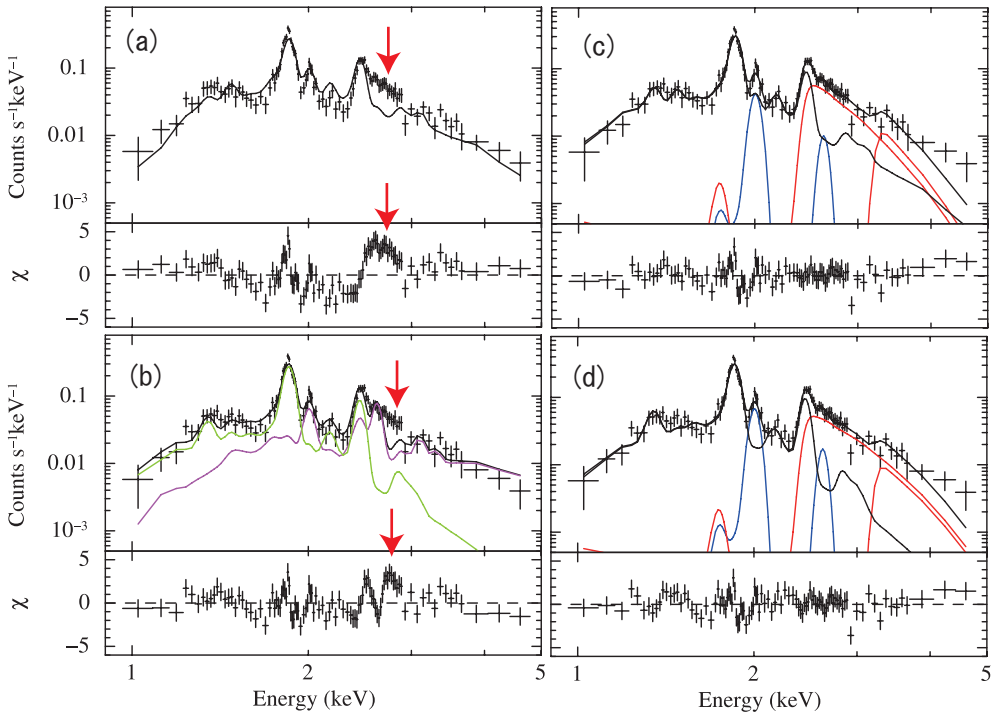

Fig. 7.4.—: XIS FI spectrum of G359.1-0.5 in the 1–5 keV band. (a) One- and (b) Two-VAPEC model fitting. The best-fit model is shown by solid lines. (c) Same as (a), but with He-RRC and Lyα lines of Si and S. (d) Same as (c), but the temperatures of the VAPEC and RRC components are linked.

Recombination Structures

There are no emission lines of abundant elements in the energy band of the bump. Furthermore, the bump is too broad to be explained by a single emission line. Instead, the edge of the bump (∼2.4 keV) corresponds to the electron binding energy of H-like Si, suggesting that this bump is likely due to RRC. Assuming this is suggestive of an overionized state, we introduced Si He-RRC and Lyα lines of Si and S in addition to the one-VAPEC model. A S He-RRC is also considered because a marginal bump is seen around 3.5 keV in figure 7.4a. During the analysis in this chapter, we ignore the contribution of the cascade lines because they are not significant due to poor statics. We assume that the RRC is expressed following equation 4.7. This formula gives a good approximation when $kT_{\rm e} \ll E_{\rm edge}$. In the case of G359.1-0.5, $kT_{\rm e}$ is ∼0.4 keV, as we confirm later, while $E_{\rm edge}$ of Si and S are ∼2–3 keV. Thus, we can safely adopt this formula.

The fitting result is given in figure 7.4c. With this model, χ^2/dof was greatly improved to 115/91. The temperature of the CIE component (0.55–0.63 keV) is higher than that of the recombination component (0.27–0.37 keV). As we see in the analysis of IC 443, however, the temperature of the CIE component becomes lower if we include the RRC of other lighter elements (such as Ne and Mg) or other ionization states (such as H-RRC). However, we cannot estimate these components with the statics of G359.1-0.5. Instead, we linked the temperatures of the CIE and RRC components. The resultant best-fit parameters and models are given in table 7.2 and figure 7.4d, respectively. With this model, χ^2/dof is 120/92, which is almost same with figure 7.4c. Because this model is acceptable with null hypothesis probability of 0.026, we use the result of table 7.2 in the following discussion.

Table 7.2—: Best-fit spectral parameters of G359.1-0.5.

CIE (VAPEC)	$kT_{\rm e}$ [keV]	$Z_{\rm Si}$ [solar]	$Z_{\rm S}$ [solar]	Normalization[a]
	0.38 (0.28–0.41)[b]	5.8 (4.9–10.8)[c]	11.0 (7.7–22.4)[c]	2.17 (1.78–2.58)
Line		Center energy [keV]	Line width [keV]	Normalization[d]
	Si Lyα	2.006 (fixed)	0 (fixed)	7.94 (5.19–10.4)
	S Lyα	2.623 (fixed)	0 (fixed)	1.36 (0.00–2.32)
RRC		Edge energy [keV]	$kT_{\rm e}$ [keV]	Normalization[d]
	Si He-RRC	2.439 (fixed)	0.38 (0.28–0.41)[b]	20.2 (18.0–24.7)
	S He-RRC	3.225 (fixed)	0.38 (0.28–0.41)[b]	2.15 (0.29–3.11)

The uncertainties in the parentheses are the 90% confidence range. [a]The unit is $10^{-12} \int n_e n_{\rm H}\, dV/(4\pi D^2)$ (cm^{-5}), where n_e, $n_{\rm H}$, V, and D are the electron and hydrogen densities (cm^{-3}), emitting volume (cm^3), and distance to the source (cm), respectively. [b]We assumed the same $kT_{\rm e}$. [c]These values should be modified in the overionization case (section 7.3.4). [d]The unit is 10^{-5} cm^{-2} s^{-1}.

7.3.3 Electron and Ionization Temperatures

We successfully detected He-RRC of Si and S from G359.1-0.5, for the first time. Due to the limited energy resolution and photon statistics of ASCA, the Si He-RRC was misunderstood as H-like S Kα line and the existence of high-temperature ($\sim$4 keV) S-rich plasma was claimed (Bamba et al. 2000). Here, we mention the plasma temperature.

The electron temperature determined by the bremsstrahlung continuum shape and the RRC width is $\sim$0.4 keV. Using this value, we derive the ionization temperature. From the best-fit model in table 7.2, the flux ratios of Lyα/Heα and He-RRC/Heα of Si are given as 0.15 (0.10–0.20) and 0.38 (0.34–0.46), while those of S are 0.13 ($\leq$0.23) and 0.20 (0.03–0.30), respectively. In figure 7.5, we compare these values with the modeled emissivity ratios at $kT_{\rm e}$ = 0.4 keV (Masai 1994) . We obtain kT_z = 0.79 (0.68–0.86) keV, 1.13 ($\geq$1.00) keV for Si, and 1.3 ($\leq$1.6) keV and 0.77 (0.51–0.92) keV for S using the above ratios, respectively. All these ionization temperatures are consistent with $\sim$0.8 keV [1]. The result that the kT_z $\sim$0.8 (0.7-0.9) keV is significantly higher than $kT_{\rm e}$ $\sim$0.4 (0.3-0.4) keV indicates the plasma is in a highly overionized state.

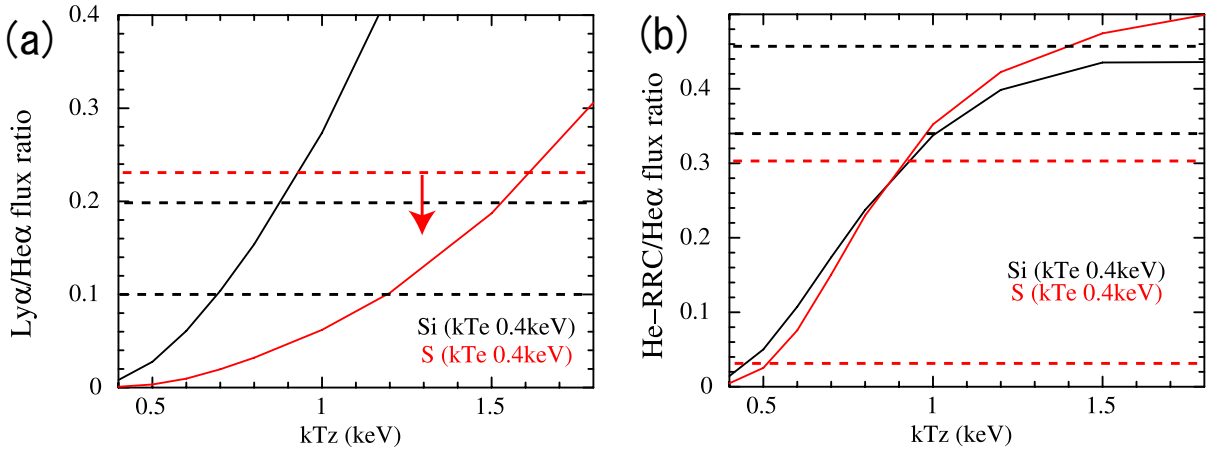

Fig. 7.5.—: Predicted emissivity ratios of (a) Lyα/Heα and (b) He-RRC/Heα for Si and S as a function of the ionization temperature for electron temperature of 0.4 keV (Masai 1994). The horizontal dashed lines represent 90% errors of the observed values.

[1]Only Si He-RRC/Heα indicates high kT_z ($\geq$1.0 keV). This would be due to the significant contribution of Si H-RRC. In the case of kT_z = 0.8 keV for the Si plasma, an ion fraction of fully-ionized ions is about 1/6 of that of H-like ones (figure 4.6). Because the recombination cross section for the fully-ionized ions into the ground state is about twice as large as that for H-like ions, we estimate the reasonable flux portion of H-RRC is about $\sim$1/3 of the He-RRC. If we assume that the real Si He-RRC flux is $\sim$2/3 of that in figure 7.5b, it is consistent with kT_z $\sim$0.8 keV.

7.3.4 Abundance Correction for Overionization

We make possible modifications for the abundance in the case of overionization using an available APEC code. In the kT range of 0.4–0.8 keV, most Heα emission originates from the He-like ions. Hence, the emissivities of the He-like ions for Si and S are modified by multiplying the ion-fraction ratio between kT_z = 0.8 keV and 0.4 keV. The Heα intensity is proportional to $Z \times \epsilon(kT_{\rm e}, kT_z)$, where Z and $\epsilon(kT_{\rm e}, kT_z)$ are the abundance of the element (solar) and the total emissivity for the Heα for $kT_{\rm e}$ and kT_z (cm^{3}s^{-1}), respectively. Multiplying by ϵ(0.4 keV, 0.4 keV)/ϵ(0.4 keV, 0.8 keV), we obtain the real abundances in the overionized state as $Z_{\rm Si} \sim 5.8\times(0.94/0.60)\sim$9.1 solar and $Z_{\rm S} \sim 11.0 \times (0.85/0.86) \sim$11.0 solar. We should note that these values become lower if we consider the cascade lines which occupy significant fraction of the Heα emission[2].

7.3.5 Volume Emission Measure

The VEM of the VAPEC component is derived from table 7.2 as $\sim$2.2 $\times 10^{12}$ cm^{-5}. On the other hand, the VEM of the recombination component is derived from equation 4.7. The total radiative recombination rate of He-like Si at $kT_{\rm e}$ = 0.4 keV is $\sim$2.1 $\times 10^{-12}$ cm^{3}s^{-1}. The recombination rate into the ground state of the H-like ions is derived from equation 4.10 for the He-like Si as $\sigma_1/(\sigma_1+\sigma_2+\cdots) \sim 0.45$. The value of $n_{\rm Si}/n_{\rm H}$ is calculated using $Z_{\rm Si}$ in the previous subsection. Using the observed He-RRC flux in table 7.2 and $\kappa_{\rm H-like}$(0.8 keV) $\sim$ 0.33, we obtain ${\rm VEM}_{\rm RRC(Si)} \sim 2.0 \times 10^{12}$ cm^{-5}. In the same way for S, using $\alpha_1 \sim$3.1 $\times 10^{-12}$ cm^{3}s^{-1}, $\sigma_1/(\sigma_1+\sigma_2+\cdots) \sim 0.44$, and $\kappa_{\rm H-like}$(0.8 keV) $\sim$ 0.09, we obtain ${\rm VEM}_{\rm RRC(S)} \sim 1.0 \times 10^{12}$ cm^{-5}. These consistent results support the same origin of the bremsstrahlung and recombining components.

7.4 Summary

- The Suzaku spectrum exhibits unusual bump-like residuals around 2.7 keV when fitted by the CIE plasma model. This bump is well explained by the RRC of Si. This is the third examples of the recombination-dominant SNR following after W49B and IC 443.
- The electron temperature derived from the bremsstrahlung and RRC shapes is $\sim$0.4 keV. On the other hand, the ionization temperatures derived from the observed intensity ratios of RRC/Heα and Lyα/Heα for Si and S are consistent with $\sim$0.8 keV. This indicated the the plasma of G359.1-0.5 is in a highly overionized state.
- VEMs independently determined from the fluxes of the bremsstrahlung and recombination components are consistent with each other. This supports the common origin of these components.

[2]If we estimate from the observed He-RRC flux and equation 4.10, about half of the total Heα emission for Si and S originate from the cascade process.

Chapter 8

Discussion on Recombination-dominant SNRs

In the previous chapters, we have analyzed X-ray data of three SNRs (W49B, IC 443, and G359.1-0.5) obtained with Suzaku. The superior sensitivity and the energy resolution of Suzaku XIS enable us to discover the brand-new spectral structure; the strong RRC in SNRs. We have found the Fe He-RRC from W49B, Si and S H-RRC from IC 443, and Si and S He-RRC from G359.1-0.5. In particular, we have further discovered cascade line structures from W49B.

All these SNRs exhibit the equal electron temperatures and volume emission measures for the bremsstrahlung and RRC components. This fact robustly indicates that the X-ray emission is due to a single overionized plasma, or a recombining plasma. Thus, we find a new aspect of the SNR evolution, presence of a strong recombining plasma, for the first time. In this chapter, we investigate the characteristics of the recombination-dominant (hereafter RD) SNRs by comparing with a well-known ionization-dominant (ID) SNR and discuss the origin of the strong recombining plasma.

8.1 Spectral Features

In order to clarify the characteristics of the RD SNR [1], we compare them with a typical ID SNR (Tycho's SNR [2], hereafter Tycho for short). The Suzaku observation of Tycho is summarized in appendix A.

[1] Here we focus on W49B, which exhibit the most prominent structure of recombination X-rays.

[2] In AD 1572, the astronomer Tycho Brahe observed a bright supernova in detail. It is now firmly classified as a Type Ia SNR based on the optical spectrum from a scattered-light echo (Krause et al. 2008).

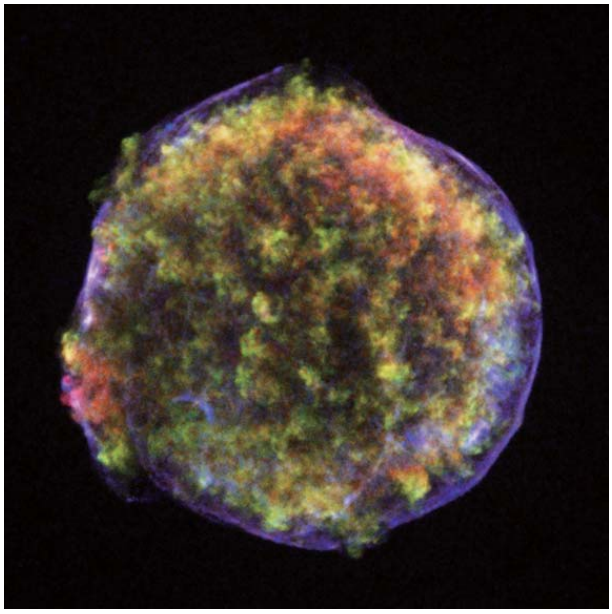

Fig. 8.1.—: Chandra three-color composite image of Tycho (Warren et al. 2005). (Blue) 4.1-6.1 keV band. Mainly originates from a non-thermal component. (Red) 0.95-1.26 keV. Mainly emitted by Fe ions. (Green) 1.63-2.26 keV. Mainly emitted by Si ions.

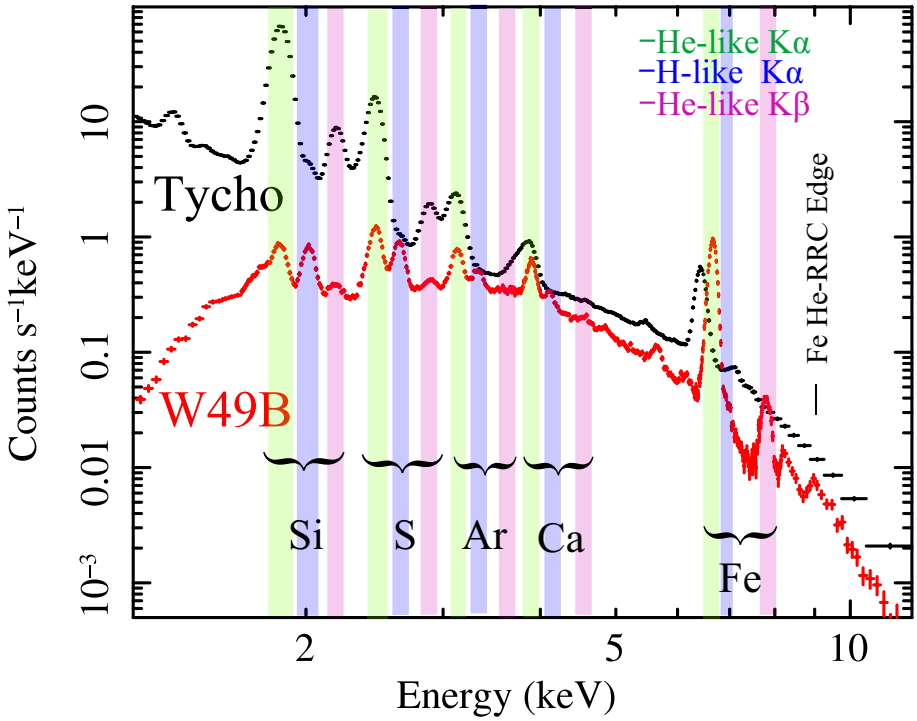

Fig. 8.2.—: Background subtracted Suzaku XIS FI spectra of Tycho (black) and W49B (red) taken from the whole remnant region. The energies of the prominent Kα emission lines are labeled. We show He-like Kα lines in green, He-like Kβ in purple, and H-like Kα in blue. We also show the edge energy of the Fe He-RRC.

Tycho is one of the youngest (∼440 years) and X-ray brightest SNRs in our Galaxy. As is seen in figure 8.1, it exhibits nearly spherically-symmetric shape. The X-ray spectrum shows intense emission lines which were studied in detail with the previous satellites. Using Tenma[3] data, Tsunemi et al. (1986) showed that Kα center energies of Si, S, Ar, Ca, and Fe are consistent with those of underionized states, which is revealed for the first time in SNRs. Thus, this source is a typical ID SNR in a strongly underionized state.

In figure 8.2, we show the Suzaku spectra of Tycho and W49B. Both exhibit intense line emission, but there are significant differences. For the quantitative comparison of the spectral structures, we construct a semi-phenomenological model, which is composed of a bremsstrahlung, Gaussian function lines, and an RRC. We focus on the W49B and Tycho spectra in the energy band of 5–12 keV, where emission structures mainly originate from Fe. We simply assume that the relevant RRC is a Fe He-RRC.

For the emission lines of Tycho, we treat Fe Kα, Kβ, Cr Kα, and Ni Kα. Line centroids are free parameters [4]. We also include Fe Lyα with fixed line center in order to derive the flux upper limit. Because heavy elements in Tycho are Doppler-shifted (Furuzawa et al. 2009), we treat the line widths as free parameters. All these widths are linked each other for simplicity.

As for the emission lines of W49B, Fe Heα, Heβ, Heγ-∞, Lyα, and Kα lines of Cr, Mn, and Ni are included. We fix the center energies of Cr Kα, Mn Kα, and Fe Lyα to those in table 5.1, and Heβ to the expected value for $kT_z = 2.7$ keV [5]. The center energies of the other lines are free parameters. Since Fe Heα and Heγ-∞ include many emission lines from different ionization states and energy levels, we treat the widths of these lines as free parameters. Widths of the other lines are fixed to 0.

Using this semi-phenomenological model, we can independently determine the electron temperatures with three independent methods; the bremsstrahlung shape, line flux ratios, and the width of RRC [6]. We, however, link the temperatures of bremsstrahlung and RRC components for Tycho because we see no significant excess of the RRC structure.

We first fit the spectra with a model of bremsstrahlung plus Gaussian lines. Figure 8.3a shows the best-fit results. We can see clear saw-edged bump structure around 9 keV for W49B with χ^2/dof = 850/133, while no sign for Tycho with χ^2/dof = 144/58 [7].

We then add an Fe He-RRC. The best-fit results are summarized in figure 8.3b and table 8.1. For W49B, χ^2/dof is greatly improved to 270/131, while χ^2/dof = 89/57 for Tycho is not so large but significant. The significant improvement of the Tycho spectrum would be due to artificial compensation of the non-thermal contribution by the RRC.

[3]This is the Japanese second X-ray satellite, launched in 1983.

[4]We only fix the centroid of Ni Kα to the predicted value of neutral line because it is weak.

[5]This ionization temperature is derived in chapter 5.

[6]See section 4.3 for details.

[7]We can see a rising slope above 7.5 keV in the lower panel (residual) of Tycho (right) in figure 8.3a. This would be due to the non-thermal contribution as we briefly discuss later.

In the spectrum of W49B, a large residual around Fe Heα are found. This is partially due to the response uncertainty as we noted in chapter 5. However, the main reason is due to the single Gaussian line approximation for the composite of many lines in different ionization states. In fact, if we ignore 6.4–6.9 keV, we obtain an acceptable χ^2/dof = 113/98.

The electron temperatures of W49B derived in the three different methods are; $\sim$1.7 (1.6–1.7) keV from the bremsstrahlung shape, $\sim$1.8 (1.6–1.9) keV from the flux ratios of Fe Heβ/Heα [8], and $\sim$1.3 (1.2–1.6) keV from the RRC width. These results are consistent with each other, and hence no additional component such as non-thermal emission is required. In the previous APEC model analysis (chapter 5), we implicitly assumed that the temperatures of the bremsstrahlung and that from the Kβ/Kα flux ratio are the same. Here we confirm the validity of this assumption.

The Fe Kβ/Kα flux ratio of Tycho can be converted to $kT_{\rm e}$ $\sim$1.8 (1.6–2.0) keV [9]. On the other hand, the bremsstrahlung shape indicates that $kT_{\rm e}$ is $\sim$4.5 (4.4-4.5) keV. We regard that this inconsistency is possibly due to the non-thermal contribution. In fact, Tamagawa et al. (2009) reported the existence of non-thermal emission of Tycho using the wideband spectra of the Suzaku XIS and HXD. They detected X-ray emission up to 30 keV with a power-law index of 2.69, and concluded that the emission comes from synchrotron radiation. We should emphasize that our semi-phenomenological model can in principle separate the non-thermal components, by fixing the electron temperature of the bremsstrahlung to that from the Fe Kβ/Kα line intensity ratio. However, further details of the non-thermal component in Tycho is beyond the scope of this thesis.

[8] We used figure 4.10.

[9] We derive this value using figure 4.10. We also confirm this from the same semi-phenomenological model fitting in the 1.7–5 keV band. The electron temperatures derived from the Kβ/Kα flux ratios of Si and S indicate $\sim$2.4 keV and $\sim$1.9 keV, respectively. All the Kβ/Kα ratios indicate the electron temperature is around 2 keV.

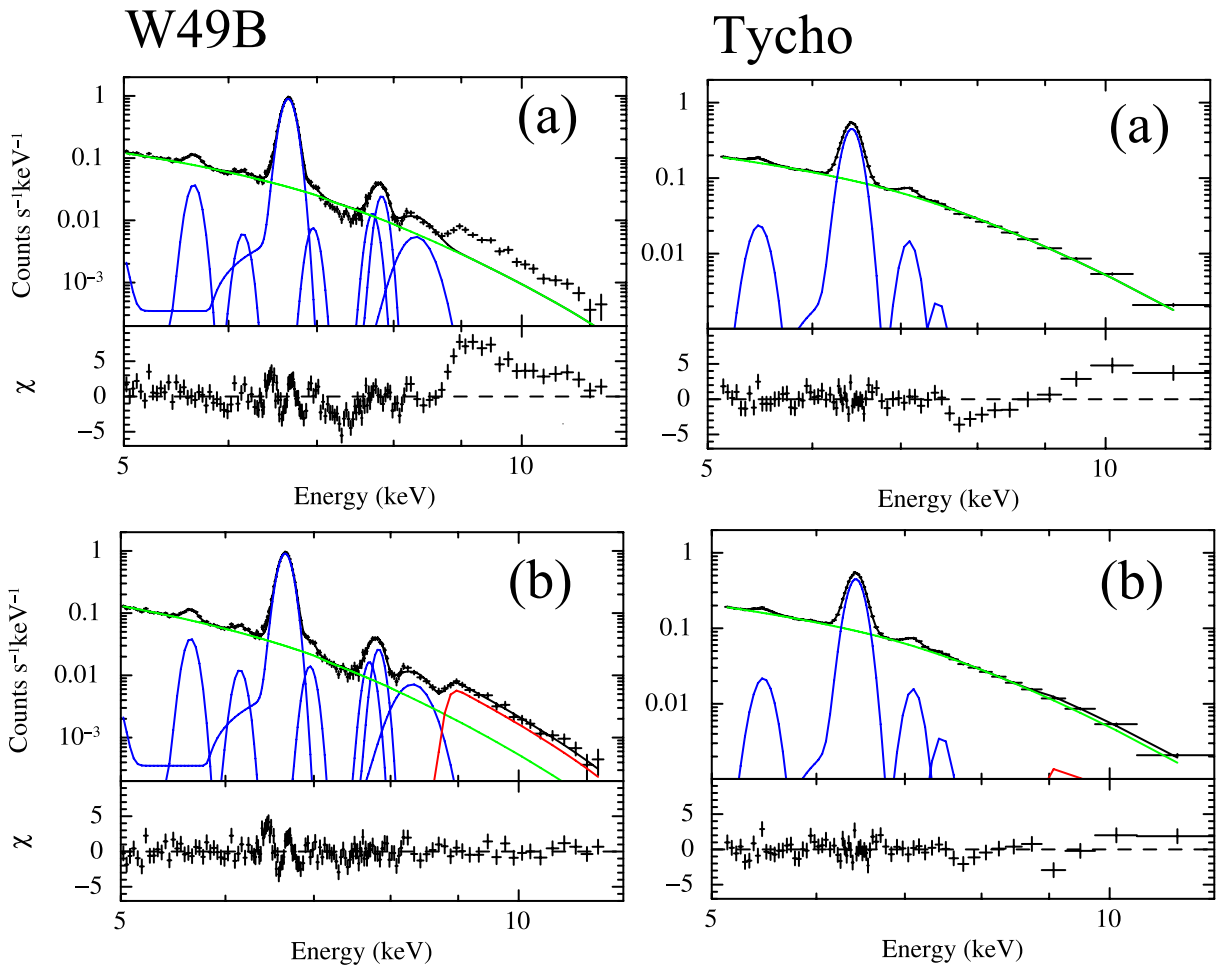

Fig. 8.3.—: Semi-phenomenological model fittings of W49B (left) and Tycho (right) spectra. (a) XIS FI spectrum fitted with a bremsstrahlung continuum and lines. We can see a large bump above 9 keV in W49B. A rising slope above 7.5 keV in the lower panel (residual) of Tycho is likely due to the non-thermal contribution (see text). (b) Same spectrum as (a), but with the radiative recombination continuum of Fe.

Table 8.1—: Best-fit spectral parameters in figure 8.3.

W49B				
bremsstrahlung			$kT_{\rm e}$ [keV]	Normalization[a]
			1.67 (1.66-1.68)	2.98 (2.93-3.01)
RRC	Fe He-RRC	Edge energy [keV]	$kT_{\rm e}$ [keV]	Normalization[b]
		8.830 (fixed)	1.32 (1.19-1.60)	11.6 (10.8-12.6)
lines		Center energy [keV]	Width [keV]	Normalization[b]
	Cr Kα	5.655 (fixed[c])	0 (fixed)	2.89 (2.61-3.15)
	Mn Kα	6.162 (fixed[c])	0 (fixed)	0.99 (0.77-1.20)
	Fe Heα	6.667 (6.666-6.667)	0.36 (0.35-0.38)	91.2 (90.4-92.0)
	Fe Lyα	6.961 (fixed[c])	0 (fixed)	1.37 (1.17-1.56)
	Ni Kα	7.722 (7.712-7.733)	0 (fixed)	2.29 (2.05-2.52)
	Fe Heβ	7.845 (fixed[d])	0 (fixed)	3.92 (3.60-4.18)
	Fe Heγ-∞	8.347 (8.323-8.374)	0.22 (0.19-0.25)	4.14 (3.75-4.51)
Tycho				
bremsstrahlung			$kT_{\rm e}$ [keV]	Normalization[a]
			4.48 (4.45-4.52)[e]	1.00 (1.00-1.01)
RRC	Fe He-RRC	Edge energy [keV]	$kT_{\rm e}$ [keV]	Normalization[b]
		8.830 (fixed)	4.48 (4.45-4.52)[e]	1.20 (0.99-1.40)
lines		Center energy [keV]	Width [keV]	Normalization[h]
	Cr Kα	5.471 (5.462-5.483)	0.060 (0.058-0.061)[h]	2.79 (2.56-3.11)
	Fe Kα	6.432 (6.431-6.432)	0.060 (0.058-0.061)[h]	66.8 (66.3-67.2)
	Fe Lyα	6.966 (fixed[f])	0.060 (0.058-0.061)[h]	0.09 (0.00-0.36)
	Fe Kβ	7.106 (7.096-7.123)	0.060 (0.058-0.061)[h]	2.93 (2.66-3.20)
	Ni Kα	7.470 (fixed[g])	0.060 (0.058-0.061)[h]	0.82 (0.55-1.09)

Note. — The uncertainties in the parentheses are the 90% confidence range. [a]The unit is $10^{-13}\int n_e n_{\rm H}\, dV/(4\pi D^2)$ (cm^{-5}), where n_e, $n_{\rm H}$, V, and D are the electron and hydrogen densities (cm^{-3}), emitting volume (cm^3), and distance to the source (cm), respectively. [b]The unit is 10^{-5} cm^{-2} s^{-1}. [c]Fixed to the value in table 5.2. [d]Fixed to the ideal value at $kT_z = 2.7$ keV. [e]Linked each other. [f]Fixed to the ideal value. [f]Fixed to the ideal value of neutral Ni. [h]Linked each other.

The semi-phenomenological model fitting have clearly revealed the spectral features of the newfound RD SNR as below.

1. Strong recombination structures (RRC and cascade lines).
2. Strong Lyα line.
3. High line center energy for Heα. [10].

1) Remarkable fact is that the electron temperatures of W49B and Tycho are nearly the same ($\sim$1.6-1.8 keV) [11]. Nevertheless, there are significant spectral differences; W49B has a very strong recombination structure above 8 keV, while no sign in Tycho. Thus, the two types of SNRs, the RD and ID SNRs, are clearly distinguished from the presence of the strong recombination structure.

2) We can see intense Lyα emission in the W49B spectrum from Si, S, Ar, Ca, and even Fe (figure 8.2). On the contrary, we can hardly see them in the Tycho spectrum. The Fe Lyα/Heα flux ratio is 0.015 (0.013-0.017) for W49B, while only an upper limit (0.0054) is derived for Tycho. The high Lyα/Heα flux ratio indicates high ionization temperature. In fact, kT_z derived from this ratio is $\sim$2.6 (2.4-2.7) keV for W49B, while $\leq$0.85 keV for Tycho.

Table 8.2—: Observed Kα line center energies (eV).

	W49B	IC 443	Tycho
Cr	5655 (5646-5663)	5575 (5438-5697)	5471 (5462-5483)
Mn	6162 (6142-6183)	not detected	5950 (5900-6000) *
Fe	6667 (6666-6667)	6676 (6656–6696)	6432 (6431-6432)
Ni	7722 (7712-7733)	not detected	7470 (fixed to the neutral value)

* From Tamagawa et al. (2009).

[10]Note that we here use the word "Heα" as the mixture of the lines from He-, Li-, Be-like and lower ionized ions.

[11]The Fe Kβ/Kα flux ratio is 0.043 (0.040-0.046) for W49B, while 0.044 (0.040-0.048) for Tycho. This consistent result strongly suggests the electron temperature for both SNRs are nearly the same.

3) In table 8.2, we summarize the observed Heα [12] center energies of Cr, Mn, Fe, and Ni for W49B, IC 443, and Tycho [13]. All the centroids of Tycho is significantly lower than those of IC 443 and W49B. The high line centroids for the RD SNRs indicate the highly-ionized state of the plasma.

Note that we find a marginal Kα sign of Cr and robust one of Fe from IC 443 for the first time (figure 8.4). We fit the spectrum of IC 443 in the energy band of 5.0-7.5 keV with a power-law and two Gaussian functions. The best-fit fluxes are 1.7 (0.0–4.1) $\times 10^{-6}$ photons cm^{-2}s^{-1} for Cr and 1.46 (1.17–1.77) $\times 10^{-5}$ photons cm^{-2}s^{-1} for Fe. Although the Cr emission is marginal, χ^2/dof is improved from 36.4/74 to 34.8/72 by introducing the Cr Kα line.

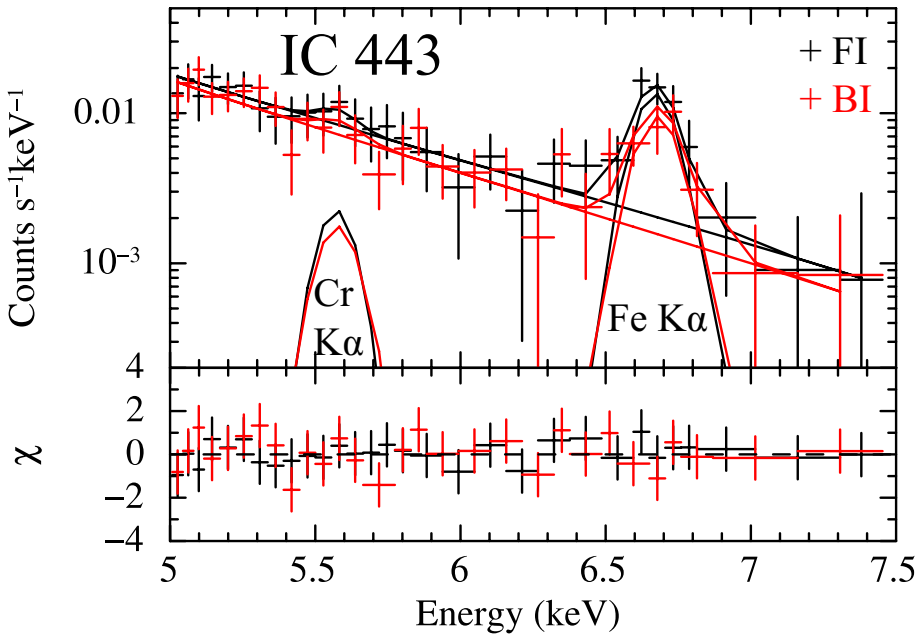

Fig. 8.4.—: NXB subtracted XIS FI and BI spectra of IC 443 extracted from the circular region in figure 6.3. We fit the spectra with a power-law and two Gaussians which represent Cr and Fe Kα lines.

[12] As we see later, the line centroids of the Tycho spectrum clearly indicate the underionized state than those from He-like ions. However, here we describe the Kα lines as Heα for convenience.

[13] As for G359.1-0.5, these lines are not detected because the plasma temperature is relatively low and the source emission is highly contaminated by the Galactic center X-ray emission.

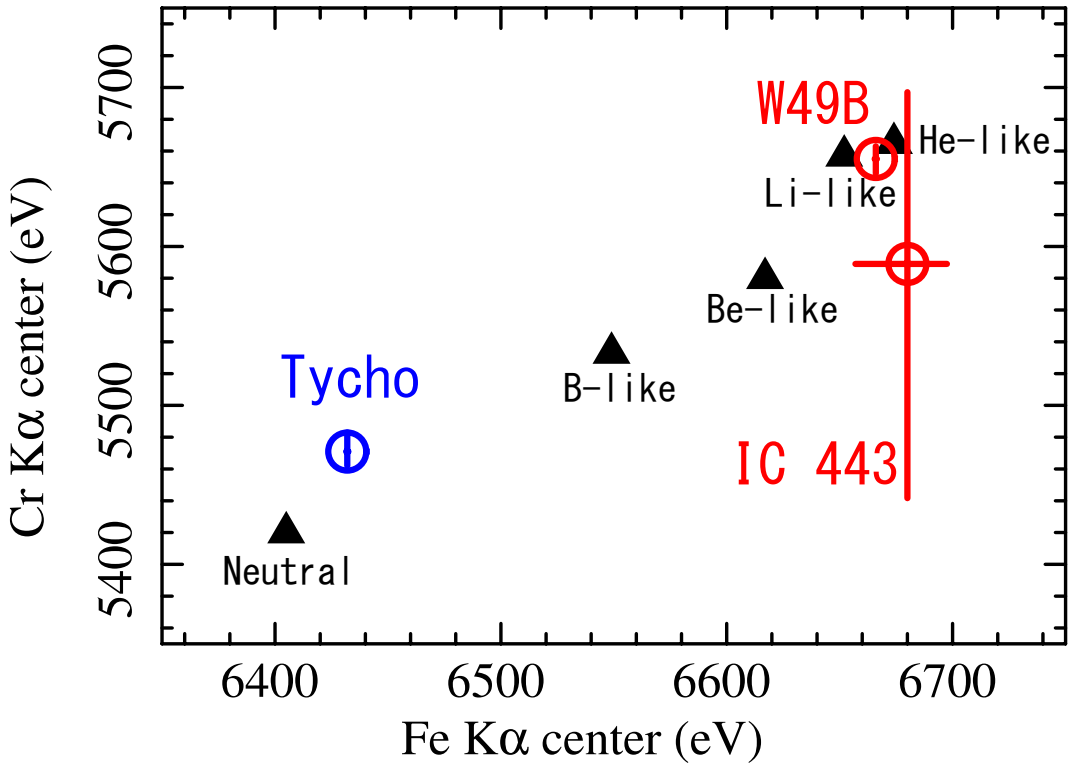

Fig. 8.5.—: Weighted line center energies of Fe and Cr Kα lines for the observed recombination-dominant SNRs (W49B and IC 443) and ionization-dominant SNR (Tycho). We also show the theoretical center energies of in different ionization states with triangles. (Mewe et al. 1985, Yang et al. 2009, http://www.camdb.ac.cn/e/spectra/spectra_ search.asp)

In figure 8.5, we plot the Kα centroids of Fe and Cr for these SNRs. We also show the theoretical center energies of these lines in different ionization states. In the case of W49B and IC 443, the line centroids indicate that the Fe ions are ionized into nearly He-like. In the case of Tycho, on the contrary, centroids are significantly lower than those from B-like. Thus, high centroids of these Heα lines, which indicate the presence of highly-ionized atoms, are characteristic of the RD plasma.

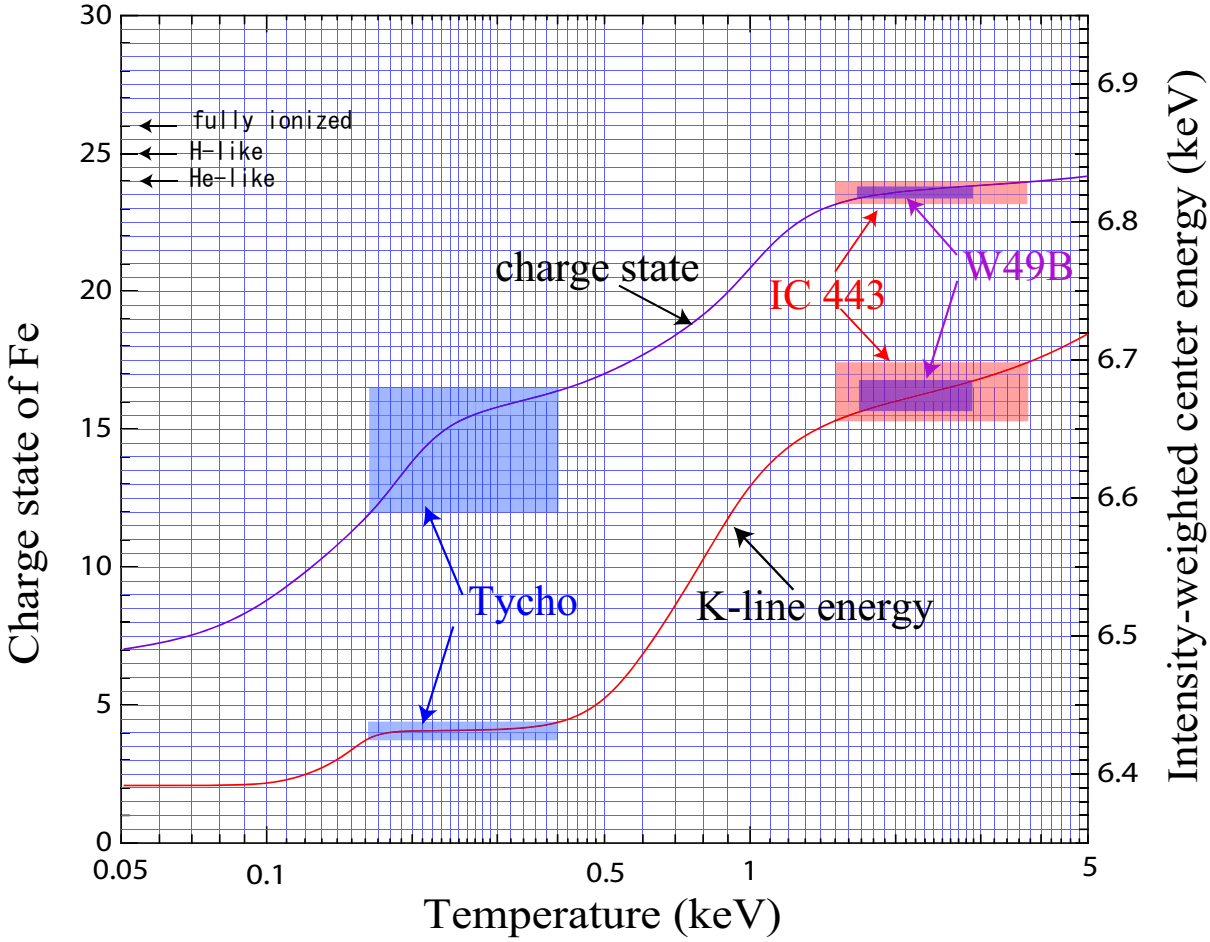

Fig. 8.6.—: Average ionization state and K-line energy of Fe as a function of CIE plasma temperature. The K-line enrgy is intensity-weighted for the lines including satellites. We also show the observed Fe Kα center energy of W49B, IC 443 and Tycho. Here we derive kT_z from the observed intensity-weighted centroid. Using this temperature, we estimate that major ionization states of Fe are Si- to F-like for Tycho, while Li- to He-like for IC 443 and W49B. We calculated the Kα centroid for W49B by taking the weighted center between Heα and Lyα. This figure is taken from Masai et al. (2002).

Although the line center is a function of both $kT_{\rm e}$ and kT_z, it mainly reflects the ion fraction (i.e. kT_z). Hence we can roughly estimate kT_z from the intensity-weighted center energy assuming the CIE state. The result is shown in figure 8.6. We assume the systematic uncertainty of energy scale is 0.1 % following Ozawa et al. (2009b). From the observed center energy, we can derive kT_z of Fe ions as 0.16–0.40 keV for Tycho, 1.5–3.8 keV for IC 443, and 1.7–2.9 keV for W49B. This value is consistent with that derived from RRC/Heα or Lyα/Heα flux ratios for W49B.

8.2 Characteristics

We summarize the electron temperature, age, distance, radius, and X-ray morphology of the three RD SNRs (W49B, IC 443 and G359.1-0.5) and ID SNR (Tycho) in table 8.3. It should be noted that all the RD SNRs show the awkward and center-filled morphology in X-rays (mixed-morphology SNRs). We should also note the high-energy gamma-rays are detected from W49B (GeV gamma-rays by Fermi) and IC 443 (GeV by EGRET, AGILE, & Fermi and TeV by MAGIC and VERITAS: Esposite et al. 1996; Tavani et al. 2009; Albert et al. 2007; Acciali et al. 2009). Also, TeV gamma-rays are detected by HESS near G359.1-0.5 (Aharonian et al. 2006). We also mention the OH maser is detected from G359.1-0.5 (Yusef-Zadeh et al. 1996) and IC 443 (Hewitt et al. 2006). Yusef-Zadeh et al. (2003) showed there is a strong association between mixed-morphology SNRs and maser-emitting SNRs. Hewitt et al. (2009) show the correlation between maser-emitting SNRs and a class of GeV- to TeV-energy gamma-ray sources. There might be relations between the mixed-morphology, maser-emitting, high-energy accelerator, and RD SNRs.

Table 8.3—: Characteristics of the observed SNRs.

SNR	kT_e[a] (keV)	age (year)	D [b] (kpc)	R [c] (pc)	X-ray morphology
W49B	1.5	not known	11.4	8.3	elongated, center-filled
IC 443	0.7	3000[d], 4000[e]	1.5	11	elongated, center-filled
G359.1-0.5	0.4	not known	8.5	20	elongated, center-filled
Tycho	1.8	∼440	2.8	3.3	almost spherical, shell-like

[a]Derived from our analyses using the Suzaku data. [b]Distance to the source. References are Gwinn et al. (1992) for W49B, Welsh & Sallmen et al. (2003) for IC 443, Uchida, Morris, & Yusef-Zadeh (1992) for G359.1-0.5, and Ruiz-Lapuente (2004) for Tycho. The distance are under debate for some of these SNRs. For example, the uncertainty is 8–12 kpc for W49B and 2-4 kpc for Tycho. Note that the physical parameters in table 8.4 are function of the distance, hence there is significant uncertainty on the resultant values. [c]Radius of the source. We assumed the distance in this table, and major axes of 2.5, 25, 7.9, and 4.0 arcmin for W49B, IC 443, G359.1-0.5, and Tycho, respectively. [d]Petre et al. (1988). [e]Troja et al. (2008).

Table 8.4—: Physical parameters of the observed SNRs.

SNR	dominant process	density (cm^{-3})	thermal energy* (10^{50} ergs)	mass* ($M_\odot$)
W49B	recombination	1.9	9.6	110
IC 443	recombination	1.0	0.15**	3.7**
G359.1-0.5	recombination	0.23	1.6	68
Tycho** *	ionization	2.3	0.52	5.0

*Note that if we consider the filling factor f, it is multiplied by $1/\sqrt{f}$ for density, and $\sqrt{f}$ for energy and mass. We assume a sphere with radii of 2.5, 7.5, 4.0 arcmin for W49B, IC 443, and Tycho, respectively, and an ellipsoidal shape with radii of 7.9, 4.9, and 4.9 arcmin for G359.1-0.5. **Note that our estimation is based on the result from a part of the SNR. The energy and mass are expected to be dozens of times larger for the whole remnant. ***We use the result of NEI (thin thermal underionized plasma code) fitting for Tycho.

We then derive the physical parameters of the plasma in table 8.4, assuming the distance in table 8.3. Because the observed flux of the thermal component (VAPEC) is proportional to $(1/4\pi D^2)\int n_{\rm H} n_{\rm e} dV$, we can derive the density of the plasma (n) assuming the hydrogen density ($n_{\rm H}$) and electron density ($n_{\rm e}$) are equal ($n_{\rm H} \simeq n_{\rm e} \simeq n$) in a hydrogen-dominant and uniform density plasma. The total energy of the plasma is obtained using the equation; $E = 3kT/2 \times (n_{\rm H} + n_{\rm e}) \times V \simeq 3kTnV$. The total mass of the plasma is estimated by the equation $M = nVm_{\rm H}$, where $m_{\rm H}$ is the hydrogen mass. Note that we cannot cover the whole remnant for IC 443, hence the total energy and mass would be dozens of times larger. We should note that the estimated mass is sub-solar for Tycho, while several tens of solar for the RD SNRs. Because of the high metallicity for W49B (∼3 solar), IC 443 (∼2 solar), and G359.1-0.5 ($\lesssim$10 solar), we can safely assume most of the plasma originate from the ejecta. Hence, the plausible progenitors of the RD SNRs are massive stars.

In figure 8.7, we show the electron and ionization temperatures for the observed SNRs. We also show the ASCA results from Kawasaki et al. (2005). We should note that the electron temperatures of W49B and IC 443 are significantly lower than the ASCA results. This is because we take the RRC contribution into account.

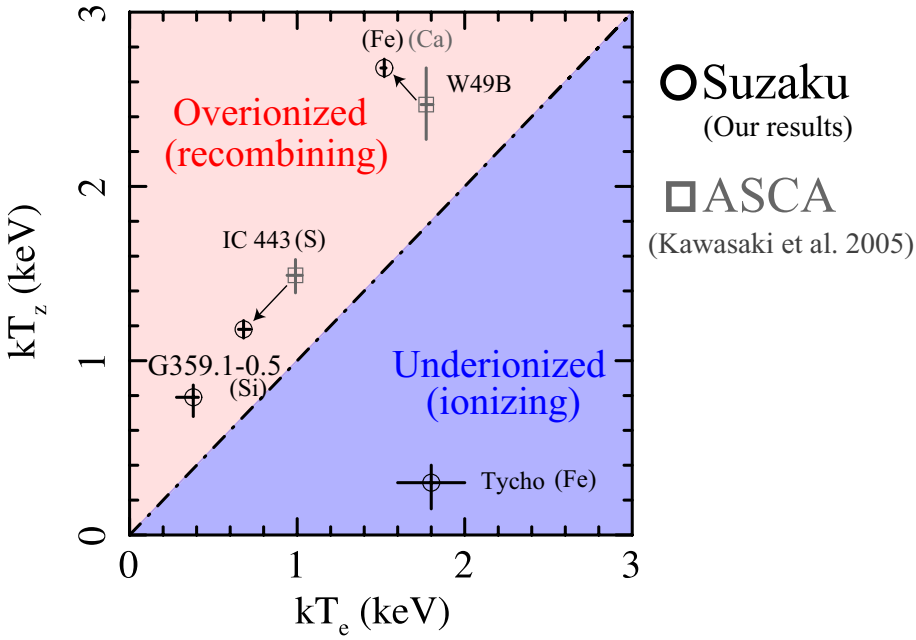

Fig. 8.7.—: Electron and ionization temperatures of the SNRs observed with Suzaku (black circle). Gray points indicate ASCA results. We derived $kT_{\rm e}$ from the bremsstrahlung shape for W49B, IC 443, and G359.1-0.5, and from the Fe Kβ/Kα flux ratio for Tycho. We obtained kT_z from the RRC/Heα ratio for W49B and IC 443, Lyα/Heα ratio for G359.1-0.5, and Kα line center for Tycho. Parentheses indicate the element from which we derive kT_z. We should note that $kT_{\rm e}$ of W49B and IC 443 become lower by taking RRC into account (arrows).

8.3 Formation Mechanisms

We have clearly found the overionized or recombining plasmas in SNRs but the formation mechanism is an open question. We here mention the evolution of the ionization degree in SNRs, and discuss the possible formation mechanisms of the anomalous plasma state.

Time Evolution of Ionization Degree in Normal SNRs

We first mention normal evolution of ionization degree in SNRs. Soon after the SN explosion, elements in the progenitor are heated and almost fully ionized due to a passage of the blast wave going through the progenitor. Expansion after the shock passage cools down the plasma. The density is high enough that highly ionized ions soon recombine with electrons. Assuming the typical density in this phase ($\sim 10^8$ cm^{-3}) and typical recombination coefficient ($\sim 10^{-12}$–10^{-11} cm^{3}s^{-1}), recombination timescale is estimated to be $\sim 10^3 - 10^4$ seconds. In this way, highly ionized ions recombine within one day.

After a few days of the SN explosion, the plasma is again heated by the radiative decay of ^{56}Ni which is synthesized in the explosion [14]. In this phase, the temperature of the center of the progenitor is $\sim$several $\times$ 10^4 K and atoms are in the several-ionized state. On the other hand, the temperature outside the photosphere is $\sim$several $\times$ 10^3 K, and atoms are in the first- or second-ionized state.

After $\sim$100 days, the whole SN region becomes optically thin. Almost all the ejecta atoms are in the first- or second-ionized state in this phase. This ionization state of the ejecta lasts until a reverse shock passes the plasma. As the ejecta expands, the reverse shock is formed by the interaction with the ambient matter and it propagates toward the ejecta core from the contact interface. Then, thermal energy is transferred from ions to electrons through Coulomb collisions in the post-shock region. Heated electrons gradually ionize atoms, as we mentioned in chapter 1. For a fiducial density (1 cm^{-3}) of SNR plasmas, electrons are heated up to $\sim$ keV in $\sim 10^2$ years (Masai 1994), while it takes $\sim 10^4$ years (or $nt \sim 10^{12}$ cm^{-3} s) for collisional ionization to reach its equilibrium state [15]. Therefore, X-ray bright young SNRs are thought to exhibit under-ionized ($kT_{\rm e} > kT_z$) or ionizing states.

[14] ^{56}Ni decays to ^{56}Co in $\sim$6 days (half life), and ^{56}Co to ^{56}Fe in $\sim$77 days (half life).

[15] Equipartition timescale is of the same order as ionization timescale.

Formation Processes of Recombining Plasma

As we see above, the overionized or recombining plasma state cannot be expected in the ordinary evolution of SNRs. Hence we need a particular process to explain the coexistence of the highly-ionized atoms and low-temperature electrons as below.

1. Increase the ionization degree of atoms.
2. Decrease the thermal energy of electrons.

1) One possible scenario to increase the ionization degree is photoionization. Since no strong radiation source is found near the observed RD SNRs, very recent photoionization is unlikely. Instead, strong photoionization at the moment of the SN explosion may be possible.

X-ray afterglow is an example, which occurs subsequently to a gamma-ray burst (GRB). It is known that some of GRBs are associated with the SN explosion (Type Ic) of massive ($\sim$40 $M_\odot$) stars, called hypernovae; examples are GRB980425, GRB030329, and GRB031203. Perna & Loeb (1998) suggest that the X-ray and UV components of the afterglow of GRB create an ionized bubble of radius $\sim$100 pc in the surroundings of the density of 1 cm^{-3}. It is possible that X-ray afterglow of these hypernovae irradiates and ionizes surrounding matter in the very initial phase of the SNR evolution.

Similar example is an X-ray flash, which is less energetic than a GRB. It emits mainly X-rays instead of gamma-rays. Some of X-ray flashes are thought to be associated with the SN explosion of $\sim$20 $M_\odot$ stars; an example is XRF060218.

Another example of photoionization is break-out X-rays from normal SNe. Colgate (1968) predicts a soft X-ray flash to occur when the shock wave breaks out of the progenitor. Soderberg et al. (2008) discovered the luminous X-ray outburst from SN 2008D, and interpret it as the shock break-out. Candidates to emit break-out X-rays are type Ib and Ic SNe [16].

These mechanisms would make atoms highly-ionized in the initial phase of the SNR evolution. If the highly-ionized atoms still survive, we observe the overionized or recombining plasmas. We discuss this scenario later from the view points of the timescale and metallicity.

[16] Type II SNe are expected to emit ultraviolet photons rather than X-rays because of large radii of their progenitors. Note that typical temperature (T) is expected to be $T \propto R^{-3/4}E^{1/4}$, where R is a radius of the progenitor and E is the explosion energy.

2) One mechanism to decrease the electron temperature is thermal conduction. This possibility is discussed by Kawasaki et al. (2002 Ph.D.thesis) for IC 443. They showed that IC 443 is composed of a central hot ($kT_e \sim 1.0$ keV) region and a surrounding cool ($kT_e \sim 0.2$ keV) shell, and interpreted that the hot interior have cooled via thermal conduction to the cool exterior. Under the several reasonable boundary conditions [17], they estimated the conduction timescale ($t_{\rm cond}$) in which the temperatures of the hot and cold plasma components to be comparable to each other. They approximately estimate the age of the plasma to be (0.3–1.0) $\times 10^4$ years, which is consistent with the SNR age ($\sim$4000 years : Troja et al. 2008). Hence they claim that the timescale of thermal conduction is shorter than that of recombination, and thus overionized plasma is formed in IC 443.

Based on our results, however, the conduction timescale is estimated to be

$$t_{\rm cond} \simeq 1.5 \times 10^4 \left(\frac{n_{\rm e}}{1.0 \ {\rm cm}^{-3}} \right) \left(\frac{kT_{\rm e}}{0.7 \ {\rm keV}} \right)^{-5/2} {\rm yr} \ , \tag{8.1}$$

following equation 5 of Kawasaki et al. (2002). Assuming both kT_z and $kT_{\rm e}$ are e-folding with their characteristic timescales [18], the age of the plasma ($t_{\rm age}$) is estimated from

$$\frac{kT_z}{kT_e} \sim \frac{\exp(-\frac{t_{\rm age}}{t_{\rm rec}})}{\exp(-\frac{t_{\rm age}}{t_{\rm cond}})} \simeq \frac{1.1 \ {\rm keV}}{0.7 \ {\rm keV}}. \tag{8.2}$$

Here, $t_{\rm rec}$ is the characteristic timescale to reach ionization equilibrium. In the case of S at a temperature around $\sim$1 keV, $t_{\rm rec} \sim 3 \times 10^4 (n/1 \ {\rm cm}^{-3})$ years (equation 3 of Kawasaki et al. 2002; Masai 1994). Then we obtain $t_{\rm age} \sim 1.4 \times 10^4$ years. Because it is far longer than the SNR age, this scenario cannot work on our new results. Thus, it is difficult to explain the overionized or recombining plasma with the thermal conduction process.

[17] They estimate the scale length of the temperature gradient is $\sim$(1–2)$\times 10^{19}$ cm, which corresponds to the distance between the hot-cool plasma boundary and the edge of the SNR.

[18] This is the same assumption with Kawasaki et al. (2002).

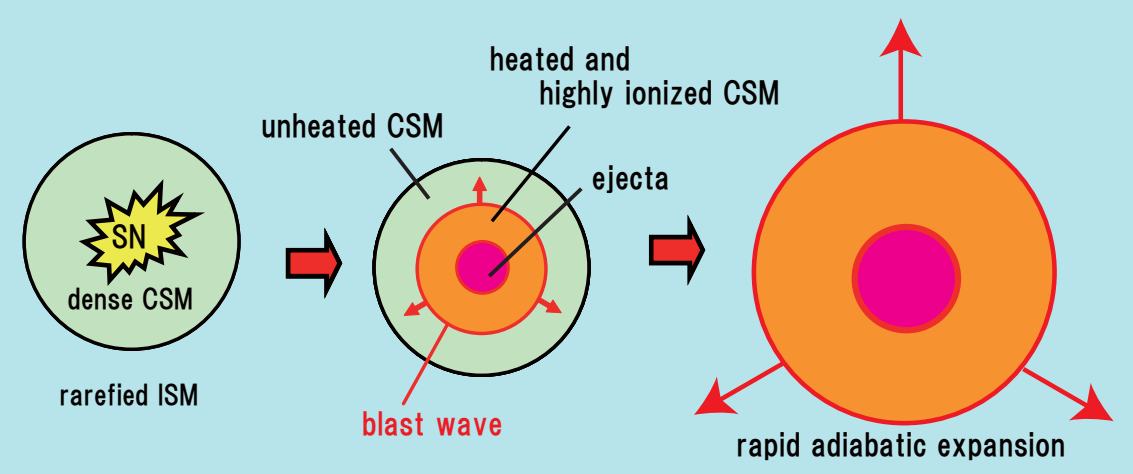

Fig. 8.8.—: Schematic illustration of the rarefaction scenario of Itoh & Masai (1989). When supernova explosion occurs in the dense circumstellar matter, the matter is heated and highly ionized by the blast wave. Subsequent rapid adiabatic expansion cools the shocked gas quickly.

1) & 2) The other possibility is the combination of 1) and 2). As a candidate of the formation mechanisms of recombining plasma, we may propose the rarefaction process which is discussed by Itoh & Masai (1989). Figure 8.8 shows a schematic illustration of this process. In this scenario, a SN[19] explodes in the dense circumstellar matter (CSM) which is formed by the progenitor's stellar wind in its supergiant phase. Because of the presence of CSM, the gas is shock-heated to high temperature and rapidly ionized in the early phase of the SNR evolution. Subsequent outbreak of the shock wave through the dense CSM into a low-density interstellar medium (ISM) caused drastic adiabatic expansion of the shocked gas. If the CSM is much denser than the ambient ISM, the timescale of adiabatic cooling is much shorter than that of recombination, and hence the remnant becomes overionized in this stage. The recombination process dominates radiation, and the X-ray spectrum is characterized by strong recombination lines and continua.

Itoh & Masai (1989) investigate the dynamical evolution and non-equilibrium X-ray emission of the SNR using a spherically-symmetric hydrodynamic code. The time evolution of physical quantities is shown in figure 8.9 with parameters taken in the calculations. In this example (density of the CSM is ~ 600 cm^{-3}), recombination timescale is $\sim 10^1$–10^2 years for typical recombination coefficients ($\sim 10^{-12}$–10^{-11} cm^{3}s^{-1}). Thus, the highly ionized state could remain for several decades until the blast wave breaks out of the dense CSM. We can see the X-ray luminosity and electron temperature decrease drastically by rarefaction due to rapid adiabatic expansion, as seen in figure 8.9. High Fe Kα center energy of W49B and IC 443 can be explained with this scenario. We also show the time evolution of the shocked-matter radial profile and X-ray spectrum in figure 8.10. We can see a strong RRC of Fe at 200 years after the explosion. Thus, rarefaction is a possible process to produce the recombining plasma.

In the following, we discuss the origin of the observed recombining plasma from the view points of timescale, metallicity, spatial distribution, and surrounding environment.

[19]Type II SNe are assumed, because their progenitors are expected to blow slow winds with high mass-loss rates in their red supergiant phase.

(a)

Model	M_{sn} ($M_\odot$)	E_{sn} (10^{51} erg)	r_c (pc)	r_{sn} (pc)	n	M_{cs} ($M_\odot$)	r_{cs} (pc)	N_0 (atoms cm^{-3})
E	10	2	0.0032	0.0065	6	1.5	0.3	0.16
F	10	2	0.0032	0.0065	6	0	-	0.16

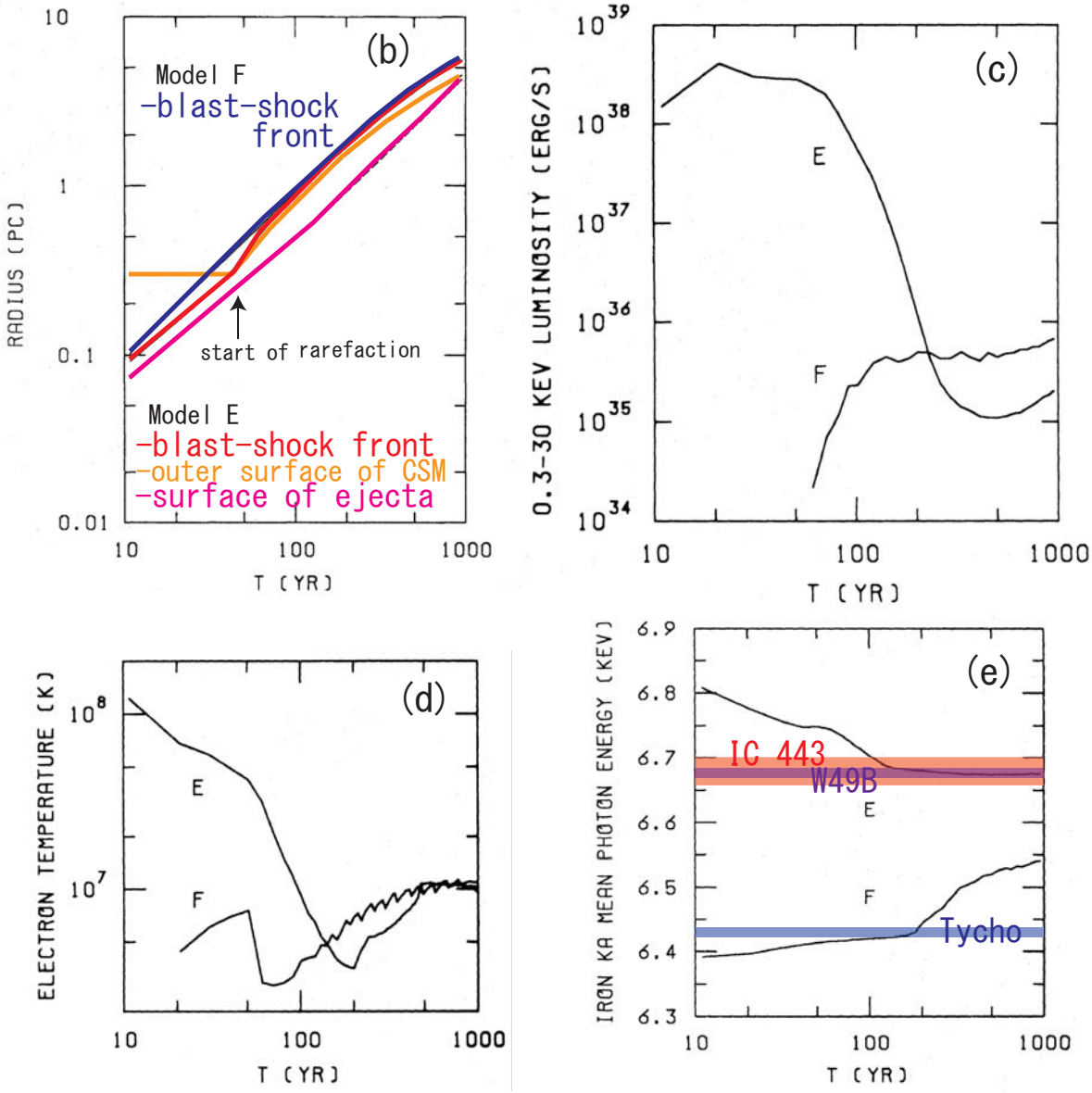

Fig. 8.9.—: Time evolution of physical quantities with (Model E) and without (Model F) CSM (Itoh & Masai 1989). (a) Model parameters. M_{sn}, E_{sn}, r_{sn}, M_{cs}, r_{cs}, and N_0 indicate the initial supernova ejecta mass, kinetic energy, ejecta radius, CSM mass, CSM radius, and ISM density. They assume the uniform ejecta density up to the core radius r_c, and the density $\propto r^{-n}$ at radius $r_c < r < r_{sn}$ with a constant n. (b) Time evolution of the radii, (c) X-ray luminosity, (d) electron temperatures, and (e) emissivity-weighted line energy of Fe Kα. We can see that the luminosity and electron temperature rapidly decrease by rarefaction (c and d). Wiggles of the curves in (d) are due to finite zoning of the remnant in the calculations, and are spurious. We show the observed line center energy in (e) for reference.

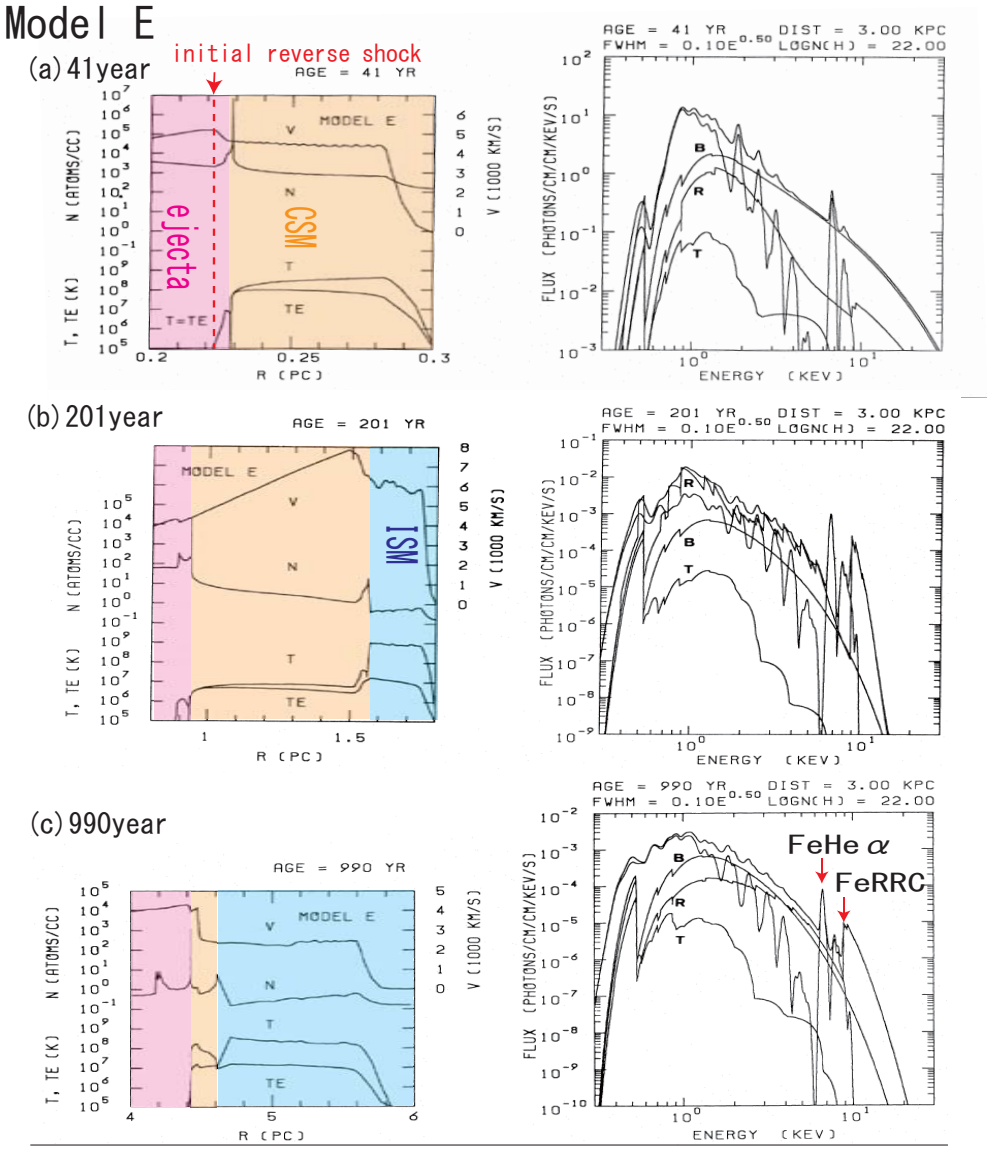

Fig. 8.10.—: Shocked-matter radial profiles (left) and spectra (right) at (a) 41 years, (b) 201 years, and (c) 990 years after the explosion (Itoh & Masai 1989), where v, N, T, and T_e are the velocity, density, electron-ion averaged temperature, and electron temperature, respectively. The spectra is shown for total emission, line emission, bremsstrahlung (B), recombination radiation (R), and two-photon emission (T). The total and line spectra are convolved with a Gaussian to a resolution of $0.1E^{0.5}$ keV (FWHM), where E is the photon energy in units of keV. The distance and the interstellar hydrogen column density to the SNR are taken to be 3 kpc and 10^{22} cm^{-2}, respectively. We can see strong RRC and cascade structures of Fe in the spectra of (b) and (c), which is similar to the Suzaku W49B spectrum.

Recombination Timescale

One question is that highly-ionized ions which were formed in the initial or early phase of the SNR evolution can survive until today or not. The lifetimes of the fully-stripped ions (τ) are roughly estimated from

$$\tau \simeq \frac{1}{\alpha n_{\rm e}}, \tag{8.3}$$

where α is the total K-shell recombination rate coefficient. We obtain $\simeq 4.8 \times 10^3 (n_{\rm e}/1.0\ {\rm cm}^{-3})^{-1}$ years for Si and $\simeq 3.4 \times 10^3 (n_{\rm e}/1.0\ {\rm cm}^{-3})^{-1}$ years for S, respectively. Note that these values are somewhat shorter than the actual timescale for the plasma to reach the CIE state. Nevertheless, the estimated lifetimes are comparable to the age of IC 443 ($\sim 3\times10^3$–4×10^3 years; Petre et al. 1998; Troja et al. 2008). The overionized plasma can, therefore, still survive at present. Thus, both photoionization and rarefaction are plausible processes to be responsible for the formation of the overionized plasma.

We also discuss the timescale for the other SNRs. The lifetimes of highly-ionized ions are $\simeq 3.5 \times 10^4 (n_{\rm e}/0.23\ {\rm cm}^{-3})^{-1}$ years for H-like Si, $\simeq 6.5 \times 10^4 (n_{\rm e}/0.23\ {\rm cm}^{-3})^{-1}$ years for H-like S, and $\simeq 5.3 \times 10^3 (n_{\rm e}/1.9\ {\rm cm}^{-3})^{-1}$ years for H-like Fe. Because no information of the age is available for W49B and G359.1-0.5, We cannot directly compare these lifetimes with the age of these SNRs. However, from the size and temperature, we can reasonably assume W49B and G359.1-0.5 are middle-aged SNRs ($\sim 10^3$–10^4 years). Thus the highly-ionized ions could survive until today.

Metallicity of the Recombining Plasma

The abundances of the RD SNRs are $\sim$3 solar for W49B (Fe & Ni), $\sim$2 solar for IC 443 (Si & S), and $<$10 solar for G359.1-0.5 (Si & S). All these are significantly higher than the solar values, implying at least part of the recombining plasma is the ejecta origin. We here discuss this point.

In the case of photoionization at the explosion, temporary strong X-rays (afterglow of the GRB, X-ray flash, or breat-out X-rays) irradiate and ionize the matter outside the progenitor; it is difficult to ionize the ejecta elements. Because typical abundance of the CSM is $\sim$1 solar, we can say it is unlikely to form a high metallicity recombining plasma by the photoionization process only.

On the other hand, it is possible to form overionized states of ejecta elements in the case of the rarefaction scenario. Collision between the ejecta and CSM produce a reverse shock in the initial phase of the SNR evolution (initial reverse shock in figure 8.10). This initial reverse shock heats the ejecta and then atoms are highly ionized. The subsequent blast wave break cools the shocked matter rapidly leaving the ionization state high. Thus, the recombining plasma of the ejecta elements could be formed.

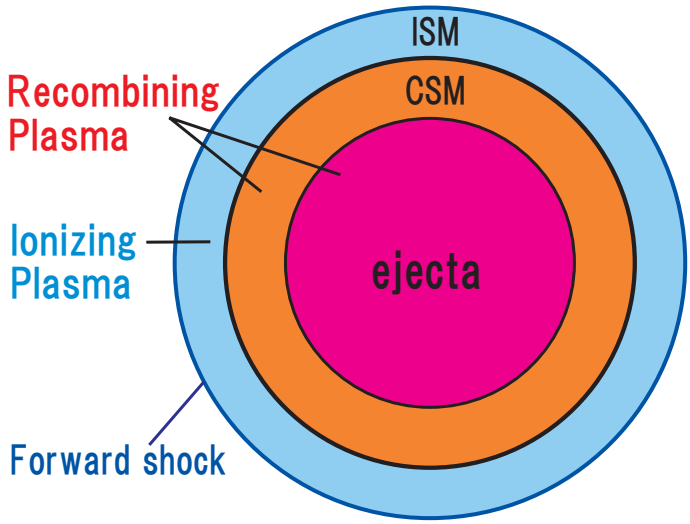

Fig. 8.11.—: Schematic view of the plasma state in the rarefaction model. In the early phase of the SNR evolution, shock-heated electrons ionize the ejecta and dense CSM and cools rapidly when the blast wave breaks out of the CSM into the low density ISM. If there is no anisotropy in the ejecta or the stellar wind (CSM), the strongly recombining plasma are expected to form in a ring shape of CSM and part of ejecta.

Spatial Distribution

In the photoionization scenario of GRB afterglow or X-ray flash, it is likely that the RD region is anisotropically formed, such as in a bipolar shape. W49B might be a possible candidate [20]. In the case of break-out X-rays, the overionized region is expected to be a spherically-symmetric shell, which is not the case for W49B.

In the rarefaction model, we can expect the plasma structure as figure 8.11. The strongly recombining plasma is produced mainly in the heated CSM, which was once highly-ionized in the early phase of the SNR evolution. The heated ejecta could be recombining as we mentioned in the discussion of the metallicity. In this scenario, the strongly recombining plasma would form in a spherically-symmetric shell or sphere shape.

Our results of IC 443 are consistent with the rarefaction scenario. As we see in figure 6.11, the strongly recombining plasma seems to form around the ejecta ring area which is revealed by XMM-Newton (figure 6.2). We nevertheless cannot strongly conclude that it is spherically-symmetric shell like, because current two fields of view of Suzaku XIS do not cover the whole reverse shock area. Thus, observations of the whole remnant are strongly required.

As we see in figure 5.12, the highly overionized region of W49B is not spherically-symmetric. Instead, it shows asymmetrical structure which extends east and west. The strongly recombining or highly overionized region is located in the west. It seems the rarefaction scenario cannot work for W49B. However, if we interpret the explosion had occurred asymmetrically to the west, the scenario is still plausible. This is probable because there is a dense molecular cloud at the east end of W49B (see figure 5.2).

[20]Note that the photoionization senario is unlikely in perspective of metallicity.

We expect that the highly overionized region corresponds to the steep gradient area in the electron temperature and X-ray intensity from the rarefaction model. This picture fairly well coincide with our results of W49B and IC 443 (see figure 6.10 and 5.11, for example).

Surrounding Environment

We propose that the most plausible scenario for the formation of the overionized plasma is the drastic cooling in the rarefaction process. In this case, some dense CSM should preexist around the supernova progenitor at the moment of explosion. Because such CSM can be formed by a stellar wind, the RD SNRs would originate from gravitationally collapsed supernovae [21] of massive stars [22]. In this case, there might be a connection between RD SNRs and star-forming regions or molecular clouds. We discuss this point.

IC 443 is located near the Gem OB1 association, which is one of the most massive molecular cloud complexes in the Galaxy. Also, the progenitor of IC 443 is suggested to be a massive star with strong stellar wind activity (Braun & Strom 1986; Meaburn et al. 1990). These facts strongly support the existence of the dense CSM around IC 443 at the time of its explosion.

It is likely that W49B is located near the star forming region, W49A. The composite image (figure 5.2) is suggestive of bipolar structures surrounding massive stars. We can see the molecular cloud in the east side of the remnant (figure 5.2). Thus, it is natural that we consider W49B as a remnant of gravitationally collapsed massive star.

G359.1-0.5 is surrounded by a molecular cloud (Uchida, Morris, and Yusef-Zadeh 1992). Because it is located in the Galactic center region, there are many massive star-forming regions. Accordingly, the progenitor of G359.1-0.5 was possibly a massive star.

[21] Especially Type II SNe (the core collapse of red supergiants) because progenitors of Type II SNe blow slow stellar winds with high mass-loss rates.

[22] Note that this picture is also supported by the estimated mass of the RD SNRs (table 8.4).

8.4 Future Works

Research for Other RD SNRs and RD Regions

We have discovered the RD SNRs, but the sample is still limited to three cases. In order to investigate their characteristics and origin, we should further explore other SNRs with high statics. The RD SNRs might have center-filled morphology in X-rays, exhibit strong Lyα lines in their spectra, and associate with star-forming regions or dense molecular clouds. With these criteria, the candidates would be W44, W28, 3C391, and 3C397. Another key to verify the formation mechanisms is the spatial distribution of the RRC. Thus, the observation of the whole IC 443 region is strongly required.

High resolution X-ray spectroscopy

Although we firmly detected the recombination continuum and lines, we cannot separately detected the fine structures with the energy resolution of the X-ray CCD. For example, we cannot clearly derive the recombination continua and lines. We also cannot distinguish the resonance, inter-combination, and forbidden lines.

X-ray micro-calorimeter on board Astro-H, which is the next Japanese X-ray satellite expected to be launched in 2014, has a very high energy resolution of 7 eV between 0.3–12 keV. If we use this device, we could completely divide the continuum and line emissions (figure 8.12). We, furthermore, could separately detect the emission lines of resonance, inter-combination, and forbidden. As we mention in chapter 4, the line intensity ratio between the resonance and forbidden is different among the collisional-dominant and recombination-dominant cases. Thus, X-ray micro-calorimeter would reveal a new aspect for the study of the recombination-dominant plasma.

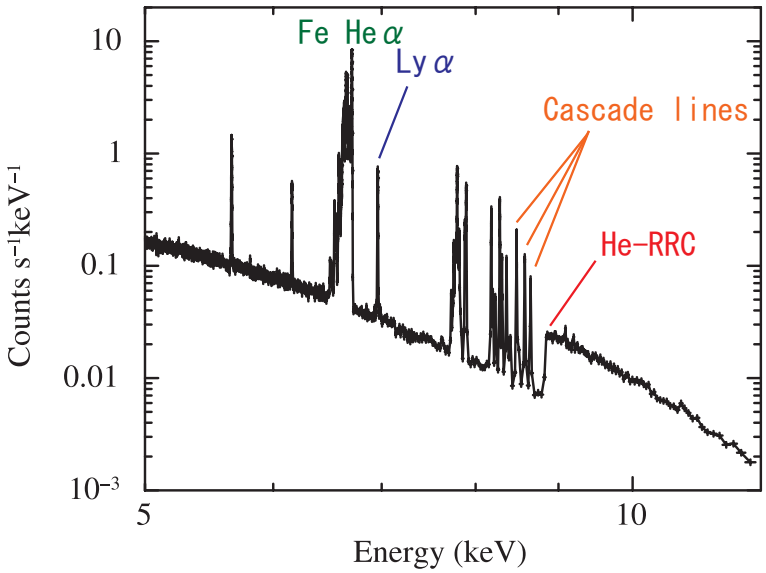

Fig. 8.12.—: Simulated Astro-H micro-calorimeter spectrum of W49B in the 5–12 keV band.

Chapter 9

Conclusion

We have performed a recombination X-ray study from three SNRs (W49B, IC 443, and G359.1-0.5) utilizing the good energy resolution and high sensitivity of Suzaku. The important results are summarized as follows:

1. Strong radiative recombination continua are firmly detected for the first time in supernova remnants. The detected continuum structures originate from highly-ionized iron atoms for W49B, wheras silicon and sulfur atoms for IC 443 and G359.1-0.5. Recombination lines of iron due to the cascade decays of electrons are also detected from W49B for the first time.

2. For all these remnants, electron temperatures independently determined from the bremsstrahlung and recombination continuum shapes are consistent with each other for all these SNRs. Volume emission measures for both components are the same order. Hence, all the X-ray spectra of the observed SNRs can be explained by a single recombining plasma component in the highly overionized state.

3. Spectra of these recombination-dominant SNRs all exhibit the strong recombination continuum structures, strong H-like Kα line intensity, and high center energies for He-like Kα lines. All these SNRs have awkward and center-filled morphology in X-ray.

4. Spatial distribution of W49B and IC 443 both indicates significant anisotropy of the recombination-dominant plasma. The region with strong recombination features corresponds to a high gradient area of electron temperature and surface brightness. Combined with the spatial distribution, timescales of highly-ionized atoms, metallicity of recombining plasma, and surrounding environment of the remnants, the plausible candidate for strongly recombining plasma of a supernova explosion in a dense circumstellar matter is proposed.

Appendix A

Suzaku Observation of Tycho

Tycho was observed twice [1] with Suzaku in the large proposal project. Because the pointing positions are almost the same, we merged these two data sets. The observation log is given in table A.1. We used the Lockman Hole observation [2] as background data. Three of the XISs (two for FIs and one for a BI) were operated in the normal full-frame clocking mode with a SCI technique during all the observations. Data were cleaned using processing version 2.2.11.24. We used HEASOFT version 6.5.1 for data reduction and XSPEC version 11.3.2 for spectral analysis. After screening with the standard criteria, the net integration time is ∼400 ks for the source region and ∼70 ks for the background region.

Figure A.1a shows the XIS image of Tycho in the 0.5–7 keV band. We extract the source spectrum from the circular region with a radius of 4 arcmin. Background spectrum was also extracted from the Lockman Hole data with the same region in the detector coordinates. The source spectrum is made by subtracting the background spectrum. In figure A.1b, we show the XIS 0 spectra. We can see several prominent lines of K-shell emission from Ne, Mg, Si, S, Ar, Ca, and Fe. The spectra of the two FI sensors are merged to improve the statistics. During the fitting, we fix the interstellar extinction on Tycho to a hydrogen column density of 7×10^{21} cm^{-2} with the solar elemental abundances, following Cassam-Chenai et al. (2007).

[1] Suzaku also observed Tycho in June 2006 for 50 ksec. This is the data taken without SCI, and the energy gain and response are significantly different from those of the SCI data. We therefore use only the SCI data.

[2] This is the field with no bright X-ray sources.

Table A.1—: Observation log of Tycho and Lockman Hole.

Target	Start Date	Obs.ID	R. A.	Dec.	Exposure
			(J2000.0)		(ks)
Tycho *	2008-08-04	503085010	$00^h25^m20^s$	$64°08'18''$	313
Tycho *	2008-08-11	503085020	$00^h25^m20^s$	$64°08'18''$	103
Lockman Hole**	2008-05-18	103009010	$10^h51^m45^s$	$57°16'00''$	73

*Used as source data. **Used as background data.

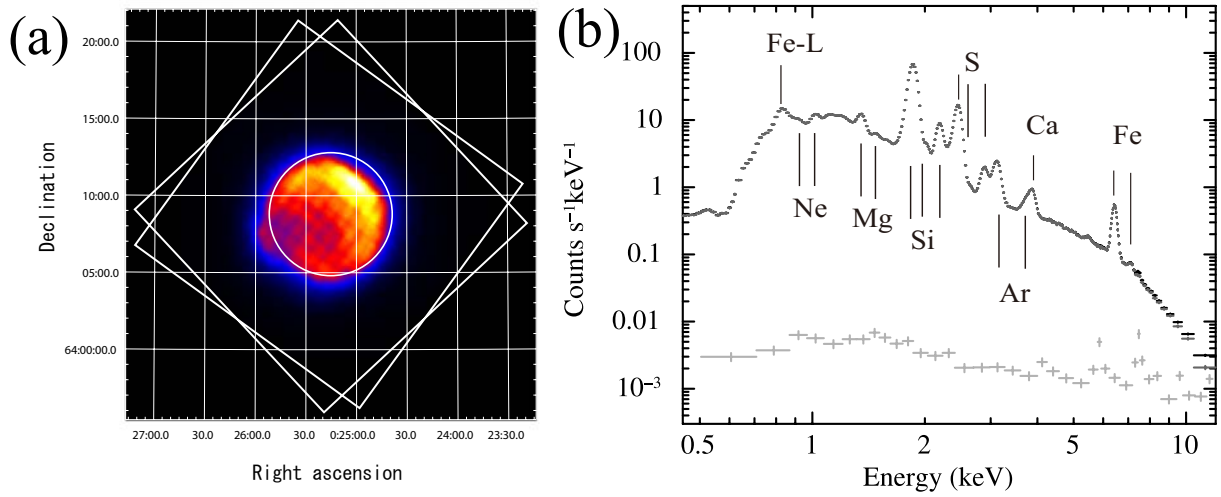

Fig. A.1.—: (left) Suzaku XIS image in the 0.7–5.0 keV band of Tycho shown on a linear intensity scale. Data from the three active XISs are combined. The white circle indicates the source region. The white squares are XIS field of views for two observations. (right) XIS 0 spectrum extracted from a white circle in the left figure. The energies of the prominent emission lines from specific elements are labeled. We show the raw source spectrum in black, background spectrum in light gray, and background-subtracted source spectrum in dark gray. Note that the background contribution is negligible.

Appendix B

Abbreviation

- APEC: Astrophysical Plasma Emission Code
  (thin thermal plasma code in the ionization equilibrium state)
- CCD: Charge Coupled Device
- CFCI: Checker-flag Charge Injection
  (one of the charge injection techniques of the Suzaku XIS)
- CIE: Collisional Ionization Equilibrium
- CSM: Circumstellar Matter
- CTI: Charge Transfer Inefficiency
- CXB: Cosmic X-ray Background
- dof: Degree of Freedom
- EOB: Extendable Optical Bench (equipped on Suzaku)
- FOV: Field of View
- FWHM: Full Width at Half Maximum
- He-RRC: Radiative Recombination Continuum accompanied by electron recombination with H-like ions into the ground state of He-like ions
- Heα: He-like Kα
  (In the same way, Heβ and Heγ mean He-like Kβ and He-like Kγ, respectively.)
- H-RRC: Radiative Recombination Continuum accompanied by electron recombination with fully-ionized ions into the ground state of H-like ions
- HXD: Hard X-ray Detector (onboard the Suzaku satellite)
- ID: Ionization-dominant
- ISM: Interstellar Matter

- Lyα: H-like Kα
  (In the same way, Lyβ and Lyγ mean H-like Kβ and H-like Kγ, respectively.)
- NXB: Non X-ray Background
- RD: Recombination-dominant
- RRC: Radiative Recombination Continuum
- SCI: Spaced-row Charge Injection
  (one of the charge injection techniques of the Suzaku XIS)
- SN: Supernova
- SNR: Supernova Remnant
- XIS: X-ray Imaging Spectrometer (onboard the Suzaku satellite)
- XRT: X-ray Telescope (onboard the Suzaku satellite)

References

Acciari, V. A., et al. 2009, ApJ, 700, 1034

Aharonian, F., et al. 2006, Physical Review Letters, 97, 221102

Albert, J., et al. 2007, ApJ, 664, L87

Anders, E., & Grevesse, N. 1989, Geochim. Cosmochim. Acta, 53, 197

Badnell, N. R. 2006, ApJS, 167, 334

Bamba, A., et al. 2009, ApJ, 691, 1854

Bamba, A., Yokogawa, J., Sakano, M., & Koyama, K. 2000, PASJ, 52, 259

Bautz, M. W., et al. 2004, Proc. SPIE, 5501, 111

Bocchino, F., & Bykov, A. M. 2003, A&A, 400, 203

Braun, R., & Strom, R. G. 1986, A&A, 164, 193

Brogan, C. L., & Troland, T. H. 2001, ApJ, 550, 799

Cassam-Chenaï, G., Hughes, J. P., Ballet, J., & Decourchelle, A. 2007, ApJ, 665, 315

Chevalier, R. A. 1974, ApJ, 188, 501

Cioffi, D. F., McKee, C. F., & Bertschinger, E. 1988, ApJ, 334, 252

Claussen, M. J., Frail, D. A., Goss, W. M., & Gaume, R. A. 1997, ApJ, 489, 143

Colgate, S. A. 1968, Canadian J. Phys., 46, 476.

Cornett, R. H., Chin, G., & Knapp, G. R. 1977, A&A, 54, 889

Cox, D. P., et al. 1999, ApJ, 524, 179

Denoyer, L. K. 1978, MNRAS, 183, 187

Dickel, J. R., Williamson, C. E., Mufson, S. L., & Wood, C. A. 1989, AJ, 98, 1363

Downes, D., Goss, W. M., Schwarz, U. J., & Wouterloot, J. G. A. 1979, A&AS, 35, 1

Duin, R. M., & van der Laan, H. 1975, A&A, 40, 111

Esposito, J. A., Hunter, S. D., Kanbach, G., & Sreekumar, P. 1996, ApJ, 461, 820

Furuzawa, A., et al. 2009, ApJ, 693, L61

Gaensler, B. M., et al. 2006, ApJ, 648, 1037

Giovanelli, R., & Haynes, M. P. 1979, ApJ, 230, 404

Gray, A. D. 1994, MNRAS, 270, 835

Green D. A. 2009, `http://www.mrao.cam.ac.uk/surveys/snrs/`

Gwinn, C. R., Moran, J. M., & Reid, M. J. 1992, ApJ, 393, 149

Hewitt, J. W., Yusef-Zadeh, F., Wardle, M., Roberts, D. A., & Kassim, N. E. 2006, ApJ, 652, 1288

Hewitt, J. W., Yusef-Zadeh, F., & Wardle, M. 2009, ApJ, 706, L270

Hwang, U., Petre, R., & Hughes, J. P. 2000, ApJ, 532, 970

Ishisaki, Y., et al. 2007, PASJ, 59, 113

Itoh, H., & Masai, K. 1989, MNRAS, 236, 885

Iwamoto, K., et al. 1999, ApJS, 125, 439

Kawasaki, M. Ph.D. thesis; The University of Tokyo

Kawasaki, M. T., Ozaki, M., Nagase, F., Masai, K., Ishida, M., & Petre, R. 2002, ApJ, 572, 897

Kawasaki, M., Ozaki, M., Nagase, F., Inoue, H., & Petre, R. 2005, ApJ, 631, 935

Keohane, J. W., Reach, W. T., Rho, J., & Jarrett, T. H. 2007, ApJ, 654, 938

Kelley, R. L., et al. 2007, PASJ, 59, 77

Kokubun, M., et al. 2007, PASJ, 59, 53

Koyama, K., et al. 2007a, PASJ, 59, 23

Koyama, K., et al. 2007b, PASJ, 59, 245

Krause, O., Tanaka, M., Usuda, T., Hattori, T., Goto, M., Birkmann, S.,& Nomoto, K. 2008, Nature, 456, 617

Kushino, A., et al. 2002, PASJ, 54, 327

LaMarr, B., et al. 2004, Proc. SPIE, 5501, 385

Leahy, D. A. 2004, AJ, 128, 1478

Masai, K. 1994, ApJ, 437, 770

Masai, K., Dogiel, V. A., Inoue, H., Schönfelder, V., & Strong, A. W. 2002, ApJ, 581, 1071

Matsumoto, H., et al. 2006, Proc. SPIE, 6266

Mazzotta, P., Mazzitelli, G., Colafrancesco, S., & Vittorio, N. 1998, A&AS, 133, 403

Meaburn, J., Whitehead, M. J., Raymond, J. C., Clayton, C. A., & Marston, A. P. 1990, A&A, 227, 191

Mewe, R., Gronenschild, E. H. B. M., & van den Oord, G. H. J. 1985, A&AS, 62, 197

Miceli, M., Decourchelle, A., Ballet, J., Bocchino, F., Hughes, J. P., Hwang, U., & Petre, R. 2006, A&A, 453, 567

Mitsuda, K., et al. 2007, PASJ, 59, 1

Moffett, D. A., & Reynolds, S. P. 1994, ApJ, 437, 705

Nakajima, H., et al. 2008, PASJ, 60 , 1

Nakayama, M., & Masai, K. 2001, ApJ, 375, 328

Nomoto, K., Thielemann, F.-K., & Yokoi, K. 1984, ApJ, 286, 644

Olbert, C. M., Clearfield, C. R., Williams, N. E., Keohane, J. W., & Frail, D. A. 2001, ApJ, 554, L205

Ozawa, M., et al. 2008, Proc. SPIE, 7011,

Ozawa, M., Koyama, K., Yamaguchi, H., Masai, K., & Tamagawa, T. 2009a, ApJ, 706, L71

Ozawa, M., et al. 2009b, PASJ, 61, 1

Perna, R., & Loeb, A. 1998, ApJ, 503, L135

Petre, R., Szymkowiak, A. E., Seward, F. D., & Willingale, R. 1988, ApJ, 335, 215

Porquet, D., Mewe, R., Dubau, J., Raassen, A. J. J., & Kaastra, J. S. 2001, A&A, 376, 1113

Prigozhin, G. Y., et al. 2004, Proc. SPIE, 5501, 357

Prigozhin, G. Y., et al. 2008, IEEE Trans. Elec. Device., 55 , 2111

Pye, J. P., Becker, R. H., Seward, F. D., & Thomas, N. 1984, MNRAS, 207, 649

Radhakrishnan, V., Goss, W. M., Murray, J. D., & Brooks, J. W. 1972, ApJS, 24, 49

Rasmussen, A. P., Behar, E., Kahn, S. M., den Herder, J. W., & van der Heyden, K. 2001, A&A, 365, L231

Rho, J., & Petre, R. 1998, ApJ, 503, L167

Rho, J., Jarrett, T. H., Cutri, R. M., & Reach, W. T. 2001, ApJ, 547, 885

Ruiz-Lapuente, P. 2004, ApJ, 612, 357

Sedov, L. I. 1959, Similarity and Dimensional Methods in Mechanics, New York: Academic Press, 1959

Serlemitsos, P. J., et al. 2007, PASJ, 59, 9

Shelton, R. L. 1999a, ApJ, 521, 217

Shelton, R. L., Cox, D. P., Maciejewski, W., Smith, R. K., Plewa, T., Pawl, A., & Różyczka, M. 1999b, ApJ, 524, 192

Soderberg, A. M., et al. 2008, Nature, 453, 469

Smith, R. K., Brickhouse, N. S., Liedahl, D. A., & Raymond, J. C. 2001, ApJ, 556, L91

Takahashi, T., et al. 2007, PASJ, 59, 35

Tamagawa, T., et al. 2009, PASJ, 61, 167

Tavani, M., et al. 2010, ApJ, 710, L151

Tawa, N., et al. 2008, PASJ, 60, 11

Thielemann, F.-K., Nomoto, K., & Hashimoto, M.-A. 1996, ApJ, 460, 408

Troja, E., Bocchino, F., & Reale, F. 2006, ApJ, 649, 258

Troja, E., Bocchino, F., Miceli, M., & Reale, F. 2008, A&A, 485, 777

Truelove, J. K., & McKee, C. F. 1999, ApJS, 120, 299

Tsunemi, H., Yamashita, K., Masai, K., Hayakawa, S., & Koyama, K. 1986, ApJ, 306, 248

Tucker, W. H., & Gould, R. J. 1966, ApJ, 144, 244

Uchida, K., Morris, M., & Yusef-Zadeh, F. 1992, AJ, 104, 1533

Uchiyama, H., et al. 2009, PASJ, 61, 9

Wargelin, B. J., Beiersdorfer, P., Neill, P. A., Olson, R. E., & Scofield, J. H. 2005, ApJ, 634, 687

Warren, J. S., et al. 2005, ApJ, 634, 376

Welsh, B. Y., & Sallmen, S. 2003, A&A, 408, 545

Yamaguchi, H., Ozawa, M., Koyama, K., Masai, K., Hiraga, J. S., Ozaki, M., Yonetoku, D. 2009, ApJ, 705, 6

Yang, X. J., Tsunemi, H., Lu, F. J., & Chen, L. 2009, ApJ, 692, 894

Yang, X. J., Tsunemi, H., Lu, F. J., & Chen, L. 2009, ApJ, 692, 894

Yusef-Zadeh, F., et al. 1996, The Galactic Center, 102, 151

Yusef-Zadeh, F., Wardle, M., Rho, J., & Sakano, M. 2003, ApJ, 585, 319

Acknowledgments

Without the support from my powerful collaborators, this thesis could not have been completed. My deepest appreciation goes to Katsuji Koyama who has been patiently encouraging me throughout my graduate course. I have learned a lot from him, not only the basis of X-ray astronomy, but also prospective attitude for the research and science. I express my gratitude to Hiroya Yamaguchi in RIKEN for his very helpful support. I thank the "encouraging person" Kuniaki Masai for giving me important suggestion and willingly offering me a lot of plasma radiation codes. His prompt response always surprised me.

My gratitude is for Masaomi Tanaka in University of Tokyo and Nozomu Tominaga in Kohnan University. I have learned a lot on supernovae and nucleosynthesis from them. Referring to the W49B proposal, I thank Toru Tamagawa. His easygoing attitude and nice smile helped me a lot. As for the calibration work of the Suzaku XIS, I was deeply helped by Hiroshi Nakajima, Hironori Matsumoto, Hideki Uchiyama, and Katsuji Koyoma. I thank the contribution of all the XIS team members.

I would like to thank all the members in the Cosmic-ray laboratory group in Kyoto University. I am grateful to Takeshi Go Tsuru and Hironori Matsumoto whose meticulous comments were of enormous help. I am grateful to Hideki Uchiyama for so much kindness, Makoto Sawada and Shinya Nakashima for checking the thesis and providing the figure, and Takao Ohnishi for helping with G359.1-0.5.

Finally, I express supreme thanks to all of my friends and family. I especially thank Sou Matsuura, Satoshi Okuzumi and Keisuke Onuma. It was my blissful moment to discuss the physics, science, and views of life. I was very shocked by Teruaki Enoto, Yudai Suwa, Masaomi Tanaka, Hajime Takami, and Shunsaku Horiuchi. It was very inspiring and interesting moment to talk to them. It was a great honor to be a member of "Four Devas" with Asami Hayato, Ryoko Nakamura, and Kaori Onda. I wish to express my sincere gratitude to my family, mother, father, grandmother, and sister, for their continuous and generous help.

I acknowledge financial support from the Japan Society for the Promotion of Science. This work is supported by the Grant-in-Aid for the Global COE Program "The Next Generation of Physics, Spun from Universality and Emergence", Challenging Exploratory Research, from the Ministry of Education, Culture, Sports, Science and Technology (MEXT) of Japan.